MnO₂-based nanostructures for high-performance supercapacitors

Ming Huang[a], Fei Li[a], Fan Dong[b], Yu Xin Zhang[a,c,*], Li Li Zhang[d,*]

[a] College of Materials Science and Engineering, Chongqing University, Chongqing 400044, P.R. China

[b] Chongqing Key Laboratory of Catalysis and Functional Organic Molecules, College of Environmental and Biological Engineering, Chongqing Technology and Business University, Chongqing 400067, P. R. China

[c] National Key Laboratory of Fundamental Science of Micro/Nano-Devices and System Technology, Chongqing University, Chongqing 400044, P.R. China

[d] Institute of Chemical and Engineering Sciences, A*STAR, 1 Pesek Road, Jurong Island, 627833, Singapore

[*]E-mail: zhangyuxin@cqu.edu.cn; zhang_lili@ices.a-star.edu.sg

Abstract

MnO₂-based materials have been intensively investigated for pseudocapacitors due to their high theoretical specific capacitance, good chemical and thermal stability, natural abundance, environmental benignity and low cost. In this review, several main factors that affect the electrochemical properties of MnO₂-based electrodes are presented. Various strategic design and synthesis of MnO₂-based electrode materials for enhanced electrochemical performance are highlighted and summarized. Finally, the challenges and future directions toward the development of MnO₂-based nanostructured electrode materials for high performance supercapacitors (SCs) are discussed.

1. Introduction

The rapid growth of population and global economy has significantly increased the demand for energy consumption. Due to the concern for the sever environmental impact by the fossil fuel and the increasing demand in grid energy storage and consumer electronics, efficient energy storage systems are highly desired.[1-6] Electrochemical energy storage (EES) devices are particularly useful for portable electronic devices and hybrid electric vehicles.[7-9] Among various emerging EES technologies, supercapacitors (SCs), also known as electrochemical capacitors (ECs), have attracted tremendous attention because of their high power density (>10 kW kg⁻¹),

high rate capability, long cycling life (> 100000 cycles) and safe operation.[10-12] A Ragone plot (Fig. 1) illustrates the power density and energy density of various EES systems,[1] in which SCs occupy the important position since it bridges the power-energy gap between traditional capacitors and batteries/fuel cells. With a combination of high power density and relatively high energy density, SCs have been widely used in a variety of applications ranging from portable consumer electronics, memory back-up system, automotives, to industrial power and energy management, and many more.[13-15]

Based on the energy storage mechanism, SCs can be classified into two categories, namely, electric double-layer capacitors (EDLCs) and pseudocapacitors.[16, 17] In EDLCs, the capacitance comes from the adsorption of both anions and cations at the electrode/electrolyte interface (Fig. 2a),[18] thus it is strongly dependent on the surface area of the electrode materials that is accessible to the electrolyte ions. During the charging process, the electrons move from the negative electrode to the positive electrode through the external loop, with anions moving to the positive electrodes, while the cations move towards the negative electrode. The moving direction of the electrons and ions would be reversed in the discharging process.[12, 19] Typical electrode materials for EDLCs are porous carbons, such as activated carbon,[20-25] xerogels,[26-31] carbon nanotubes (CNTs),[32-36] carbon nanofibers (CNFs),[37-41] mesoporous carbon,[42-46] graphene,[47-50] and carbide-derived carbons.[51-56] Previous research has shown several important factors affecting the performance of carbon-based electrodes: the specific surface area, electrical conductivity, pore size and distribution. In most cases, porous carbon materials exhibit high specific surface area and good conductivity. However, the low energy density, especially the low volumetric energy density of carbon-based materials is yet to be improved. In contrast to EDLCs, pseudocapacitors store energy through a Faradic process that involves fast and reversible redox reactions occurring at or near the electrode surface.[57] As shown in Fig. 2b, when a potential is applied, the electrode materials undergo reversible redox reactions, generating charges and resulting in Faradic current passing through the supercapacitor cells.[18] Since the capacitance depends on the Faradic charges generated at or near the electrode surface, it is extremely important to use pseudo-capacitive materials with high charge generation and storage ability in short period of time. The most widely explored pseudo-capacitive electrode materials include conducting polymers (polyaniline,

polypyrrole, and polythiophene)[58-64] and transition metal oxides or hydroxides (RuO_2, MnO_2,

Co_3O_4, NiO, CuO, Fe_2O_3, $Ni(OH)_2$, and $Co(OH)_2$)[65-72]. Compared with EDLCs, pseudocapacitors

can achieve much higher energy densities as they can provide a variety of oxidation states for

efficient redox charge transfer which could satisfy the needs of high-energy SCs. The challenges

associated with pseudocapacitors are rate capability and cycling stability.

Among electrode materials for pseudocapacitors, MnO_2 has been extensively investigated due

to its low cost, natural abundance, large theoretical capacity (~1370 F g^{-1}), and low toxicity.[73-79] In

1999, Lee and Goodenough first used the amorphous $MnO_2 \cdot nH_2O$ in a mild KCl aqueous

electrolyte as s possible electrode for supercapacitor, and a specific capacitance about 200 F g^{-1}

was obtained.[80] In order to increase the specific capacitance of MnO_2-based electrodes, synthesis

of nanostructured MnO_2-based electrodes with novel morphologies, hierarchical porous structures,

large pore volume and high specific surface area has been explored by various methods. Until now,

manganese oxides with various structures and morphologies such as nanosheets,[81] nanospheres,[82]

nanoflowers,[83] nanowires/nanorods,[84, 85] thin films,[86] and nanotubes[87] have been fabricated and

their electrochemical properties have been investigated. The studies have indicated that

MnO_2-based nanomaterials with controllable particle size, morphology, crystallinity, high specific

surface area and good electrical conductivity are critical for improving capacitance, rate capability

and cycling stability. Another effective approach to improve the performance of MnO_2-based

electrodes is the design of MnO_2-based composites by using highly conductive materials such as

porous metal substrates,[88] conducting polymers,[89, 90] carbon nanotubes/nanofibers/spheres,[91-93] and

graphene[94] as scaffolds. Very recently, an emerging attractive strategy is the synthesis of

multi-component MnO_2-based mixed oxides with a smart design to improve the performance

based on the synergistic effects from their individual constituents.

In this review, we first discuss several important factors affecting the electrochemical

properties of MnO_2-based materials. Then various fabrication strategies to make advanced

MnO_2-based nanostructures and MnO_2-based composite electrodes are summarized. Finally, the

challenges and the promising future of the MnO_2-based electrodes for SCs are presented.

2.   Factors affecting the pseudocapacitance of MnO_2-based materials

The charge that MnO_2-based pseudocapacitor electrode stores arises from the III/IV oxidation state change at or near the surface of MnO_2 nanostructures and the charge storage mechanism can be described by Equation (1):

$$MnO_2 + C^+ + e^- \leftrightarrow MnOOC \tag{1}$$

where C represents electrolyte cations such as H^+, K^+, Na^+ and Li^+.[95, 96] For the surface charge storage, Faradic reaction is achieved by adsorption/desorption of electrolyte cations and protons on the surface of MnO_2.[95, 97] The bulk pseudo-capacitive reaction relies on the intercalation/deintercalation of protons and cations into the bulk of the MnO_2.[98, 99] However, due to the poor electric conductivity and slow proton and cation diffusivity of the solid MnO_2 phase, the bulk pseudo-capacitive reaction is limited to a thin subsurface layer of MnO_2, for instance, *ca*. 420 nm in thickness according to Bélanger's study.[95] The electrochemical property of MnO_2-based electrodes is influenced by the crystallinity, crystal structure, morphology, conductivity, mass loading of active material, and electrolyte used for the electrode.

2.1 Crystallinity

The pioneering work on the capacitive behavior of MnO_2 are focused on amorphous MnO_2 and nanocrystalline compounds for the application in electrochemical capacitors, with the belief that a porous morphology can enhance the ion accessibility and cation diffusion.[100, 101] Xue et al.[102] adopted a direct precipitation approach to get the polymorphs of α-, δ-, γ- and β-MnO_2 by a simple redox reaction between $NaNO_2$ and $KMnO_4$. It was found that the capacitance performances of any particular MnO_2 phase decrease with increasing crystalline nature, and the poorly crystallized α-MnO_2 demonstrated the highest specific capacitance (200 F g^{-1} at a current density of 1 A g^{-1}). Nevertheless, the poorly crystallized MnO_2 contains intergrowth of different tunnel structures, leading to more difficult cation diffusion and resulting in higher resistance.[103] The capacitance of the amorphous MnO_2 is due to faradaic processes localized at the surface and subsurface regions of the electrode. The maximum capacitance of MnO_2 is limited by the upper limit of BET surface area it can achieve, further increasing the surface area does not provide additional capacitance.[99]

Many attempts have been made to explore the crystallized MnO_2 materials since the

capacitance of the crystallized materials is clearly dependent upon the crystalline structure, especially with the size of the tunnels able to provide limited cations intercalation.[103] Brousse and coworkers have synthesized different MnO_2 polymorphs with the aim of investigating the crystallinity/electrochemical properties relationship by evaluating the capacitance of these materials.[103] Since capacitance comes mainly from the intercalation/deintercalation of protons or cations in MnO_2, only some crystallographic structures, which possess sufficient gaps to accommodate these ions, are expected to be useful for further improving the capacitance. Also, a recent work reported the electrochemical properties of Nb_2O_5 and established that crystalline phases of the material underwent fast faradaic reactions that led to higher specific capacitance than that of the amorphous phase, suggesting that the Faradaic reactions which led to additional capacitive energy storage were associated with ion insertion along preferred crystallographic pathways.[104] Ran et al.[105] reported a facile and cost-effective strategy for the synthesis of a novel bird nest-like nanostructured MnO_2 material. The obtained nano-MnO_2 possesses a well designed loosely-assembled hierarchical nanoarchitecture with an appropriate crystallinity which gives rise to excellent performances as an electrode material for supercapacitors. A maximum specific capacitance of 917 F g^{-1} has been obtained at a current density of 5 mA cm^{-2}. Based on the above analysis, it is a great challenge and also of great significance to prepare novel MnO_2 nanostructures with high specific surface area and good crystallinity.

2.2 Crystal structure

Manganese oxide has several crystalline structures, including α-, β-, γ-, δ-, and λ-MnO_2, the different structures can be described by the size of their tunnel determined by the number of octahedra subunits (n × m), as depicted in Fig. 3.[106] α-MnO_2 consists of double chains of edge-sharing MnO_6 octahedra, which are linked at corners to form 1D (2 × 2) and (1×1) tunnels in the tetragonal unit cell. The size of the (2 × 2) tunnel is ~4.6 Å, which is large tunnel for insertion/extraction of alkali cations.[107] β-MnO_2 is composed of single strands of edge-sharing MnO_6 octahedra to form a 1D (1 × 1) tunnel. Because of the narrow (1 × 1) tunnel of size (~1.89 Å), β-MnO_2 cannot accommodate cations.[108] The structure of γ-MnO_2 is random intergrowth of ramsdellite (1 × 2) and pyrolusite (1 × 1) domains.[109] δ-MnO_2 is a 2D layered structure with an

interlayer separation of ~7 Å.[110] It has a significant amount of water and stabilizing cations such as Na$^+$ or K$^+$ between the sheets of MnO$_6$ octahedra. λ-MnO$_2$ is a 3D spinel structure.

Since the energy stored in MnO$_2$ relies on the insertion/extraction of protons or cations in MnO$_2$, the crystallographic structures with sufficient space to accommodate these ions play crucial role in determining the electrochemical properties. Brousse et al.[103] first reported the systematic comparison of the capacitive properties of MnO$_2$ with five different types of crystal structures. They found that the capacitance of the MnO$_2$ was clearly dependent upon the tunnel sizes of different crystalline structures, More significantly, the tunnel sizes of 1D α-MnO$_2$ (4.6 Å) and 2D δ-MnO$_2$ (7 Å) are suitable for fast insertion of hydrated K$^+$ cations (3 Å), leading to relatively high capacitance values (110 F g^{-1}) considering their moderate BET surface area of 17 m^2 g^{-1}. However, 1D tunnel structure such as λ or β-MnO$_2$ provides only a pseudofaradaic surface capacitance of less than 110 μF cm^{-2} since their tunnel sizes are smaller than the hydrated K$^+$ cations, thus limiting the diffusion process. 3D tunnel structure such as λ-MnO$_2$ with a more open three-dimensional (3D) structure permits partial cationic diffusion, exhibiting some intermediate behavior between 2D birnessite and 1D tunnel structures. The results in their work suggest that the tunnel space should be sufficiently large to accommodate a high rate insertion/extraction of the electrolyte ions for charge storage. A similar conclusion was reported by Munichandraiah[106] that the specific capacitance measured for MnO$_2$ electrode is found to depend strongly on the crystallographic structure, and it decreases in the following order: α ≈ δ > γ > λ > β. A wide tunnel size and large interlayer separation of the crystalline structure are ascribed as favorable factors for high specific capacitance. A specific capacitance value of 297 F g^{-1} is obtained for α-MnO$_2$, whereas it is 9 F g^{-1} for β-MnO$_2$. A wide (~4.6 Å) tunnel size and large surface area of α-MnO$_2$ are ascribed as favorable factors for its high capacitance. A large interlayer separation (~7 Å) also facilitates insertion of cations in δ-MnO$_2$ resulting in a specific capacitance close to 236 F g^{-1}. A narrow tunnel size (1.89 Å) does not allow intercalation of cations into β-MnO$_2$. As a result, it provides a very small specific capacitance.

However, Ghodbane et al.[99] found that the relationship between specific capacitance and tunnel sizes of various crystal structures do not always follow the rule described above. They prepared a series of MnO$_2$ allotropic phases and conducted a systematic study dealing with the

crystal structure effects on the charge-storage properties in MnO_2 electrode materials. The results show that the 3D spinel λ-MnO_2 exhibits the highest specific capacitance (241 F g^{-1}) followed by 2D δ-MnO_2 (225 F g^{-1}), and finally, the 1D tunnel structures exhibits the poorest electrochemical performance. For the 1D tunnel group, the larger the cavity, the larger the measured capacity. However, the Ni-todorokite compound exhibits a poor electrochemical performance despite its large 3×3 channel size. This is due to the high stability of solvated Ni ions inside the channel cavity that hinder the ionic diffusion through the cage. However, the overall trend is somewhat identical (i.e. specific capacitance increases with an increase in the tunnel size).

Therefore, the charge storage process is not only confined to the crystal structures, but is also affected by other factors, such as the specific surface area of electrode materials, the electric conductivity, and the ionic conductivity. These factors are playing important roles in affecting the final capacitive property, which make it difficult to compare the specific capacitance by direct comparison of the tunnel sizes of different crystal structures.

2.3 Morphology

The specific capacitance is closely related to the morphology of the electrode, but there have been few systematic studies on morphology-dependent electrochemical properties. Different morphologies result in different specific surface area and the surface to volume ratio which may lead to different specific capacitance. Many different morphologies of MnO_2 have been synthesized and the corresponding electrochemical properties are investigated. Depending on the morphology, the obtained specific surface area of the MnO_2 nanostructures is in the range from 20 to more than 200 m^2 g^{-1}, thus altering the specific capacitances of various MnO_2 nanostructures.

Several morphologies of MnO_2 and their effects on capacitive property are discussed in this part. The first one is the one dimensional nanostructured MnO_2 with short transport/diffusion path lengths for both ions and electrons, offering large specific surface areas, and thus resulting in high capacitance.[111] For example, Wu et al.[112] reported the synthesis of MnO_2 nanorods (15-35 nm in diameter) and MnO_2 nanowires (8-16 nm in diameter). The electrochemical result showed that the nanowires exhibited a higher specific capacitance (350 F g^{-1}) than that of nanorods (243 F g^{-1}) when tested under the same condition. They concluded that the MnO_2 nanowires electrode has the

smallest diameter which could provide more active sites for charge transfer and shorten proton diffusion, therefore benefit high-rate charge/discharge. Other examples are the MnO_2 nanobelts and nanotubes.[87, 113] Both of them offer large surface area and provide conductive ways for ions, leading to enhanced capacitive properties. Furthermore, MnO_2 nanotubes can also accommodate large volume changes during the charge-discharge cycle and thereby improve the life of the electrode.[87] The second type of MnO_2 morphology is hollow spheres and hollow urchins. For example, Xu et al.[114] synthesized α-MnO_2 hollow spheres and hollow urchins via a simple hydrothermal process without using any template or organic surfactant. The hollow sphere or urchin structured MnO_2 materials possess a high loosely mesoporous cluster structure with high specific surface area, which leads to enhanced rate capacity and cycling stability. The third morphology is MnO_2 thin film, which is always fabricated as a robust hybrid MnO_2 electrode for achieving large areal capacitances. Yi and coworkers reported a facile synthesis of a robust MnO_2 thin film involving agarose gel-mediated electrodeposition.[115] The resulting electrode exhibited, not only an enhanced areal loading capacity (52.55 mF cm^{-2}), but a high utilization rate of MnO_2 as well. These improvements can be explained by a robust film structure and excellent contact with the metallic current collector. The fourth morphology is MnO_2 nanopillar array, which enhances the surface area nearly 4.5 times compared to that of the planar electrode and the structural stability is improved during the intercalation and de-intercalation process, thus leading to remarkable enhancements in specific capacitance, charge/discharge ability, as well as cyclic stability.[116] The fifth morphology is 3D porous MnO_2 nanostructure, which have gained more and more attention because of their advantages over the bulk counterparts such as higher surface area and less dead volume. These characters are beneficial for reducing the ion diffusion resistance and optimizing the transport kinetics, which could ensure that MnO_2 possesses both high energy density and power capability.[117]

As the functionalities of nanomaterials are largely affected by their structures, especially in an electrode, the morphologies of nanomaterials directly affect their surface areas interacting with the electrolyte. The rational manipulation of the morphologies of nanostructured MnO_2 electrodes with high specific surface area and porous structure seems to be very promising in further improvement of the performances of electrodes.

2.4 Conductivity

The conductivity of the electrode material is a vital factor. During the charging process, the electrode-electrolyte interface is balanced by the counter ions from the electrolyte to storage charges. It is crucial to control the electrical conductivity of the MnO_2 electrodes in order to achieve the high specific capacitance and rate capability. It can be observed that the resistance to electron conduction will be more noteworthy in an electrode with low conductivity when the charge/discharge rate increases, which would result in the localized charge/discharge process in a limited volume near the current collector, leading to the low specific capacitance and low rate capability. However, it is highly challenging to improve the capacitive property of MnO_2 due to its low electrical conductivity ($\sim 10^{-5}$–10^{-6} S cm^{-1}). In this case, incorporation of other metal elements (Cu, Ni, Co, Fe, Al, Zn, Mo and Sn) into MnO_2 could be an effective way to enhance their electrical conductivity and charge-storage capability.[77, 118-121] The electrochemical properties after doping indicate that the manipulation of defect chemistry by the chemical modification has significant influence on the electrical conductivity and, in turn, on the specific capacitance and rate capability. In addition to doping, the utilization of the carbon black as the conductive agent in the MnO_2 electrode and the design of free-standing MnO_2-based nanocomposite[122, 123] using the conducting polymers or conductive carbon as supporting substrates can be the promising solutions to improve the conductivity of MnO_2 electrodes. The recent efforts are mostly focused on depositing various MnO_2 nanostructures onto highly conductive porous substrates by using a variety of approaches, such as thermal deposition, chemical deposition and electrochemical deposition.

In summary, to achieve high specific capacitance and rate capability for supercapacitors, MnO_2-based electrodes can be modified by metal ions doping and depositing onto conducting substrates with high surface area and porous structure.

2.5 Mass loading

In general, the specific capacitance decreases with increasing mass loading of the MnO_2 electrode because large mass loading may cause the lower electrical conductivity, limited

accessing of electrolyte ions and higher series resistance due to longer transport paths for the diffusion of protons. Kang et al.[124] studied the effect of MnO_2 loading on the electrochemical performances by cyclic voltammetry (CV), impedance measurements and galvonostatic charging/discharging technique. The average specific capacitance decreases linearly from 539 to 188 F g^{-1}, while the corresponding mass loading of MnO_2 deposits increases from 0.33 to 3.41 mg cm^{-2}. The results show that an ultrathin MnO_2 deposits are indispensable to achieve better electrochemical performance. Another example is the investigation of the electrochemical performance of the carbon nanotube/MnO_2/conducting polymers ternary composite electrodes with different MnO_2 mass loading.[125] The specific capacitance of the electrode decrease from 481 to 374 F g^{-1} with the corresponding MnO_2 mass loading range from 0.71 to 3.11 mg cm^{-2}. In addition, a conceptually new colloidal method for the fabrication of MnO_2-based composite with high surface area carbon was proposed by Zhitomirsky's group to obtain relatively high material loading electrodes.[126, 127] To date, most reported research works of MnO_2 electrodes having good electrochemical performances showed a small mass loading of nanoscale MnO_2 (< 1 mg cm^{-2}) due to the limited supporting surface area or non-uniform porous structure of the conductive substrates.[116, 128-135] However, large mass loading of active materials are needed for achieving high power and energy performance of the capacitor device in practical application. Therefore, applying optimal substrates that provide large specific surface areas for high mass loading of active materials and good electric conductivity for full utilization of MnO_2 would be a promising route.

2.6 Electrolyte

Electrolyte is an indispensable element in capacitors since the positive and negative electrodes are interconnected by an electrolyte that determines the charge transport during the charge/discharge process. Up to now, there are three types of electrolytes that have been used in the MnO_2-based SCs, which are aqueous electrolytes, organic electrolytes, and ionic electrolytes, respectively. Among these three types of electrolytes, aqueous electrolytes are the most widely-used electrolytes since they can provide higher ionic concentration and smaller solvated ions which could promote high conductivity and power delivery. However, a large disadvantage is

their small voltage window below 1.2 V because water molecules start to decompose above this voltage, which thus results in the low energy density since the energy density is proportional to the square of the voltage. To solve this problem, organic electrolytes with higher voltage window up to 1.5-2.0 V have been used, which gives rise to energy densities six to nine times that of aqueous electrolytes.[136] However, the organic electrolyte generally exhibits a poor ion conductivity in comparison with the aqueous electrolyte,[137] thus leading to a low power density. Moreover, the use of organic electrolytes also brings in environmental concerns. A further increase in voltage window can be achieved by using the ionic electrolytes. A potential window of 3.0 V of MnO_2 asymmetric supercapacitor have been successfully fabricated by using different kinds of ionic electrolytes as the electrolyte,[138, 139] which also exhibited a high energy density of more than 163 Wh kg^{-1}. Nevertheless, practical applications of ionic electrolytes still seem difficult as a number of limitations such as high viscosity and poor wettability with electroactive materials are yet to be overcome.

3. Synthesis of MnO_2 nanostructures for SCs

Nanostructured MnO_2 electrode materials have received extensive interest due to their potential in improving the performance of SCs. It has been demonstrated that the performance of supercapacitor depends on not only the micro-structure but also the morphology of the active material. Hence, control over the dimension and morphology of the electrode materials is very important for manipulating its electrochemical properties.[140] The most promising and extensively used method for achieving novel structures is self-assembly process. Much effort has been focused on the self-assembly of low-dimensional building blocks into hierarchical structures.[141-143] To date, many self-assembly processes driven by chemical or physical principles have been developed to construct unique structures by different methods such as template-assisted method and template-free method.

3.1 Hard template method

Hard templates are those materials which are either used as scaffolds for the deposition or employed not only as shape-defined templates, but also as chemical reagents that react with other

chemicals to produce desired nanomaterials. In the development of various MnO_2 nanostructures, hard template method is widely used, and coupled with solvothermal/hydrothermal method. There are quite a lot of hard templates have been used for the synthesis of MnO_2 nanostructures, such as SiO_2 spheres,[82] mesoporous silica,[144] naturally-existing diatomite,[145] porous anodic aluminum oxide (AAO),[146] polycarbonate membrane (PC),[87] carbon spheres,[147] carbon nanotubes.[148] For example, Tang et al.[82] synthesized the hierarchical hollow MnO_2 nanospheres by a template-assisted hydrothermal process. In this work, SiO_2 spheres were used as the template to obtain the $SiO_2@MnO_2$ core-shell nanospheres, and then the hollow MnO_2 nanospheres were obtained after etching away the SiO_2 core in the NaOH solution. The as-prepared hollow MnO_2 nanospheres exhibited good capacitive behavior (299 F g^{-1}) and cycling stability (97.6% retention after 1000 charge/discharge cycles) in a neutral electrolyte system. Using the same strategy, mesoporous MnO_2 with uniform nanorod morphology has been synthesized using mesoporous silica SBA-15 as the template.[149, 150] The electrochemical properties of the prepared MnO_2 material are studied using cyclic voltammetry in a mild aqueous electrolyte, which shows that such a mesoporous MnO_2 nanostructure has a high specific capacitance of 258 F g^{-1} and a good reversibility due to its favorable phase and hierarchically porous structure as well as high surface area. The naturally-occurring diatomite with an extraordinary 3D structure, is one of the promising templates for the preparation of porous nanostructures, because of its high porosity, low in bulk density, stable in chemical property, and large in specific area.[151, 152] Recently, different types of hierarchical hollow MnO_2 patterns with both a large surface area and a 3D structure are successfully prepared by a diatomite template-assisted hydrothermal process (Fig. 4).[153] The proposed process is based on hydrothermal reaction where in the first step $KMnO_4$ is used to obtain the nanostructured layer of MnO_2 on the surface of diatoms. In the second step, diatom silica is removed and MnO_2 with diatom preserved shape and morphology is achieved. The electrochemical characterization of the MnO_2 diatom replicas used as electrodes for the supercapacitors showed a high specific capacitance (371.2 F g^{-1} at a current density of 0.5 A g^{-1}), good cycling stability (93.9% rentention after 2000 cycles) and rate capability (54.7% capacitance retention). However, these silica-based hard templates can be just used for the synthesis of MnO_2 powders which are less suitable for the preparation of MnO_2 thin film electrodes. This is a serious

disadvantage of the silica-templating methods, limiting their usefulness in the development of numerous thin film-based light-weight supercapacitor devices with nanoporous MnO_2 components.

Anodic aluminum oxide (AAO) film is also one of the attractive templates since it possesses very regular and highly anisotropic porous structures with pore diameters ranging from below 10 to 200 nm, pore length from 1 to 50 μm, and pore densities in the range 109 to 1011 cm^{-2}.[154] The pores have been found to be uniform and nearly parallel, which is useful for the synthesis of one dimensional MnO_2 nanostructures, affording short ion diffusion paths and fast kinetics during the electrochemical reactions. Using the AAO as the template, MnO_2 nanotubes and nanowires arrays can be prepared by a sol-gel method or electrodeposition method (Fig. 5).[155-159] The as-prepared MnO_2 nanotube and nanowire arrays are investigated as electrode materials for supercapacitor applications and show a good electrochemical performance. However, the cost of the AAO templates limits the large-scale application for the production of well-organized MnO_2 nanostructured electrodes. In addition to the AAO template, polycarbonate membrane (PC) with different pore diameters was also developed to prepare MnO_2 nanotubes. For instance, Huang et al.[87] first reported that porous MnO_2 nanotubes comprised of nanosheets could be fabricated by using polycarbonate membrane as the template after hydrothermal reaction (Fig. 6). The diameter and thickness of nanotubes can be controlled by choice of the membrane pore size and the chemistry. The specific capacitance of the MnO_2 nanotubes-based electrode was 365 F g^{-1} at a current density of 0.25 A g^{-1} with capacitance retention of 90.4% retention after 3000 cycles in a three-electrode cell system. Similarly, MnO_2 tubular arrays with different size and morphologies have been synthesized by tuning the size of PC template and reaction temperature.[160] The results showed that the sample of MnO_2-200-100 which is synthesized from the PC template with 200-nm diameter at a temperature of 100 °C exhibited the best performance among those MnO_2 nanotubes. MnO_2-200-100 exhibits a porous structure with an inner diameter of 80 nm. Such porous structure ensures the efficient electrolyte diffusion throughout the tubes, leading to the enhanced capacitive property. Moreover, carbon nanospheres, nanotubes, and nanofibers can be used as sacrificial template for the synthesis of hollow MnO_2 nanostructures.[161-164] The morphology of MnO_2 nanostructures can be adjusted by changing the reaction time or annealing process.

In summary, hard templates can be used for the controlled synthesis of ordered MnO_2 nanostructures, which could be quite useful for the scientific understanding of some fundamental issues. However, these templates always suffer from high cost and complicate removal process through acid or base etching and calcinations. Therefore, a great challenge is the development of low-cost and simple templating methods to fabricate unique MnO_2 nanostructures.

3.2 Soft template method

Soft template method is also applied in the synthesis of MnO_2 nanostructures. Soft templates include surfactants, flexible organic molecules, microemulsions or block copolymers,[165] which can act as the structure-directing agents in the formation of MnO_2. Compared to the hard template method, soft-template method has advantages such as simple process and relatively low cost. During the self-assembly process in the synthesis of MnO_2 nanostructures, the surface tension can be reduced largely by surface adsorption of the surfactant unique amphiphilic structure. In addition, surfactant long molecular chains generate steric effect which can reduce the agglomeration phenomenon, thus controlling particles size and maintaining high specific surface area. Furthermore, owning to its self-assembled function, surfactant can be used as micro-reactors to regulate and control materials morphology and structure of MnO_2, thus to improve its capacitance performance.[166] Up to now, various MnO_2 nanostructures have been synthesized by different surfactants, such as sodium dodecyl sulfate (SDS),[167-171] hexadecyl trimethyl ammonium bromide (CTAB),[172-174] polyvinylpyrrolidone (PVP),[175-178] Pluronic P123 (PEO-b-PPO-b-PEO triblock copolymer),[179-181] tetraoctylammonium bromide (TOAB),[182-184] and polyethylene glycol (PEG).[185-187]

Yin's group synthesized single-layer MnO_2 nanosheets *via* a redox reaction between $KMnO_4$ and sodium dodecyl sulfate (SDS). The gradual hydrolysis of SDS is found to be the key factor for the successful formation of single-layer nanosheets. SDS not only serves as the precursor of dodecanol to reduce $KMnO_4$, but also aids the formation of single-layer MnO_2 nanosheets as a structure-inducing agent.[188] Single-crystal α-MnO_2 ultralong nanowires with a length of ~40 μm were synthesized by Hu's group using a PVP assisted hydrothermal route.[189] With the decomposition of $KMnO_4$, the MnO_2 nuclei take place in the solution and then adsorb on the PVP

long chains, which can act as a template and stabilizer for the MnO_2 crystal growing, preventing the precipitation and aggregation of MnO_2 nuclei. Thus, the PVP and MnO_2 nuclei assemble together. As the reaction proceeds, the MnO_2 NWs are formed due to Ostwald ripening. The as-prepared ultra long α-MnO_2 nanowires exhibited an enhanced specific capacitance of 345 F g^{-1} at 1 A g^{-1} with high rate capability and good cycling stability. Triblock copolymer P123 is one of the popular structure-directing agents, which acts as a soft template during the preparation of MnO_2 nanostructures. When Mn^{2+} ions are added into the P123 solution, Mn^{2+} first coordinates with the polymer to form Mn^{2+}-P123 complex and then MnO_2 particles grow along the polymer chains when Mn^{2+} is oxidized by $KMnO_4$, forming nanorods that pile up to secondary particles. Wang et al.[190] synthesized porous MnO_2 via an ultrasound-microwave-intensified precipitation method with the soft template of triblock polymer P123. The MnO_2 particles showed a loose sphere-network structure with tiny pores (4−5 nm in diameter) inside the spheres, and architectural mesopores and macropores among the secondary particles. The specific capacitance of the as-prepared MnO_2 was as high as 214 F g^{-1} and the capacitance reduction was less than 10% after 5000 cycles.

Although conceptually simple and versatile, soft template has its own limitations. It usually requires surface modification of the template and the template removing process is time-consumming. Soft template often has the difficulty to control the size, shape and uniformity of the product. Besides, the residual surfactant may envelop MnO_2 particles, increase the ion resistance and reduce charge storage capability of MnO_2 electrodes.[166] Therefore, it still remains a major challenge to develop a facile low cost, and environmental benign method for the controllable synthesis of MnO_2 for supercapacitors.

3.3 Template-free method

Apart from the above mentioned template-assisted methods, there are many other techniques that can be used to synthesize MnO_2 nanostructures, such as hydrothermal/solvothermal method, sol-gel method, microwave-assisted method, electrodeposition method, and electrospinning method.

3.3.1 Hydrothermal/solvothermal method

Hydrothermal/solvothermal method has been widely used to synthesize MnO_2 nanostructures with specific sizes and morphologies. Hydrothermal and solvothermal method are similar synthetic methods, except for the reaction medium. They both apply high temperature and high pressure to promote the reaction. The temperature adopted is often higher than 100 ^{o}C in order to reach the pressure of vapor saturation, so that autogenous pressure will be developed in a closed system. In addition to the temperature, other experimental factors, such as the type and amount of solvent and dissolved salts, also have significant effect on the morphology and structure of prepared MnO_2 products.[191] Up to now, the hydrothermal/solvothermal method has achieved great success in the preparation of MnO_2 with various nanostructures, such as nanowires/nanorods/nanobelts,[192-200] micro/nanoflowers,[201-204] micro/nanospheres,[205-209] nanotubes,[210-212] nanosheets,[213-215] nanoparticles,[216-218] and so on. Recently, Wei et al.[219] synthesized a novel 2D β-MnO_2 network with long-range order through a one-pot hydrothermal reaction (Fig. 7). Such a novel structure makes efficient contact of β-MnO_2 with electrolyte during the electrochemical process, decreases the polarization of the electrode and thus increases the discharge capacity and high-rate capability. The as-prepared 2D β-MnO_2 network exhibited a specific capacitance of 453 F g^{-1} at a current density of 0.5 A g^{-1}.

3.3.2 Sol-gel method

Sol-gel technique also attracts significant attention for the synthesis of MnO_2 because it offers controllable purity, composition, homogeneity of the products. It can be briefly summarized to be the transformation from the manganese precursor solution to solid MnO_2 powders or thin films. Although there are many merits of sol-gel method, its large scale application is still hindered by the requirement of large amounts of organic solvents and reagents. Pang et al.[98, 220] first used the sol-gel technique to prepare MnO_2 thin film electrodes for capacitors. The cyclic voltammograms of the sol-gel-derived MnO_2 films showed a specific capacitance values as high as 698 F g^{-1}. In 2003, Reddy et al.[221] used a sol–gel method to get two forms of MnO_2, namely xerogel and ambigel. After that, various MnO_2 nanostructures have been synthesized by sol-gel method with different precursors.[222-225] In the recent study by Sarkar et al.,[226] a mesoporous manganese oxide film was fabricated by a sol-gel method followed by annealing process. The amorphous MnO_2 film shows a specific capacitance of 360 F g^{-1} at current of 0.82 A g^{-1} and a large density of 48.8

Wh kg^{-1} at a power density of 1.16 W kg^{-1}.

3.3.3 Microwave-assisted method

Microwave-assisted method has been used in the preparation of inorganic materials due to its wide applicability such as short reaction times (can reduce the reaction time often by orders of magnitude), low cost, and high yields.[227, 228] Unlike conventional oil bath or hydrothermal heating, an inverted temperature gradient takes place during the microwave-assisted process. The rapid dielectric heating is generated internally within the material due to applied microwave radiation with a commonly used frequency of 0.3 to 2.45 GHz.[229] Microwave-assisted synthesis has been adopted to prepare MnO_2 with highly uniform microstructures.[230-234] For example, Nyutu et al.[230] prepared α-MnO_2 nanofibers in mixed aqueous and dimethyl sulfoxide solvent by use of microwave reflux. This process required about 10 min to start crystallizing the α-MnO_2 phase and about 90 min to fully crystallize the phase. Yu et al.[231] has developed a microwave-assisted emulsion process to synthesize one-dimensional (1D) birnessite-type MnO_2 nanostructures. As a consequence of the small size, such MnO_2 nanostructures exhibit a high specific capacitance of 277 F g^{-1} at the current density of 0.2 mA cm^{-2}. Zhang et al.[233] reported that γ-MnO_2 nanoparticles and α-MnO_2 urchin-like nanostructures have been successfully synthesized by the microwave-assisted reflux as short as 5 min under neutral and acidic conditions, respectively. γ-MnO_2 nanoparticles obtained from the neutral condition exhibited a capacitance of 311 F g^{-1} at a current density of 0.2 A g^{-1}, which is much higher than that of α-MnO_2 urchin-like nanostructures (163 F g^{-1}).

In microwave synthesis, the morphologies and phases are difficult to be controlled. An emerging attractive concept is to combine the microwave method with hydrothermal method. The coupled microwave-hydrothermal method possesses advantages of both hydrothermal and microwave conditions, which can dramatically reduce the reaction time from 10 h or even several days down to 30 min, and also keep the ability to control over the morphology and size distribution of the products.[235] Ming et al.[236] reported the rapid and scalable synthesis of birnessite-type MnO_2 nanospheres by the microwave–hydrothermal method at 75 °C for 30 min under low pressure. The electrochemical test results show that the specific capacitance is 210 F g^{-1} at 0.2 A g^{-1} in 1.0 M Na_2SO_4 electrolyte, and the SC retention and coulombic efficiency are over

96% and 98% respectively after 300 cycles at 1.6 A g^{-1}. Using the similar method, Xue's group reported a coupled microwave-hydrothermal process to crystallize polymorphs of MnO_2 such as α-, β-, and γ-phase samples with plate-, rod-, and wire-like shapes, using a controllable redox reaction in $MnCl_2$-$KMnO_4$ aqueous solution system.[237]

3.3.4 Electrodeposition method

The electrodeposition method proceeds in the solution containing the targeting ions which will be deposited on the anodic or cathodic electrode substrates by controlling the deposition rate, and thus the target material films with different density and morphologies will be obtained.[238, 239] The electrodeposition technique has been widely used because of its simplicity, the elimination of polymer binders, non-polluting nature and modest reaction conditions.[240-243] In fact, the electrodeposition of MnO_2 can be generally divided into galvanostatic (GS),[244, 245] potentiostatic (PS),[246] and cyclic voltammetric (CV)[247] techniques according to the different styles of applied voltage or current. These different deposition routes significantly influence the surface morphology and crystal structure of the final product, which are also related to the capacitive properties. Using the electrodeposition method, many interesting MnO_2 nanostructures or films have been prepared. For example, manganese oxide nanostructures are synthesized by the pulse reverse electrodeposition technique for electrode materials of SCs. The morphology and composition of MnO_2 can be controlled by the pattern of the applied potential.[248] Dupont et al.[249] reported the anodic electrodeposition of manganese dioxide from a solution of 0.01 M $MnSO_4$ in 0.1 M H_2SO_4 onto a platinum substrate. Electrochemical data indicates that the dilute acid solution favors the formation of MnO_2 via a MnOOH intermediate (hydrolysis).

A facile 3D hierarchically structured MnO_2 nanowires supported on hollow Ni dendrites was prepared via an electrodeposition method.[250] The resultant 3D hierarchical Ni@MnO_2 structure is highly porous and likes a forest of pine trees grown vertically on a substrate (Fig. 8). In addition, the as-prepared MnO_2 electrode shows a remarkable high-rate performance (1097 and 766 F g^{-1} at discharge current densities of 12.5 and 100 A g^{-1}, respectively). Yang et al.[251] has fabricated nanostructured porous MnO_2 film on Ni foam substrate via a cyclic voltammetric electrodeposited route for the first time. The obtained MnO_2 film had a 3D network structure and a high mass loading from 6 to 18 mg cm^{-2}. This material achieved a maximum specific capacitance of 2790

mF cm^{-2} at 2 mA cm^{-2} and 864 mF cm^{-2} at 20 mA cm^{-2}, and the specific capacitance can be retained above 90% after 1000 cycles at 5 mA cm^{-2}. Hu and co-workers prepared a porous hybrid manganese oxide electrode on porous electroformed nickel by applying a current density of 1 to 14 mA cm^{-2} in a solution bath of 0.1 M manganese acetate and 0.1 M sodium sulphate.[245] With increasing deposition current densities, the manganese oxide electrode changed from porous and fibrous to a denser film. The relationship among the deposition parameters, morphology and electrochemical characteristics of MnO_2 electrodes is also discussed.

3.3.5 Electrospinning method

Electrospinning method is a versatile technique to produce nanofibers with controllable diameter, morphology and surface topology from a variety of organic and inorganic materials. It gives the impression of being a very simple and, therefore, easily controlled technique for the production of fibers with dimensions down to the nanometer range. First, polymers will be surveyed as fiber-forming materials. Later, materials such as metals, ceramics, and glasses will be considered as fiber precursors.[252] Electrospinning mainly makes use of the electrostatic repulsions between surface charges to reduce the diameter of a viscoelastic jet or a glassy filament. A number of functions can be incorporated into the nanofibers by electrospinning to expand their potential applications with the only prerequisite that the second phase can be soluble or well dispersed in the initial solution.[253] This simple, cheap, and scalable method has been successfully applied to produce MnO_2-based nanostructures.[175, 254, 255] Li et al.[255] adopted the electrospinning method to fabricate ordered nanofibers with the MnO_2 precursor on the glass-collector with two parallel grounded electrodes. The solution used for this step was a mixture of 8 wt% poly(vinylpyrrolidone) (PVP, Mw≈360000, Sigma-Aldrich) and 0.2 g $Mn(CH_3COO)_2 \cdot 4H_2O$ in a 4 mL alcohol–deionized water solvent mixture (volume ratio=3:7). The as-fabricated supercapacitor possesses an electrochemical capacitance as high as 645 F g^{-1} at a current density of 0.5 A g^{-1}, as well as good stability, retaining 95% of its initial capacitance after 2000 consecutive cycles. Zhang and coworkers fabricated the manganese oxide/carbon nanofiber (MnOx/CNF) composites as freestanding electrodes through incorporating different manganese sources of nanostructured MnO_2 or $Mn(CH_3COO)_2 \cdot 4H_2O$ into polyacrylonitrile (PAN) solution by electrospinning and a subsequent carbonization method.[175] The resulting MnO$_x$/CNFs demonstrated excellent

electrochemical performance with great rate capability, low internal resistance and long-term cycling stability.

Morphology, crystallinity and microstructures are important factors in affecting the final electrochemical performance of MnO_2 electrodes. It is extremely crucial to explore the optimal synthesis method. In this chapter, the fundamentals and different methods for the synthesis of various MnO_2 structures have been summarized. Three types of strategies, including hard-template, soft-template and template-free methods have been reviewed and discussed in detail. Among these methods, hard template method involved the deposition of MnO_2 on various hard templates (porous silica, AAO, PC and carbon nanotubes), followed by the removal of these hard templates by either dissolution or calcination. Hard template method can be highly useful for the synthesis of ordered MnO_2 nanostructures, but it always suffers from high cost and complicated removal process through acid or base etching and calcinations. Soft template method is also employed for the synthesis of various MnO_2 structures by altering the type and concentration of the surfactants. The use of the soft template method always results in the formation of mesoporous MnO_2, which makes them promising candidates for supercapacitor electrodes. Soft template method can overcome some disadvantages of hard template method but the control over size, shape and uniformity of the MnO_2 is limited in comparison to hard templating. By contrast, template-free methods are investigated in the synthesis of MnO_2 nanostructures considering the fact that template removal is a critical problem in the template-based methods, which makes it complicated. Furthermore, the composition, defect chemistry, various morphologies and even crystal structure can be manipulated through adjusting different template-free methods.

4. MnO_2-based composite for SCs

4.1 MnO_2-carbon composites for SCs

Forming MnO_2-based hybrid structures with highly conductive carbons is one of the most adopted methods to improve the capacitor performance of MnO_2 electrodes whose poor conductivities limit their capacitance, cycling life and rate performance. Carbon materials (carbon nanotubes, graphene, porous carbon, carbon nanofibers, carbon spheres, carbon nanofoam/aerogel) are promising candidates to couple with MnO_2 nanostructures in view of their good electrical

conductivity and excellent mechanical/electrochemical stability.

4.1.1 MnO_2-carbon nanotubes (CNTs) composite

CNTs are the most representative nanostructured carbons with one dimensional tubular structure and exhibit outstanding structural and electrical properties such as high electrical conductivity, high mechanical strength, high chemical stability, and high activated surface areas, which hold great promise in constructing MnO_2-CNT architectures with enhanced energy storage capabilities. The incorporation of MnO_2 on CNT architectures can be realized through many effective synthetic protocols such as electrodeposition technique, hydrothermal treatment, microwave-assisted method, chemical co-precipitation, thermal decomposition.[256-260] Zhang et al.[261] reported the controllable synthesis of manganese oxide nanoflower/carbon nanotube array (CNTA) composite electrodes with hierarchical porous structure, large surface area, and superior conductivity by electrodeposition technique. This binder-free manganese oxide/CNTA electrode presents good rate capability (50.8% capacity retention at 77 A g^{-1}), high capacitance (199 F g^{-1} and 305 F cm^{-3}), and long cycle life (3% capacity loss after 20000 charge/discharge cycles). Li et al.[262] prepared the MnO_2/CNTs composite by modified chemical method in a mild one-pot reaction process. The MnO_2 layer with about 50 nm thick attaches the sidewalls of the inner nanotubes uniformly. The composite exhibits a specific capacitance of 201 F g^{-1} at 1 A g^{-1}, with good rate capability (140 F g^{-1} at 20 A g^{-1}) and capacitance retention upon cycling (no decay after 10000 cycles).

Recently, Mai and coworkers developed a flexible, low-cost and high-performance hybrid electrode based on MnO_2 nanotubes (NTs) and carbon nanotubes (CNTs) by employing a facile vacuum-filtering method.[263] The CNTs in the film not only provide a mechanical reinforcement effect, but also act as an electron transport medium. The as-synthesized capacitor devices by the freestanding CNT/MnO_2 NT hybrid electrodes exhibited an excellent volumetric capacitance of 5.1 F cm^{-3} and a high energy density of 0.45 mWh cm^{-3} for the entire supercapacitor volume. Huang et al.[264] fabricated the three-dimensional carbon nanotubes@MnO_2 core–shell nanostructures grown on Ni foam for binder-free capacitor electrodes by a floating catalyst chemical vapor deposition process and a facile hydrothermal approach. Ultrathin layered MnO_2 nanosheets are uniformly coated on the surface of the carbon nanotubes (CNTs), directly grown on

Ni foam (Fig. 9). This unique well-designed binder-free electrode exhibited a high specific capacitance (325.5 F g^{-1} at a current density of 0.3 A g^{-1}), good rate capability (70.7% retention), and excellent cycling stability (90.5% capacitance retention after 5000 cycles). However, this scalable synthesis of MnO$_2$-coated CNT may cause the problems related to carbon consumption in the redox reaction and collapse of the carbon–carbon bonding structure of CNT that degrade the electrical conductivity. To decrease the chemical degradation of CNT, Shi et al.[265, 266] developed a new approach by using N-doped activated carbon layer as a sacrificial material to protect the CNT in the composite, which also allowed a relatively high mass content of MnO$_2$. The approach offered the advantages of small size of MnO$_2$ nanoparticles, good electrical contact of MnO$_2$ and MWCNT and fibrous microstructure of the material. The electrochemical results showed a remarkably high specific capacitance of 6.29 F cm^{-2} (311.7 F g^{-1}) at a mass loading of 20 mg cm^{-2}, good capacitance retention at high charge/discharge rates and good cycling stability.

4.1.2 MnO$_2$-graphene composite

Graphene, a two-dimensional carbon layer with one atom thick, is attractive for developing high-performance SCs due to its large theoretical specific area (2630 m^2 g^{-1}), high electrical conductivity (10^4 s cm^{-1}), abundant raw material resources, and good electrochemical stability.[267] These fascinating properties have motivated extensive efforts to use graphene as the conductive supporting materials for MnO$_2$-based SCs. The combination of graphene and MnO$_2$ can generate a synergistic effect to overcome their inherent drawbacks, thus improving the capacitive performance. Up to now, various hybrid structures such as graphene nanosheets/MnO$_2$,[268-274] graphene nanoribbon/MnO$_2$,[275-277] partial-exfoliated graphite/MnO$_2$,[278, 279] 3D graphene hydrogel/MnO$_2$,[193, 280, 281] and 3D graphite foam/MnO$_2$[282-284] have been studied. For example, Cheng and coworkers reported the preparation of a graphene nanosheets/MnO$_2$ nanowires composite by solution-phase assembly of graphene sheets and MnO$_2$ nanowires (Fig. 10a).[268] Huang et al.[269] synthesized graphene nanoplate-MnO$_2$ composites by oxidizing part of the carbon atoms in the framework of graphene nanoplates at ambient temperature. Dai et al.[273] reported the fabrication of highly uniform graphene oxide nanosheets/MnO$_2$ nanowire composite on a gram-scale through a hydrothermal process without any catalysts or templates. The results showed that the product consisted of α-MnO$_2$ nanowires with the diameter of 20~40 nm and the length of

0.5~2 μm that were well dispersed on the surfaces of graphene oxide sheets. The electrochemical specific capacitance of GO/MnO$_2$ composite electrode is as high as 360 F g^{-1}. Liu and coworkers demonstrated a novel hybrid material of graphene nanoribbons and MnO$_2$ nanoparticles (GNR-MnO$_2$) by a one-step method.[277] By tuning the amount of oxidant (KMnO$_4$) used in the synthesis process, not only have the pristine CNTs been totally unzipped resulting in the formation of GNR, but also MnO$_2$ nanoparticles have been deposited simultaneously and controllably on the surface or interlayer of GNRs (Fig. 10b). With the GNR–MnO$_2$ hybrid material and pure GNR sheets as the positive and negative electrodes respectively, a high-performance asymmetric supercapacitor, with widened operating potential window (2.0 V) and specific capacitance of 212 F g^{-1}, has been fabricated.

Song et al.[279] developed a synthesizing route to deposit MnO$_2$ nanosheets onto functionalized exfoliated graphite substrate (Fig. 10c). Ultrathin and functionalized graphene sheets anchoring on the graphite provide a large conductive surface area for loading pseudo-capacitive MnO$_2$ nanosheets. The functionalized exfoliated graphite/MnO$_2$ (FEG/MnO$_2$) electrode achieved an excellent areal capacitance of 244 mF cm^{-2}, corresponding to an estimated MnO$_2$ based gravimetric capacitance of 1061 F g^{-1}. The capacitance of FEG/MnO$_2$ preserved 92% of its initial capacitance after 5000 cycles. Li and coworkers reported a facile method to assemble a hierarchical and interconnected reduced graphene oxide/β-MnO$_2$ (rGO/β-MnO$_2$) nanobelt hybrid hydrogel by dispersion of pre-synthesized ultrathin β-MnO$_2$ nanobelts in graphene oxide precursor solution by a hydrothermal reaction (Fig. 10d).[193] The obtained typical rGO/β-MnO$_2$ nanobelt hybrid hydrogel with 54.2% ultrathin β-MnO$_2$ nanobelts exhibits a high specific capacitance of 362 F g^{-1} at a current density of 1.0 A g^{-1}, good rate performance and cycling stability. In addition, the highly conductive three-dimensional graphite network produced by chemical vapor deposition using commercially available Ni foam as the sacrificial template was also investigated as an efficient supporting material for MnO$_2$ deposition.[285] He et al. developed a type of MnO$_2$-coated free-standing, flexible, lightweight, and highly conductive 3D graphene network. High specific surface area (392 m^2 g^{-1}) allows for the   large mass loading of 92.9% MnO$_2$ (Fig. 11).[282] The hybrid flexible electrodes exhibit a high areal capacitance of 1.42 F cm^2 and a high specific capacitance of 130 F g^{-1} (based on the total weight of the electrode). Moreover, the flexible

supercapacitor exhibits an energy density of 6.8 Wh kg^{-1} at a power density of 62 W kg^{-1} with a 1 V potential window. It preserves 55% of its energy density as the power density increases to 2500 W kg^{-1}. These properties were found to be superior to those of other MnO$_2$-based symmetric flexible SCs (Fig. 11d) and can be further improved by an asymmetric supercapacitor design.

4.1.3 MnO$_2$-porous carbon composite

Porous carbon is another attractive supporting material for MnO$_2$ due to its desirable electrolyte transport routes. Yang and coworkers reported the synthesis of a series of MnO$_2$/carbon nanocomposites with varying amounts of ultrathin MnO$_2$ nanofibers grown on a three dimensional ordered macroporous carbon framework via the redox reaction occurring between the KMnO$_4$ solution and the sacrificial carbon substrate.[286] Liu et al.[287] developed the MnO$_2$/porous carbon microspheres with a partially graphitic structure for high performance supercapacitor electrode materials. In this hybrid structure, micro- and mesoporous carbon microspheres were fabricated based on a hydrothermal emulsion polymerization and common activation process. Manganese nitrate was introduced into the pores of the carbon microspheres, followed by thermal treatment to transform it into amorphous MnO$_2$. As a result, the MnO$_2$/porous carbon microspheres as supercapacitor electrodes exhibited excellent electrochemical performance (459 F g^{-1} at 1.0 A g^{-1} and 354 F g^{-1} at 20.0 A g^{-1} in 6 M KOH electrolyte). Li et al.[288] developed a facile strategy for the synthesis of MnO$_2$ nanoflakes/hierarchical porous carbon spheres nanocomposites (HPCs) via a two-step redox process. The external MnO$_2$ nanoflakes with thickness of 10 nm were deposited on the surface of the HPCs, resulting in the formation of hierarchical architecture of the composites. The MnO$_2$ nanoflakes/HPCs composite possessed a capacitance of 417 F g^{-1} at 20 mV s^{-1} with good cycling stability (slightly over 100% capacitance retention after 10000 cycles). Wang et al.[289] reported a simple and industry-scalable approach to prepare the MnO$_2$/3D porous carbon hybrid structure (Fig. 12). The 3D porous carbon not only provided a conductive network to enhance the charge transport and mass transfer during the electrochemical process, but also allowed for a large MnO$_2$ mass loading. As a result, the as-prepared MnO$_2$/3D porous carbon hybrid electrode exhibits a high specific capacitance of 416 F g^{-1} and large areal capacitances of 2.77 F cm^{-2} (Fig. 12e and f).

4.1.4 MnO$_2$-carbon nanofiber composite

Carbon fiber is also a promising backbone for the conformal coating of MnO_2 for SCs. The single carbon fibers can connect with each other to form a conductive network with appropriate pore channels, which give rise to efficient electron and ion transportation. Kang and coworkers reported the synthesis of carbon nanofibers (CNFs)/MnO_2 nanocomposites as freestanding electrodes.[290, 291] The maximum specific capacitance (based on pristine MnO_2) was 557 F g^{-1} at a current density of 1 A g^{-1}. This freestanding electrode also exhibited good rate capability (power density of 13.5 kW kg^{-1} and energy density of 20.9 Wh kg^{-1} at 30 A g^{-1}) and long-term cycling stability (retaining 94% of its initial capacitance after 1500 cycles). Zhi et al.[292] presented highly conductive carbon nanofiber/MnO_2 coaxial cables in which individual electrospun carbon nanofibers are coated with an ultrathin hierarchical MnO_2 layer (Fig. 13). In the hierarchical MnO_2 structure, a 4 nm thick sheath surrounds the carbon nanofiber (CNF) with a diameter of 200 nm, and nano-whiskers grow radically outward from the sheath in view of the cross-section of the coaxial cables, giving a high specific surface area of MnO_2. The MnO_2-carbon nanofiber composite electrode shows a specific capacitance of 311 F g^{-1} for the whole electrode and 900 F g^{-1} for the MnO_2 shell at a scan rate of 2 mV s^{-1}. Chen et al.[92] developed a simple and scalable approach to fabricate a binder-free asymmetric supercapacitor using bacterial-cellulose-derived carbon nanofibers loaded with MnO_2 and nitrogen-doped carbon nanofibers as electrode materials. The optimal device can be reversibly charged/discharged at an operation voltage of 2.0 V in 1.0 M Na_2SO_4 aqueous electrolyte, delivering a high energy density of 32.91 Wh kg^{-1} and a maximum power density of 284.63 kW kg^{-1}, possessing a remarkable cycling stability with approximately 95.4% capacity remaining after 2000 continuous cycles.

4.1.5 MnO_2-carbon sphere composite

Carbon spheres are one of representative nanostructured carbons to serve as the cores to fabricate carbon sphere@MnO_2 core-shell nanocomposites for enhanced electrochemical performance of supercapacitor electrodes.[293-296] Zhao and coworkers prepared MnO_2 nanofibers on graphitic hollow carbon spheres (GHCS) by refluxing GHCS in a $KMnO_4$ aqueous solution.[294] The stoichiometric redox reaction between GHCS and MnO_4^- yields GHCS–MnO_2 composites with controllable MnO_2 content. It is found that these ultrathin MnO_2 nanofibers are vertically grown on the external surface of the GHCS, yielding a composite electrode showing good electron

transport, rapid ion penetration, fast and reversible Faradic reaction, and excellent rate performance when used as supercapacitor electrode materials. Zhao et al.[295] presented a facile, efficient and low-cost preparation of carbon@MnO_2 core–shell nanospheres as the electrode materials for SCs with improved electrochemical performances (Fig. 14). First, the carbon nanospheres were produced by aromatization and carbonization of glucose under hydrothermal condition. Subsequently, the MnO_2 nanoshells can be in situ anchored on surfaces of the carbon spheres through a facile redox reaction between $KMnO_4$ and carbon. By simply controlling the reaction time, various nanostructure MnO_2 shells with different morphologies and crystalline structures are obtained. Typically, the hybrid nanospheres with flower-like birnessite-type MnO_2 shells exhibit a highest capacitance of 252 F g^{-1} (based on the mass of MnO_2) at the scan rate of 2 mV s^{-1}, and an excellent rate performance with a specific capacitance of 175 F g^{-1} at 100 mV s^{-1}. Recently, Li et al.[296] developed a facile approach to directly grow MnO_2 nanosheets on hollow carbon frameworks with the aid of the redox reaction between $KMnO_4$ and carbon. The hollow carbon spheres were produced through a simple and inexpensive template-directed coating method with resorcinol–formaldehyde (RF) resin as carbon source. Due to the synergistic effect between hollow carbon spheres and MnO_2, the carbon spheres@MnO_2 composites exhibit a high specific capacitance of 306 F g^{-1}, good rate capability, and desirable cycling performance (95.2% after 5000 cycles).

4.1.6 MnO_2-carbon nanofoam/aerogel composite

Carbon nanofoams and carbon aerogel nanoarchitectures are particularly attractive for electrochemical capacitor applications due to their inherent structural characteristics that include high specific surface areas, through-connected networks of mesopores and/or macropores, tunable pore sizes ranging from nanometers to micrometers, durable monolithic, moldable forms, and reasonable electronic conductivity.[297, 298] Manganese oxide is easy to form composite on the surface or in the large aperture of the carbon nanofoams/aerogels due to the physical characteristics, thus the active sites of the MnO_2 electrodes can be optimized and the specific capacitance can be improved. For example, Fischer et al.[297] demonstrated the self-limiting deposition of homogeneous MnO_2 throughout macroscopically thick porous carbon nanofoams. The MnO_2 coating contributes additional capacitance to the carbon nanofoam while maintaining

the favorable high-rate electrochemical performance inherent to the ultraporous carbon structure of the nanofoam. Such a three-dimensional design exploits the benefits of a nanoscopic MnO_2−carbon interface to produce an exceptionally high area-normalized capacitance (1.5 F cm^{-2}), as well as high volumetric capacitance (90 F cm^{-3}). Lv et al.[299] prepared the nano-sized amorphous α-MnO_2-dispersed carbon aerogels (CAs) by liquid phase co-precipitation technique. Filamentous nano-MnO_2 has been formed and homogeneously dispersed among the three-dimensional mesoporous network of CA. The as-prepared MnO_2-dispersed CAs exhibit a specific capacitance of 219 F g^{-1}, and that for MnO_2 ingredient in the composite is as high as 401 F g^{-1}. Tong and coworkers explored a novel route to prepare mesoporous MnO_2/carbon aerogel composites by electrochemical deposition assisted by gas bubbles.[300] The growth rates of deposits can easily be well controlled by deposition potentials, current densities, or salt concentrations. The prepared mesoporous MnO_2/carbon aerogel composites have been successfully employed as supercapacitor electrodes and give a high specific capacitance (515.5 F g^{-1}). Ren et al.[301] presented a facile and scalable method to synthesize MnO_2 loaded carbonaceous aerogel (MnO_2@CA) composites via the hydrothermal carbonaceous process. The obtained MnO_2@CA displays the specific capacitance of 123.5 F g^{-1}. The enhanced capacity of MnO_2@CA nanocomposites could be ascribed to both electrochemical contributions of the loaded MnO_2 nanoparticles and the porous structure of three-dimensional carbonaceous aerogels.

Various carbon materials have been investigated as the supporting material for the deposition of MnO_2 nanostructures due to their outstanding properties, such as high electrical conductivity, chemical stability in both acidic and alkaline medium, and light weight. These features enable carbon materials to be the most popular scaffold materials for fabrication of MnO_2 electrodes. As discussed above, the current MnO_2-carbon composite electrodes are mainly focusing on loading MnO_2 on carbon nanotubes, graphene, porous carbon, carbon nanofiber, carbon spheres and carbon nanofoams. These carbons can act both as high surface area mechanical support and current collector for the active MnO_2 phase to improve the conductivity of the electrode. It is noted that the carbon scaffolds can also act as active materials for charge storage, simultaneously increasing the whole capacitance of the composite electrodes.

However, the largely enhanced specific capacitance of the MnO_2 is due to the relatively low

mass loading of MnO_2, resulting in a low energy density of the overall supercapacitor cell. Besides, the measurement and report of the capacitive property of MnO_2 based electrodes should follow industrial procedures and standards. Therefore, it is essential to optimize the mass loading of MnO_2 materials to achieve high specific capacitance without sacrificing the good conductivity and rate capability in terms of both gravimetric and volumetric bases.

4.2 MnO_2-conducting polymer composite for SCs

Conducting polymers, such as polyaniline (PANI), Poly(3,4-ethylenedioxythiophene) (PEDOT), Polypyrrole (PPy), are also considered as a category of promising supporting materials to couple with MnO_2 for advanced electrochemical energy storage.[302-304] The advantages of conducting polymers mainly include the good conductivity, controllable synthesis, feasibility of forming uniform and porous structures, and the pseudo-capacitive characters. Based on these properties, the combination of conducting polymers with MnO_2 would harvest the synergetic effects between polymers and oxides, thus providing some superiority for the supercapacitor application.

4.2.1 MnO_2-polyaniline (PANI) composite

Polyaniline (PANI) is one candidate for supercapacitor due to its electrochemical reversibility, easy synthesis, high stability, good conductivity, and good stability. By introducing PANI into MnO_2 nanostructures to form MnO_2-PANI composite, the conductivity and pseudo-capacitive property can be improved.[305-307] Jaidev et al.[308] reported the preparation of a novel binary hybrid nanocomposite based on polyaniline (PANI) and α-MnO_2 nanotubes by in situ polymerization. The polymerization is carried out in acidic medium using α-MnO_2 nanotubes as oxidant. The obtained MnO_2-PANI nanocomposite shows maximum specific capacitance of 626 F g^{-1} and corresponding energy density of 17.8 Wh kg^{-1} at a current density of 2 A g^{-1} in the potential range of 0-0.7 V. Guo and coworkers proposed a facile and scalable one-step strategy for patterning ultrathin MnO_2 nanorods (3 nm in diameter) on surfaces of PANI nanofibers by using polymer nanofibers and $KMnO_4$ as raw materials (Fig. 15).[309] The loading amount and patterning of MnO_2 nanorods on surfaces of PANI nanofibers can be controlled by simply altering the $KMnO_4$ concentration. In comparison with PANI nanofibers, the specific capacitance of MnO_2-PANI

composites has substantially increased by almost four-fold, with values as high as 417 F g^{-1} achieved. Using the same method, Jiang et al.[310] demonstrated the facile loading of ultrafine and loosened K-birnessite MnO_2 floccules on the surface of polyaniline (PANI) nanofibers by simply soaking the polyaniline nanofibers in a $KMnO_4$ aqueous solution. The as-prepared PANI–MnO_2 coaxial nanofibers with optimal composition, when applied as an electrode, exhibited a high specific capacitance (383 F g^{-1} at 0.5 A g^{-1}) with good rate and cycling stability. Such intriguing electrochemical performance is mainly attributed to the synergistic effects of the combined pseudo-capacitive contributions from the PANI core and MnO_2 shell.

4.2.2 MnO_2-Poly(3,4-ethylenedioxythiophene) (PEDOT) composite

Due to the excellent conductivity, high stability, good capacitive behavior and mechanical flexibility of PEDOT, MnO_2-PEDOT composite has received extensive attention in SCs. Lee and coworkers demonstrated the synthesis of a coaxial manganese oxide/poly(3,4-ethylene-dioxythiophene) (MnO_2/PEDOT) nanowire composite by performing electrodeposition of MnO_2 and PEDOT on Au-sputtered nanoelectrodes with different shapes (ring and flat-top, respectively) within the 200 nm diameter pores of an anodized aluminum oxide (AAO) template.[311] The as-prepared MnO_2/PEDOT coaxial nanowires showed the highest specific capacitance of 270 F g^{-1} when synthesized at the potential of 0.70 V vs Ag/AgCl. Rios et al. prepared the composite electrodes of poly(3,4-ethylenedioxithiophene) and manganese oxide (PEDOT/MnO_2) by electrodeposition of manganese oxide over PEDOT-modified titanium substrate. Tang et al.[312] developed a class of novel composite electrodes based on poly(3,4-ethylenedioxythiophene) (PEDOT) and manganese dioxide (MnO_2) by step-by-step anodic deposition on nickel foam. The optimized PEDOT/MnO_2/PEDOT sandwich electrode shows excellent capacitive behavior, and MnO_2 species in the optimized sandwich electrode possesses a high specific capacitance of 487.5 F g^{-1} at 1 A g^{-1}. Zhang and coworkers presented a facile and scalable method to synthesize a core–shell–branch hierarchical MnO_2@PEDOT@MnO_2 composite by using a simple electrochemical deposition strategy.[313] The maximum specific capacitance of 449 F g^{-1} is achieved through galvanostatic charge/discharge test at a current density of 0.5 A g^{-1}.

4.2.3 MnO_2-Polypyrrole (PPy) composite

Polypyrrole (PPy) is also a commonly used conducting polymer for constructing MnO_2-PPy composite due to its large specific surface area, high conductivity, and good stability.[314, 315] Zhang et al.[316] reported the preparation of MnO_2-PPy composites through chemical oxidation of pyrrole monomer and MnO_2 suspension with ammonium peroxysulfate at low temperature. The electrochemical results indicated that MnO_2-PPy composite electrode exhibited a specific capacitance of 352.8 F g^{-1} at a current density of 8 mA cm^{-2}. Bahloul et al.[89] synthesized a polypyrrole-covered MnO_2 composite by electrochemical polymerization of pyrrole deposited onto γ-MnO_2 particles. The asymmetric supercapacitor using MnO_2-PPy composite material showed a higher specific capacitance of 141.6 F g^{-1} compared with 73.7 F g^{-1} for γ-MnO_2 before PPy coating. The electrochemical performance improvement is not only due to the electronic conductivity of the polymer, but also due to the the increase of the specific surface area of the composite. Liu and coworkers developed a MnO_2 nanosheet-PPy composite film through the direct reaction of a carbon cloth with potassium permanganate ($KMnO_4$) and the subsequent chemical polymerization.[90] The electrochemical results revealed that the PPy with the high electrical conductivity had promoted the charge transfer in the MnO_2 nanofilm and thus enhanced the electrode performance (45.6 mF cm^{-2}). An areal capacitance of 25.9 mF cm^{-2} and an excellent rate performance (~50.1% of the initial capacitance when the scan rate increases 100 times from 2.5 to 250 mV s^{-1}) can be achieved for an aqueous symmetric supercapacitor that was assembled from the MnO_2-PPy nanofilm.

Conducting polymers have been widely investigated as the electrode materials by researchers because of the good electrical conductivity, low cost, mechanical stability and flexibility. They are normally used to form core-shell hybrid structures, where conductive polymer acts either as intermediate or outer shell. Besides enhancing the electrical conductivity of the electrodes and providing pseudo-capacitance, the intermediate conductive polymer shell could also act as sacrificing material for conformal in-situ deposition of MnO_2, while the conductive polymer could protect the MnO_2 active phase from dissolution in acidic electrolyte (H_2SO_4). Furthermore, MnO_2-polymer-carbon composites have also been intensively explored as the flexible electrodes with high electrochemical performance. However, the fundamental synergic effects are yet to be clarified and not all the attempts in combining conducting polymer and MnO_2 yielded positive

results.

4.3 MnO$_2$-condutive metal composite for SCs

Another effective way to improve electrical conductivity and to boost electrochemical performance is to conformally deposit MnO$_2$ nanostructures onto highly conductive and well-ordered metal micro-/nanostructures, which can serve as the mechanical support with greatly enhanced electron and ionic transport.

4.3.1 MnO$_2$-noble metal (Au, Ag) composite

Since the electrical conductivity of nanoporous metals (Au or Ag) is ~3 to 5 orders of magnitude higher than that of carbon materials, nanoporous metals are expected to dramatically enhance the electronic and ionic conductivity of MnO$_2$ for high specific capacitance in non-aqueous electrolytes.[136, 317] Lang et al.[318] fabricated 100-nm-thick nanoporous Au/MnO$_2$ composite films in a two-step procedure, which involved de-alloying Ag$_{65}$Au$_{35}$ (at%) using HNO$_3$ to produce conductive nanoporous gold and then plating nanocrystalline MnO$_2$ into the nanopores (Fig. 16). The nanoporous gold allows electron transport through the MnO$_2$, and facilitates fast ion diffusion between the MnO$_2$ and the electrolytes while also acting as a double-layer capacitor. The hybrid structures made of nanoporous gold and nanocrystalline MnO$_2$ have enhanced conductivity, resulting in a specific capacitance of the constituent MnO$_2$ (~1145 F g^{-1}) that is close to the theoretical value. Yan et al.[319] described the fabrication of arrays of nanowires on glass in which a gold core nanowire is encapsulated within a hemi-cylindrical shell of manganese dioxide. They first prepared the Au nanowires arrays on glass using the lithographically patterned nanowire electrodeposition (LPNE) method. Au nanowires were then used to deposit MnO$_2$ by potentiostatic electrooxidation from Mn^{2+} solution, forming a conformal, hemicylindrical shell with a controllable diameter ranging from 50 to 300 nm surrounding each Au nanowire. These hybrid nanostructures showed both an ultrahigh specific capacity of 1020 ± 100 F g^{-1} at 5 mV s^{-1} and 450 ± 70 F g^{-1} at 100 mV s^{-1} coupled with absolute cycle stability of this capacity to 1000 cycles.

Recently, Fan and coworkers reported a freestanding MnO$_2$/Au/MnO$_2$ nanospike electrodes based on 3D gold nanospike (NSP) films (Fig. 17a-c).[320] The large surface area of NSPs is utilized

31

to achieve respectable pseudocapacitance together with a thin layer of MnO_2 coating. The all-solid-state symmetric SCs based on $MnO_2/Au/MnO_2$ NSP (MAMNSP) electrodes showed that the devices have a volumetric capacitance of 20.35 F cm^{-3} and the highest specific energy and specific power of 1.75×10^{-3} W h cm^{-3} and 13.46 W cm^{-3}, respectively. Qiu et al.[321] developed for the first time a novel Au@MnO_2 core–shell nanomesh structure on a flexible polymeric substrate through nanosphere lithography combined with electrodeposition processing (Fig. 17d-f). The direct growth of MnO_2 on a well-conformed Au nanomesh, which acts as a transparent flexible electrode with high transparency, not only introduces metal oxides successfully but realizes an efficient contact between the current collector and the active materials needed for a fast charge transport during charging and discharging processes. As a result, a high areal capacitance of 4.72 mF cm^{-2} and an ultrahigh rate capability have been achieved on such hybrid films. Li et al.[322] synthesized one-dimensional (1D) tubular Ag/MnOx nanocomposites by the solvothermal method via the Kirkendall effect between potassium permanganate ($KMnO_4$) and Ag nanowire templates. The morphology and electrochemical performance of Ag/MnOx composites were tuned by varying the pH levels. When tested as an electrode for SCs, the hierarchical tubular Ag/MnOx nanosheet composites prepared in an acidic environment exhibited an optimized electrochemical performance, with specific capacitance of 180 F g^{-1} at current density of 0.1 A g^{-1}, and still maintained 80% of initial capacity after 1000 cycles. The proposed synthetic mechanism and the developed synthetic strategy in this work may provide design guidelines for synthesizing other hierarchical transition metal/transition metal oxide nanocomposites for supercapacitor.

4.3.2 MnO_2-transition metal (porous Cu and Ni, stainless steel, Mn film) composite

The transition metals (porous Cu and Ni, stainless steel, Mn film)[250, 323-326] are also good scaffolds to form MnO_2-based hybrid films or composites by conformal coating or penetration for SCs. Pang and coworkers prepared a novel Cu–MnO_2 composite through facile coating of a thin MnO_2 nanofilm onto the highly electronically conductive Cu superstructures.[325] The Cu superstructures were synthesized by using natural sapless leaves. Benefiting from the unique structures, the composite superstructures have a high specific capacity of 1024 F g^{-1} at 1.5 A g^{-1} and good capacity retention of around 96% after 2000 electrochemical cycles. Xiao et al.[88] reported a MnO_2/3D dendrites-like Ni core-shell electrode for high-performance SCs. The

MnO_2/3D-Ni electrode exhibits a large areal capacitance (837.6 mF cm^{-2}), excellent rate capability and high cycling stability (16% degradation after 2000 cycles). The high electrochemical properties of MnO_2/3D-Ni electrode can be attributed to the high conductivity of the Ni metal core, high porous and large specific surface structure of the MnO_2/3D-Ni nanocomposites, which facilitates electrolyte diffusion, electron transport, and material utilization. Wu and coworkers proposed a novel architecture, MnO_2 nanowires grown on ordered macroporous conductive Ni scaffold, to enhance the capacitive behavior of MnO_2 electrode.[241] This MnO_2-macroporous Ni composite expedites the electron conduction and electrolyte transport through film electrode and consequently improves the pseudocapacitive property of MnO_2 nanowires. Su et al.[327] fabricated ultrathin and flexible supercapacitor electrodes containing a manganese dioxide (MnO_2) nanostructure deposited onto 3D nickel nanocone arrays (NCAs) (Fig. 18). The MnO_2-NCAs electrode was prepared by an electrodeposition technology, which involves the cathode deposition of NCAs on a titanium carrier film as the current collector and subsequent anode deposited from the MnO_2 nanostructures as the active material. The resulting freestanding electrode exhibited outstanding mechanical robustness, high specific capacitance (632 F g^{-1}), enhanced energy density (52.2 Wh kg^{-1}) and excellent cycle performance (95.3% retention after 20000 cycles).

Dubal et al.[328] provided a simple and efficient route for the selective growth of branched MnO_2 nanorods on flexible stainless-steel substrates at ambient temperature without sacrificial templates or surfactants. The branched α-MnO_2 materials possess a loose mesoporous cluster and show enhanced rate performance and cyclability. Excellent supercapacitive properties coupled with low production costs and the environmentally friendly nature of MnO_2 make this material promising for a wide range of applications. Deng et al.[329] presented a nanoarchitecture consisting of a three-dimensionally ordered macroporous Mn core–MnO_2 shell inverse-opal structure using electrodeposition of metallic Mn within a polystyrene (PS) bead template in an ionic liquid (IL), subsequently anodized in KCl aqueous solution (3 M) with varied anodization courses to construct a nano-architectured pseudocapacitive electrode (Fig. 19). The varied anodization courses were confirmed to cause variations of the material characteristics of the prepared 3D macroporous Mn core/MnO_2 electrodes and thereby in their pseudocapacitive performance. These unique electrodes

anodized with the cyclic voltammetric method showed the most promising specific capacitance, 1200 ± 60 F g^{-1} (based on the mass of Mn/MnO$_2$), with a satisfactory rate capability and cycling performance.

As discussed above, the current strategies for the design of MnO$_2$-transition metal composite electrode architectures are mainly focused on loading MnO$_2$ on these scaffolds, which act both as high surface area mechanical support and current collector for MnO$_2$ phase and are the main physical link between the electrode and the external structures of the supercapacitor. However, there are some key issues of these composite electrodes. (i) the first one is the chemical stability in aqueous electrolytes, because porous Cu and Ni are not stable in acidic electrolyte which would cause corrosion of the metal scaffolds, thus leading to the degradation of the conductivity of the composite electrode. The way to avoid this problem is the combination of conducting polymers to prepare metal-polymer-MnO$_2$ ternary composite in which the metal scaffolds are protected by the polymers to achieve a high conductivity and flexible supercapacitor. (ii) the potential window may be decreased due to the low electrochemical stability of the porous metal during the charge/discharge process, which could be accommodated by using organic electrolyte. (iii) the last one is the size of the porous metals. Small size of the porous metal would possibly lead to the collapse of the electrode after sufficient active material loading, whereas with a large size, the porous metal itself would inevitably occupy too much volume, ultimately lowering the the volumetric energy density of the composite electrode. Therefore, optimizing the size of the porous metal in the composite represents a significant challenge.

4.3.3 MnO$_2$-nickel foam (Ni) composite for binder-free electrode

Highly conductive 3D porous materials as electrode that enable enhanced penetration of an electrolyte appropriate cations that enable compensation of the Mn^{3+}/Mn^{4+} redox reaction during charge and discharge cycles are crucial to improve the capacity performance of MnO$_2$ films. Nickel foam with a large electronic conductivity and a 3D porous structure is a promising candidate for a capacitive electrode substrate material, and thus has been extensively studied for emerging binder-free electrode in the past several years.[330-333] Liu and coworkers prepared well-defined mesoporous MnO$_2$ nanosheet arrays on Ni foam current collectors using one-step electrodeposition, followed by a low-temperature thermal annealing process.[334] The MnO$_2$

nanosheet arrays grown on Ni foam were used as binder-free electrodes, which exhibited a

specific capacitance as high as 201 F g^{-1} at a current density of 1 A g^{-1}. Huang et al.[335] developed

a facile one-pot hydrothermal method for the large scale synthesis of MnO_2 nanosheets arrays

grown on Ni foam (Fig. 20). In this work, the deposition of MnO_2 nanosheets did not need any

surfactant or the electrochemical deposition due to the fact that MnO_2 can be produced via

self-decomposition of $KMnO_4$ during hydrothermal reaction. Benefiting from favorable

mesoporous structure as well as the rational design of a binder-free electrode, the MnO_2 nanosheet

arrays on Ni foam electrode exhibits a relatively high capacitance (595.2 F g^{-1} at a current density

of 0.5 A g^{-1}) and excellent cycling ability (89% retention after 3000 cycles). Pang et al.[213] reported

the synthesis of δ-MnO_2 nanosheets grown on nickel foam by using a one-pot chelation-mediated

aqueous method at a low temperature. The as-prepared 3D hierarchical δ-MnO_2 nanosheet on Ni

foam can be directly used as additive-free and binder-free electrode for SCs, which exhibited

excellent favorable electrochemical performance, such as high specific capacitance (325 F g^{-1} at a

current density of 1 A g^{-1}), good long-term cycle stability and low equivalent series resistance and

charge transfer resistance.

The porous metal scaffold is a good supporting material to form MnO_2-based hybrid

films/arrays by conformal coating. Different types of metal scaffolds, such as noble Au, Ag,

porous Cu, Ni and Mn have been introduced in this chapter. According to the discussion on the

previous works, there are several aspects that determine the electrochemical properties of the

MnO_2-based composite electrodes. First of all, the porous metal can serve as the current collectors

which have much larger surface area than the bulky metal film current collectors. This enables the

high mass loading of MnO_2 materials, thus improving the energy density per unit area. Second,

these porous metal structures are capable of providing efficient pathways for both ion and electron

through the entire electrode, which can avoid the dead-volume of the whole electrode. More

importantly, the good mechanical robustness of these metal scaffolds can ensure the stability of the

composite electrodes during the repeated charge/discharge cycles. The challenge of the application

of the porous metal for preparing the MnO_2-conducting metal composite electrode is the high

production cost, which limits its practical applications.

4.4 MnO_2-metal oxide/hydroxide composite for SCs

Incorporation of certain metal oxide/hydroxide with MnO_2 to fabricate MnO_2-based composite is one of the effective ways to improve the electrochemical property. Through optimizing preparation parameters, generated synergistic effects may enlarge specific surface area, facilitate electrons and ions transport, add active sites or improve cycling stability. Up to now, various MnO_2-metal oxide/hydroxide composite with different geometrical attributes and morphological forms have been employed as electrodes for SCs.

4.4.1 MnO_2-Co_3O_4 composite

An alternative route to improve the performance of MnO_2 electrode is constructing a novel MnO_2-Co_3O_4 composite nanostructure, in which electrochemical activities of each component are fully manifested and the kinetics of ion/electron transport are guaranteed. Liu et al.[336] reported the preparation of Co_3O_4@MnO_2 core/shell nanowire composites on Ti foil by using 3D ordered amorphous carbon layers as a sacrificial reactive template to anchor MnO_2 nanostructures onto Co_3O_4 nanowire scaffolds, leading to a well-designed hybrid architecture. The as-prepared Co_3O_4@MnO_2 composite electrode exhibited a high capacitance (480 F g^{-1} at 2.67 A g^{-1}) with good cycle performance (2.7% capacitance loss after 5000 cycles) and remarkable rate capability. In the same way, Kong et al.[337] demonstrated the fabrication of the 3D hierarchical Co_3O_4@MnO_2 core-shell composite arrays for binder-free electrode used in supercapacitor. Huang et al.[338] proposed a two-step hydrothermal reaction to design and fabricate hierarchical Co_3O_4@MnO_2 compsite arrays on Ni foam, in which the mesoporous Co_3O_4 arrays served as the "core" and the ultrathin branch MnO_2 nanosheets were the "shell" layer (Fig. 21). The unique designed MnO_2-Co_3O_4 composite electrodes exhibited a high specific capacitance (560 F g^{-1} at a current density of 0.2 A g^{-1}), good rate capability, and excellent cycling stability (95% capacitance retention after 5000 cycles). Lin and coworkers prepared nano-Co_3O_4/MnO_2 composites by anodic composite deposition from $Mn(NO_3)_2$ solutions containing different amounts of suspended Co_3O_4 particles.[339] The specific capacitance of the composite reached 317 F g^{-1} at a scan rate of 5 mV s^{-1}. Recently, Wang et al. fabricated the Co_3O_4 nanowires@MnO_2 nanoflakes core–shell composite supported on carbon fiber paper and further investigated the performance as the electrodes for SCs. The composite electrode possessed a high specific capacitance as high as 1200

F g^{-1} (based on low loading of MnO$_2$) at the current density of 1 A g^{-1} in 2 M KCl electrolyte.

4.4.2 MnO$_2$-NiO/Ni(OH)$_2$ composite

The composites of MnO$_2$ and nickel oxides/hydroxides exhibited enhanced capacitance performance compared with their individual components.[340-342] Liu et al.[341] prepared nanostructured MnO$_2$-NiO composite by the sol–gel and chemical deposition method. They found that introducing a proper proportion of the NiO into MnO$_2$ to form an electroactive material is an effective method to achieve high performance electrochemical capacitor. Fan and coworkers reported the synthesis of MnO$_2$–NiO nanoflake-assembled tubular array on stainless steel substrate to function as pseudocapacitor electrode by programmed three-dimensional (3D) interfacial reactions, in which the ZnO nanowire array was employed as the low-cost sacrificial template.[343] With the smart combination of MnO$_2$ and NiO, a synergistic effect can be observed: the firstly-grown MnO$_2$ flake-assembled array provides a scaffold for the later NiO growth, avoiding the conventional aggregation and ensuring sufficient ion diffusion; while the further introduction of NiO reduces the charge-transfer resistance of MnO$_2$, leading to fast electron transport within active materials. Consequently, the areal specific capacitance of 0.35 F cm^{-2} can be achieved, four orders of magnitude higher than the areal specific capacitance values of carbonaceous materials (10–40 μF cm^{-2}). Jiang et al.[344] presented a novel hybrid structure of porous MnO$_2$–Ni(OH)$_2$ composite with a nanoflake surface by a green, surfactant-free and scalable strategy. The optimal MnO$_2$–Ni(OH)$_2$ composite exhibited a very high specific capacitance with excellent rate and cycling stability in 1 M Na$_2$SO$_4$ aqueous solution (355.5 F g^{-1}), and even in 1 M KOH aqueous solution (487.4 F g^{-1}). Chen et al.[345] developed a facile one-step hydrothermal co-deposition method for growth of ultrathin Ni(OH)$_2$-MnO$_2$ composite nanosheet arrays on three dimensional (3D) macro-porous nickel foam (Fig. 22). Due to the highly hydrophilic and ultrathin nature of hybrid nanosheets, as well as the synergetic effects of Ni(OH)$_2$ and MnO$_2$, the fabricated Ni(OH)$_2$-MnO$_2$ composite exhibited an ultrahigh specific capacitance of 2628 F g^{-1}.

4.4.3 MnO$_2$-TiO$_2$ composite

TiO$_2$ is abundant, low cost and environmentally benign with a stable chemical nature, so it has been widely studied in many domains, especially in electrochemical devices. Furthermore, it

has higher electrical conductivity (10^{-5} to 10^{-2} S cm^{-1}) than MnO_2.[346, 347] Hence, introducing TiO_2 to construct MnO_2-TiO_2 composite will be an excellent strategy.[348-350] For example, hierarchical TiO_2 nanobelts@MnO_2 ultrathin nanoflakes core–shell composite arrays were fabricated on a Ti foil substrate by hydrothermal approach and further investigated as the electrode for a supercapacitor.[351] The composite electrode exhibited a specific capacitance as high as 557.6 F g^{-1} at a scan rate of 200 mV s^{-1} (454.2 F g^{-1} at a current density of 0.2 A g^{-1}) in 1 M Na_2SO_4 aqueous solution. In particular, hydrogenation can greatly improve the electrical conductivity of TiO_2.[347] Lu et al.[352] reported the use of hydrogen-treated TiO_2 (H-TiO_2) NWs as the core (conducting scaffold) to support electrochemically active MnO_2 to form H-TiO_2@MnO_2 composite NWs (Fig. 23). The H-TiO_2@MnO_2 yielded a high specific capacitance of 449.6 F g^{-1} at the scan rate of 10 mV s^{-1}. Significantly, the CV curves collected for the ASC device under flat, bent, and twisted conditions were similar (Fig. 23d), indicating their excellent mechanical stability as flexible energy storage devices. Moreover, the maximum volumetric energy and volumetric power density of the flexible ASC device were calculated to be 0.30 mWh cm^{-3} (59 Wh kg^{-1}) and 0.23 W cm^{-3} (45 kW kg^{-1}), which were substantially higher than values reported for other solid-state SCs (Fig. 23e). Recently, Zhang and coworkers synthesized an ultrathin layer (about 5 nm) of MnO_2 coated on the H-TiO_2 nanowires (NWs) grown on flexible carbon microfibers (labeled as MnO_2/H-TiO_2/CMF NWs), and then quantitatively studied the effect of the hydrogenated temperature varying from 400 °C to 800 °C on the electrochemical performance of MnO_2/H-TiO_2/CMF NW composite electrodes.[353] Typically, for a MnO_2-TiO_2 composite electrode hydrogenated at 600 °C, the specific capacitance reached 630.1 F g^{-1} at 10 mV s^{-1} and the high energy density of 46.0 Wh kg^{-1} was obtained at the high power density of 21.8 kW kg^{-1}.

4.4.4 MnO_2-ZnO composite

ZnO, as one of the most attractive functional semiconductor materials, is widely used for the efficient mechanical support and electron conducting pathway to develop ZnO@MnO_2 core-shell composite structure because of its high chemical stability in the neutral and alkaline electrolyte, conductivity, and mechanical flexibility.[354-357] He et al.[358] developed a simple and quick approach to synthesize a novel single-crystal ZnO nanorod/amorphous MnO_2 shell composites for supercapacitor applications. The single-crystal ZnO nanorods as cores experienced less structural

stress or damage during electrochemical cycling, and they served as mechanical supports and effective electron transport pathways and increased the electrochemical utilization of MnO_2. Yang et al.[359] designed a novel hierarchical structure of MnO_2/ZnO composite on cabon-fibric by a simple three-step-solution method. The design comprised ZnO nanowires radially grown on each micron-size fiber of a carbon-fabric electrode, with a thin MnO_2 shell on each ZnO nano-core (Fig. 24). The as-prepared MnO_2/ZnO composite electrode exhibited a high specific capacitance of 886 F g^{-1}, a specific energy of 16 Wh kg^{-1}, a specific power of 27 kW kg^{-1}, and good long-term cycling stability. Recently, a hierarchical ZnO@MnO_2 composite pillar arrays on Ni foam have been fabricated by a facile two-step hydrothermal approach.[360] The core-shell hybrid nanostructure was achieved by decorating ultrathin self-standing MnO_2 nanosheets on ZnO pillar arrays grown radically on Ni foam. This unique well-designed binder-free electrode exhibited a high specific capacitance (423.5 F g^{-1} at a current density of 0.5 A g^{-1}), and excellent cycling stability (92% capacitance retention after 3000 cycles). The facile design of the unique composite architectures provides a new and effective approach to fabricate high-performance binder-free electrode for SCs.

4.4.5 MnO_2-other transition metal oxides (SnO_2, CuO, Fe_2O_3, Fe_3O_4) composite

Combining MnO_2 with many other transition oxides (SnO_2, CuO, MnO_2, Fe_2O_3, Fe_3O_4)[215, 361-366] are also developed by designing novel composite pseudo-capacitive systems. For example, Kim and coworkers synthesized the size- and thickness-tunable two-dimensional (2D) MnO_2 nanosheets on SnO_2 backbone arrays by one-step enhanced chemical bath deposition (ECBD) method at a low temperature (~50 °C).[215] The SnO_2-MnO_2 composite electrode achieved a specific capacitance of 162 F g^{-1} at an extremely high current density of 20 A g^{-1}, and good cycling stability of 92% capacitance retention, along with a coulombic efficiency of almost 100% after 5000 cycles. Huang et al.[362] developed a simple and cost-effective method to fabricate hierarchical CuO@MnO_2 core-shell heterostructures as electrode materials for high-performance SCs (Fig. 25). They systematically probed structures at different reaction time and therefore proposed a possible growth mechanism for the CuO@MnO_2 composite structure (Fig. 25a), which could be divided into three stages. Firstly, the MnO_4^- nuclei were produced and adsorbed on surfaces of Cu nanowires, forming MnO_2 nuclei. With the increase of reaction time, the MnO_2 nuclei were

aggregated and transformed to nanosheets. In the meanwhile, Cu nanowires were oxidized to CuO nanowires, followed by a transformation to CuO nanotubes. Finally, the MnO_2 nanosheets were compact and totally covered surfaces of CuO nanotubes, resulting in the formation of the hierarchical CuO nanotube@MnO_2 nanosheets nanocomposites. The complex heterostructures were found to show a high specific capacitance of 276 F g^{-1} at a current density of 0.6 A g^{-1}, much improved rate performance, and long-term cycling stability (92.1% of its original value after 1000 cycles). An asymmetric supercapacitor with CuO@MnO_2 core-shell nanocomposite as the positive electrode and activated microwave exfoliated graphite oxide (MEGO) as the negative electrode yielded an energy density of 22.1 Wh kg^{-1} and a maximum power density of 85.6 kW kg^{-1}, rendering such heterostructures promising for the application as high-performance SCs.

Zhu et al.[365] reported the synthesis of hierarchically porous MnO_2 microspheres doped with Fe_3O_4 nanoparticles by a one-step ultrasound assisted method. The scalable synthesis is based on Fe^{2+} and ultrasound assisted nucleation and growth at a constant temperature in a range of 25−70 °C. A systematic optimization of reaction parameters results in isolated, porous, and uniform MnO_2-Fe_3O_4 composite spheres. The uniform MnO_2-Fe_3O_4 composite spheres exhibited a superior specific capacitance of 448 F g^{-1} at a scan rate of 5 mV s^{-1}, which is nearly 1.5 times that of the extremely high reported value for pure MnO_2. An isomorphous MnO_2@MnO_2 core-shell nanostructure had also been developed for the first time by using MnO_2 nanowires as seed crystals.[363] These unique nanoarchitectures consisting of an isomorphous layer of β-MnO_2 nanosheets well grown on the surface of β-MnO_2 nanowires exhibit remarkable electrochemical performance with high capacitance and ultra long cycle life, i.e., nearly 92.2% retention after 20000 cycles at a current density of 5 A g^{-1}. Furthermore, Huang et al.[367] reported a facile and cost-effective approach to fabricate Co_3O_4/SnO_2@MnO_2 core–shell nanocomposite, in which the mesoporous Co_3O_4/SnO_2 nanoboxes acted as the "core" and the ultrathin MnO_2 nanosheets worked as the "shell" layer (Fig. 26). This unique core–shell nanostructure was anticipated to manifest excellent capacitive performance because of the superior structural advantages. On the one hand, the Co_3O_4/SnO_2 nanoboxes could serve as the hard template, providing a large surface area for the growth of MnO_2 nanosheets and avoiding the aggregation of active materials that degrades the cycle stability. On the other hand, the porous MnO_2 nanosheets possessed large specific surface

area and multiple oxide sites, which would facilitate ion diffusion and provide high-energy storage capacity. The resultant $Co_3O_4/SnO_2@MnO_2$ core–shell nanostructures exhibited a high specific capacitance of 225 F g^{-1} at a current density of 0.5 A g^{-1} and excellent cycling stability (90.7% retention after 6000 cycles), suggesting that such core–shell architectures could be expected to be promising candidates for supercapacitor applications.

4.4.6 MnO_2-binary metal oxide composite

Binary metal oxides (BTMOs) contain at least one transition metal ion and one or more electrochemically active/inactive ions. BTMOs can utilize the synergistic effect of pure oxides, which can improve the capacitive property with a widened potential window, superior conductivity, more active sites and improved stability.[165] Therefore, many studies of combining MnO_2 with BTMOs ($NiCo_2O_4$, $CuCo_2O_4$, $ZnCo_2O_4$, $NiMoO_4$, and Zn_2SnO_4)[368-378] for SCs have been conducted and a series of good results were achieved. For instance, Yu et al.[368] fabricated hierarchical $NiCo_2O_4@MnO_2$ core–shell heterostructured nanowire (NW) arrays on Ni foam as a binder-free electrode, which exhibited a large areal specific capacitance of 3.31 F cm^{-2}, desirable rate performance and cycling stability in a 1 M LiOH solution. Xu et al.[369] demonstrated the design and fabrication of hierarchical mesoporous $NiCo_2O_4@MnO_2$ core–shell nanowire arrays on nickel foam via a facile hydrothermal and electrodeposition process for supercapacitor applications (Fig. 27 a and b). The $NiCo_2O_4@MnO_2$ core-shell nanowires possessed a high areal capacitance up to 2.244 F cm^{-2}, while the $NiCo_2O_4$ nanowires only showed an areal capacitance of 1.428 F cm^{-2}. Zou et al.[372] used a one-step hydrothermal reaction followed by a post-annealing treatment, we synthesized networked $NiCo_2O_4/MnO_2$ branched nanowire heterostructure arrays on Ni foam substrates (Fig. 27 c and d). The as-prepared $NiCo_2O_4/MnO_2$ electrode showed a specific capacitance of 2827 F g^{-1} at a current density of 2 mA cm^{-2}, which was still maintained at 2339 F g^{-1} at 20 mA cm^{-2}. The electrode also presented excellent cycling stability with only 1.6% loss of specific capacity after 3000 cycles at a high charge/discharge current density. Recently, a hierarchical $NiCo_2O_4@MnO_2$ core–shell nanosheet arrays hybrid composite integrated electrode for SCs was designed and synthesized via a facile two-step hydrothermal method (Fig. 27 e and f).[373] Electrochemical characterizations indicated that the unique nano-architecture possesses excellent electrochemical properties, exhibiting a capacitance of 2.39 F cm^{-2} as well as high

cycling stability (7.4% loss after 2000 cycles).

To boost the electrochemical utilization and area-specific capacitance, core–shell $CuCo_2O_4$@MnO_2 nanocomposite arrays on carbon fabrics were synthesized and utilized as high-performance, binder-free, positive electrodes for electro-chemical capacitors.[374] The electrode takes advantage of the synergistic effects contributed from both the porous $CuCo_2O_4$ nanowire core and the MnO_2 shell layer. The as-prepared electrode had a high cell-specific capacitance of 327 F g^{-1} at a current density of 1.25 A g^{-1} with excellent rate capability (90% capacitance retention at a current density of 6.25 A g^{-1}) in aqueous electrolyte. $ZnCo_2O_4$/MnO_2 nanocone forests with a mesoporous, hierarchical core-shell structure and a large surface area were hydrothermally grown on 3D nickel foam (Fig. 28).[376] The supercapacitor electrodes prepared from the unique structure exhibits exceptional specific capacitances of 2339 and 1526 F g^{-1} at current densities of 1 and 10 A g^{-1}, respectively, and long-term capacity retention of 95.9% after 3000 cycles at 2 A g^{-1} and 94.5% after 8000 cycles at 10 A g^{-1}. Li and coworkers demonstrated the design and fabrication of a novel flexible nanoarchitecture by coating ultrathin MnO_2 films to highly electrical conductive Zn_2SnO_4 nanowires grown radially on carbon microfibers (CMFs).[377] The maximum specific capacitance of 642.4 F g^{-1} (based on pristine MnO_2) by chronopotentiometry at a current density of 1 A g^{-1} was achieved in 1 M Na_2SO_4 aqueous solution. Guo et al.[378] reported the synthesis of a hybrid structure of core/shell $NiMoO_4$@MnO_2 on carbon cloth by a two-step hydrothermal route for SCs. The $NiMoO_4$@MnO_2 electrode yielded high-capacitance performance with a high areal capacitance of 3.90 F cm^{-2} at a current density of 8 mA cm^{-2} and a desirable cycling ability (90.5% capacitance retention after 4000 cycles). The as-prepared $NiMoO_4$@MnO_2 composite electrode with remarkable electrochemical performance could be the promising pseudocapacitive electrode materials for high-performance SCs.

Fabrication of MnO_2-metal oxide/hydroxide composite electrode with high specific surface area and porous configuration has been intensively studied, and a series of good results has been achieved. In this section, hierarchical porous composites containing MnO_2 as the electrode material for supercapacitors have been reviewed briefly. As described above, many metal oxides or hydroxides (Co_3O_4, NiO, $Ni(OH)_2$, TiO_2, ZnO, etc.) have higher electrical conductivity than MnO_2, but with narrower operating potential window. Therefore, by combining these different

metal oxide/hydroxides with MnO_2, synergic properties are expected. Research has shown that the combination of two types of materials not only provides the composite electrode material with stronger redox ability, but also enhances the stability. Most importantly, the higher conductivity of the other metal oxide/hydroxides can serve as the backbone to support and provide effective electrical connection to MnO_2, which can produce a synergistic effect of all individual constituents. According to these reasons, tuning the microstructure, crystallinity, and conductivity of the MnO_2-based electrodes by constructing binary or ternary composites could be an efficient way to improve the performance of MnO_2-based supercapacitors.

5. MnO_2-based microsupercapacitors

Microsupercapacitor (MSC) is a new type of supercapacitor with typical device feature sizes in the range of micrometers. It is considered to be one of the promising power sources for driving miniaturized electronic devices such as sensors-actuators, energy-harvesting microsystems, microelectromechanical systems (MEMS) or on-chip electronics.[52] Compared to conventional SCs, MSCs have high energy density, power density and good charge/discharge rate due to the reduced diffusion length.[379] Moreover, MSCs can be directly coupled with other energy storage units (microbatteries and fuel cell), microsensors, and biomedical implants to offer sufficient peak power.[380] Therefore, a great deal of attention has been focused on MSCs, for which a series of nanostructured active materials have been developed.[381-388] Among them, MnO_2-based materials have been exploited as active materials for MSCs by taking advantage of the unique properties of environmental friendly, high theoretical capacitance, good stability within a reasonable potential range.[389] For instance, Cao and coworkers described a low-cost method of fabricating flexible and all-solid-state MSCs by microfluidic etching.[390] The micro-supercapacitor configuration is composed of sub-10-nm-scale MnO_2 nanoparticle interdigital microelectrode fingers prepared by microfluidic etching with H_3PO_4-PVA thin films as both the solid-state electrolyte and the flexible substrate. Shen et al.[391] demonstrated an asymmetric microsupercapacitor that combined the advantages of both MnO_2 positive electrode and carbon negative electrode for energy storage on a chip. A self-supporting composite containing MnO_2 and another nanoporous activated carbon (AC) were separated in an interdigital structure by using micro-electro-mechanical systems (MEMS)

fabrication technologies. Measurements of the prototype show that the asymmetric MSC had well-performed capacitive behavior, and its working voltage range was extended from 1 V to 1.5 V in aqueous electrolyte due to the MnO_2–AC configuration. Wang et al.[392] constructed a symmetric microsupercapacitor by electrochemically depositing manganese oxide onto micro-patterned current collectors. Benefiting from high surface-to-volume ratio of manganese oxide and short diffusion distance between electrodes, the synthesized microsupercapacitor showed an ultra-high areal capacitance of 56.3 mF cm^{-2} at a current density of 27.2 μA cm^{-2}.

Yang and coworkes developed a screen printing technology for fabricating all-solid flexible MSCs, which consisted of a printed Ag electrode, MnO_2/onion-like carbon (MnO_2/OLC) as active material and a polyvinyl alcohol:H_3PO_4 (PVA:H_3PO_4) as the solid electrolyte.[379] A capacity of 7.04 mF cm^{-2} was achieved for the screen printed MnO_2/OLC MSCs at a current density of 20 μA cm^{-2}. Kaner and coworkes demonstrated 3D high-performance hybrid MSCs based on graphene and MnO_2 by rationally designing the electrode microstructure and combining active materials with electrolytes that operate at high voltages (Fig. 29).[393] These microdevices enabled an ultrahigh capacitance per footprint approaching 400 mF cm^{-2} with a high energy density of up to 22 Wh L^{-1}. These developments are promising for micro-electronic devices such as biomedical sensors and radiofrequency identification tags where high capacity per foot print is crucial. Recently, a reduced graphene oxide (RGO)/manganese dioxide (MnO_2)/silver nanowire (AgNW) ternary hybrid film (RGMA ternary hybrid film) was successfully fabricated by a facile vacuum filtration and subsequent thermal reduction. The hybrid film was used directly as a binder-free electrode for MSCs (Fig. 30).[394] In this work, a flexible, transparent, all-solid state RMGA-MSC was also built, and its electrochemical performance in an ionic liquid gel electrolyte were investigated in depth. Notably, the RGMA-MSCs displayed superior electrochemical properties, including exceptionally high rate capability (up to 50000 mV s^{-1}), high frequency response (very short corresponding time constant $\tau_0 = 0.14$ ms), and excellent cycle stability (90.3% of the initial capacitance after 6000 cycles in ionic liquid gel electrolyte). Dubal et al.[395] reported a novel architecture design of hierarchical MnO_2@silicon nanowires (MnO_2@SiNWs) hetero-structures directly supported on silicon wafer for MSCs. The as-prepared 3D mesoporous MnO_2@SiNWs in Li-ion doped ionic liquids electrolyte could be cycled reversibly across a voltage of 2.2 V and exhibited a high areal

capacitance of 13 mF cm^{-2}. They found that the high conductivity of the Si NWs arrays together with the large surface area of ultrathin MnO_2 nanoflakes were responsible for the good performance of the microsupercapacitor device. The design concept in this work opens up a novel avenue to fabricate electrode materials for high-performance MCSs.

6. Summary and perspectives

MnO_2-based SCs have experienced rapid development in recent years and have demonstrated immense potential as highly efficient energy storage device. In this review, we have summarized the latest progresses in this field, highlighted the important factors affecting the performance of MnO_2-based electrode and the challenges as well as future perspectives in designing MnO_2-based composite as advanced electrodes.

Despite some significant progresses made in MnO_2-based SCs, there are still practical challenges and obstacles to overcome to satisfy the requirements of future power sources (such as high energy and power densities, long lifetime, low cost, good safety, and environmental benignity, etc.). Several important issues have to be considered in the development of next generation MnO_2-based electrodes. The first challenge is the low energy density of the MnO_2-based electrodes, especially on the whole electrode basis, which cannot meet the demand for practical application. Thus, future research should be directed towards the development of high energy density supercapacitor device by widening the device operating voltage and increasing the loading of MnO_2. Asymmetric configurations and the use of ionic liquids with an electrochemically stable window of 4 V is one way to widen the operating voltage. For example, by designing MnO_2//activated graphene asymmetric capacitor and using ionic liquid as electrolyte, the potential window can be maximized to 3.6 V. A higher cell voltage improves both energy and power densities, as they are proportional to the voltage window (V^2). The other challenge, especially for large-scale energy storage applications, is the high cost of the production. There are two strategies to solve this problem: (1) incorporating earth-abundant carbon materials with MnO_2; (2) one-step synthesis or highly scalable approaches to produce MnO_2-based electrodes, such as facile solution-based method and printing technique, will be of great importance for designing scalable and low-cost devices.

Besides the research in electrode materials, it is also necessary to investigate the fundamental

science. For instance, we need to study the chemical and physical interactions of the MnO_2-based composite materials since the interactions can strongly affect the morphology, size and crystalline structure of the composite, thus affecting the electrochemical properties. In particular, it is important to understand the electrochemical mechanisms of MnO_2-based composites and to investigate the characteristics of the two levels of interface, namely the interface between electrolyte and composite electrodes and the interface within the composite between MnO_2 and another component. Furthermore, the development of flexible SCs has attracted great attention due to their high power density along with the unique properties of being flexible, lightweight, shape versatile, and eco-friendly. However, the deployment of the flexible SCs based on MnO_2-based electrodes is still at early stage and the state-of-the-art electrodes show limited energy densities. Therefore, the fabrication of flexible devices based on MnO_2-based nanostructures is highly desirable.

Based on the challenges discussed above, several possible future trends for the MnO_2-based high-performance SCs are listed below:

(1)   Improve the overall electricity of the MnO_2-based electrodes to the largest extent by utilizing various conducting agents, for example, designing hierarchical architectures of MnO_2@carbon/conducting polymer or MnO_2@carbon/porous metal. The desired composite structures are assembled by numerous tiny units composed of MnO_2 core and carbon/polymer or carbon/metal shell. This design can accommodate the electrolyte throughout the electrode and thus produce a large surface area for ion transfer between electrolyte and the active material, thus achieving ultra-fast energy storage.

(2)   For the MnO_2-based film electrode, it is promising to integrate synergetic nanomaterials into the remaining free space. The main aim is to further increase the specific energy density of the electrodes by minimizing the dead volume within the electrode. We should also consider that sufficient space still needs to be maintained for electrolyte penetration.

(3)   Designing lightweight and mechanically flexible electrode for future applications. We should pay close attention to the MnO_2-based hybrid electrodes that combine the

advantages of both pseudo-capacitance MnO_2 materials with the use of cost-effective flexible substrates.

(4)   Highly scalable, facile, solution-based methods and printing techniques will be a good solution for making large-scale and low cost MnO_2-based high-performance microsupercapacitor devices.

In conclusion, supercapacitor devices will play an important role in energy storage and harvesting, which is expected to complement with batteries in certain applications to reduce the environmental pollution problems and minimize the use of hydrocarbon fuels. With recent achievements in MnO_2-based electrodes, high performance SCs with safe operation and environmental-friendly character that are suitable for practical energy storage and power supply may be commercialized in the near future.

Acknowledgements

References

1.   P. Simon and Y. Gogotsi, *Nat. Mater.*, 2008, **7**, 845-854.
2.   J. P. Holdren, *Science*, 2007, **315**, 737-737.
3.   D. Ginley, M. A. Green and R. Collins, *MRS Bulletin*, 2008, **33**, 355-364.
4.   V. S. Arunachalam and E. L. Fleischer, *MRS Bulletin*, 2008, **33**, 264-276.
5.   H. Wang and H. Dai, *Chem. Soc. Rev.*, 2013, **42**, 3088-3113.
6.   G. Yu, X. Xie, L. Pan, Z. Bao and Y. Cui, *Nano Energy*, 2013, **2**, 213-234.
7.   A. S. Arico, P. Bruce, B. Scrosati, J. M. Tarascon and W. Van Schalkwijk, *Nat. Mater.*, 2005, **4**, 366-377.
8.   B. Dunn, H. Kamath and J.-M. Tarascon, *Science*, 2011, **334**, 928-935.
9.   A. Manthiram, A. V. Murugan, A. Sarkar and T. Muraliganth, *Energy Environ. Sci.*, 2008, **1**, 621-638.
10.   L. L. Zhang, R. Zhou and X. S. Zhao, *J. Mater. Chem.*, 2010, **20**, 5983-5992.

11.   J. R. Miller and P. Simon, *Science*, 2008, **321**, 651-652.

12.   F. Shi, L. Li, X.-l. Wang, C.-d. Gu and J.-p. Tu, *RSC Adv.*, 2014, **4**, 41910-41921.

13.   P. J. Hall, M. Mirzaeian, S. I. Fletcher, F. B. Sillars, A. J. R. Rennie, G. O. Shitta-Bey, G. Wilson, A. Cruden and R. Carter, *Energy Environ. Sci.*, 2010, **3**, 1238-1251.

14.   R. Kotz and M. Carlen, *Electrochim. Acta*, 2000, **45**, 2483-2498.

15.   S. Liu, S. Sun and X.-Z. You, *Nanoscale*, 2014, **6**, 2037-2045.

16.   L. L. Zhang and X. S. Zhao, *Chem. Soc. Rev.*, 2009, **38**, 2520-2531.

17.   M. J. Young, A. M. Holder, S. M. George and C. B. Musgrave, *Chem. Mater.*, 2015, **27**, 1172-1180.

18.   J. W. Long, D. Bélanger, T. Brousse, W. Sugimoto, M. B. Sassin and O. Crosnier, *MRS Bulletin*, 2011, **36**, 513-522.

19.   G. Wang, L. Zhang and J. Zhang, *Chem. Soc. Rev.*, 2012, **41**, 797-828.

20.   S. Park, J. An, J. W. Suk and R. S. Ruoff, *Small*, 2010, **6**, 210-212.

21.   C. Cougnon, E. Lebegue and G. Pognon, *J. Power Sources*, 2015, **274**, 551-559.

22.   L. Timperman, A. Vigeant and M. Anouti, *Electrochim. Acta*, 2015, **155**, 164-173.

23.   L. Yang, Z. Shi and W. Yang, *Electrochim. Acta*, 2015, **153**, 76-82.

24.   Y. S. Yun, M. H. Park, S. J. Hong, M. E. Lee, Y. W. Park and H.-J. Jin, *ACS Appl. Mater. Interfaces*, 2015, **7**, 3684-3690.

25.   L. Zhao, L. Z. Fan, M. Q. Zhou, H. Guan, S. Qiao, M. Antonietti and M. M. Titirici, *Adv. Mater.*, 2010, **22**, 5202-5206.

26.   Y.-M. Chang, C.-Y. Wu and P.-W. Wu, *J. Power Sources*, 2013, **223**, 147-154.

27.   X. Lu, J. Shen, H. Ma, B. Yan, Z. Li, M. Shi and M. Ye, *J. Power Sources*, 2012, **201**, 340-346.

28.   H.-F. Ju, W.-L. Song and L.-Z. Fan, *J. Mater. Chem. A*, 2014, **2**, 10895-10903.

29.   T.-T. Chen, W.-L. Song and L.-Z. Fan, *Electrochim. Acta*, 2015, **165**, 92-97.

30.   W.-L. Song, K. Song and L.-Z. Fan, *ACS Appl. Mater. Interfaces*, 2015, **7**, 4257-4264.

31.   Z. Ling, G. Wang, Q. Dong, B. Qian, M. Zhang, C. Li and J. Qiu, *J. Mater. Chem. A*, 2014, **2**, 14329-14333.

32.   P. J. King, T. M. Higgins, S. De, N. Nicoloso and J. N. Coleman, *ACS Nano*, 2012, **6**, 1732-1741.

33.   X. Fan, Z. Peng, Y. Yang, H. Zhou and X. Guo, *J. Mater. Chem. A*, 2015, **3**, 10077-10084.

34.   A. Ghosh, L. Viet Thong, J. J. Bae and Y. H. Lee, *Sci. Rep.*, 2013, **3**, 2939.

35.   X. Chen, H. Wang, H. Yi, X. Wang, X. Yan and Z. Guo, *J. Phys. Chem. C*, 2014, **118**, 8262-8270.

36.   C. Choi, J. A. Lee, A. Y. Choi, Y. T. Kim, X. Lepro, M. D. Lima, R. H. Baughman and S. J. Kim, *Adv. Mater.*, 2014, **26**, 2059-2065.

37.   W. Li, F. Zhang, Y. Dou, Z. Wu, H. Liu, X. Qian, D. Gu, Y. Xia, B. Tu and D. Zhao, *Adv. Energy Mater.*, 2011, **1**, 382-386.

38.   K. Jost, D. Stenger, C. R. Perez, J. K. McDonough, K. Lian, Y. Gogotsi and G. Dion, *Energy Environ. Sci.*, 2013, **6**, 2698-2705.

39.   J. Ren, W. Bai, G. Guan, Y. Zhang and H. Peng, *Adv. Mater.*, 2013, **25**, 5965-5970.

40.   W. Zhou, K. Zhou, X. Liu, R. Hu, H. Liu and S. Chen, *J. Mater. Chem. A*, 2014, **2**, 7250-7255.

41.   P. He, L. Liu, W. Song, G. Xiong, T. S. Fisher and T. Chen, *RSC Adv.*, 2015, **5**, 31837-31844.

42.   A. B. Fuertes and M. Sevilla, *ACS Appl. Mater. Interfaces*, 2015, **7**, 4344-4353.

43. Y. Liang, L. Cai, L. Chen, X. Lin, R. Fu, M. Zhang and D. Wu, *Nanoscale*, 2015, **7**, 3971-3975.

44. R. Liu, L. Wan, S. Liu, L. Pan, D. Wu and D. Zhao, *Adv. Funct. Mater.*, 2015, **25**, 526-533.

45. M. Shen, C. Ruan, Y. Chen, C. Jiang, K. Ai and L. Lu, *ACS Appl. Mater. Interfaces*, 2015, **7**, 1207-1218.

46. T. Zhu, Y. Lu, S. Zheng, Y. Chen and H. Guo, *Electrochim. Acta*, 2015, **152**, 456-463.

47. L. L. Zhang, X. Zhao, H. Ji, M. D. Stoller, L. Lai, S. Murali, S. Mcdonnell, B. Cleveger, R. M. Wallace and R. S. Ruoff, *Energy Environ. Sci.*, 2012, **5**, 9618-9625.

48. Y. Wen, B. Wang, C. Huang, L. Wang and D. Hulicova-Jurcakova, *Chem.- Eur. J.*, 2015, **21**, 80-85.

49. Z.-S. Wu, K. Parvez, X. Feng and K. Muellen, *Nat. Comm.*, 2013, **4**, 2487.

50. K. Chen, S. Yin and D. Xue, *Nanoscale*, 2015, **7**, 1161-1166.

51. J. Chmiola, G. Yushin, Y. Gogotsi, C. Portet, P. Simon and P. L. Taberna, *Science*, 2006, **313**, 1760-1763.

52. J. Chmiola, C. Largeot, P.-L. Taberna, P. Simon and Y. Gogotsi, *Science*, 2010, **328**, 480-483.

53. P. Huang, M. Heon, D. Pech, M. Brunet, P.-L. Taberna, Y. Gogotsi, S. Lofland, J. D. Hettinger and P. Simon, *J. Power Sources*, 2013, **225**, 240-244.

54. M. Oschatz, L. Borchardt, K. Pinkert, S. Thieme, M. R. Lohe, C. Hoffmann, M. Benusch, F. M. Wisser, C. Ziegler and L. Giebeler, *Adv. Energy Mater.*, 2014, **4**, 1300645.

55. K. Pinkert, M. Oschatz, L. Borchardt, M. Klose, M. Zier, W. Nickel, L. Giebeler, S. Oswald, S. Kaskel and J. r. Eckert, *ACS Appl. Mater. Interfaces*, 2014, **6**, 2922-2928.

56. J. Xu, R. Zhang, C. Wu, Y. Zhao, X. Ye and S. Ge, *Carbon*, 2014, **74**, 226-236.

57. Y. Huang, J. Liang and Y. Chen, *Small*, 2012, **8**, 1805-1834.

58. Y.-E. Miao, W. Fan, D. Chen and T. Liu, *ACS Appl. Mater. Interfaces*, 2013, **5**, 4423-4428.

59. T. Liu, L. Finn, M. Yu, H. Wang, T. Zhai, X. Lu, Y. Tong and Y. Li, *Nano Lett.*, 2014, **14**, 2522-2527.

60. M. R. Arcila-Velez and M. E. Roberts, *Chem. Mater.*, 2014, **26**, 1601-1607.

61. C. Zhao, P. Gai, C. Liu, X. Wang, H. Xu, J. Zhang and J.-J. Zhu, *J. Mater. Chem. A*, 2013, **1**, 12587-12594.

62. G. P. Pandey, A. C. Rastogi and C. R. Westgate, *J. Power Sources*, 2014, **245**, 857-865.

63. K. Wang, H. Wu, Y. Meng and Z. Wei, *Small*, 2014, **10**, 14-31.

64. H. Zhang, L. Hu, J. Tu and S. Jiao, *Electrochim. Acta*, 2014, **120**, 122-127.

65. I. L. Chen, T.-Y. Chen, Y.-C. Wei, C.-C. Hu and T.-L. Lin, *Nanoscale*, 2014, **6**, 2861-2871.

66. S. Santhanagopalan, A. Balram and D. D. Meng, *ACS Nano*, 2013, **7**, 2114-2125.

67. H. Lee, Y.-J. Kim, D. J. Lee, J. Song, Y. M. Lee, H.-T. Kim and J.-K. Park, *J. Mater. Chem. A*, 2014, **2**, 11891-11898.

68. M. Huang, F. Li, J. Y. Ji, Y. X. Zhang, X. L. Zhao and X. Gao, *CrystEngComm*, 2014, **16**, 2878-2884.

69. Y. X. Zhang, M. Huang, F. Li and Z. Q. Wen, *Int. J. Electrochem. Sci.*, 2013, **8**, 8645-8661.

70. M. Zhang, K. Chen, X. Chen, X. Peng, X. Sun and D. Xue, *CrystEngComm*, 2015, **17**, 1917-1922.

71. J. Ji, L. L. Zhang, H. Ji, Y. Li, X. Zhao, X. Bai, X. Fan, F. Zhang and R. S. Ruoff, *ACS Nano*, 2013, **7**, 6237-6243.

72. S. Gao, Y. Sun, F. Lei, L. Liang, J. Liu, W. Bi, B. Pan and Y. Xie, *Angew. Chem. Int. Ed.*, 2014,

53, 12789-12793.

73. T. Zhai, S. Xie, M. Yu, P. Fang, C. Liang, X. Lu and Y. Tong, *Nano Energy*, 2014, **8**, 255-263.

74. L. Zhao, J. Yu, W. Li, S. Wang, C. Dai, J. Wu, X. Bai and C. Zhi, *Nano Energy*, 2014, **4**, 39-48.

75. W. Yao, J. Wang, H. Li and Y. Lu, *J. Power Sources*, 2014, **247**, 824-830.

76. Z. Wen, W. She, Y. Li and R. Che, *J. Mater. Chem. A*, 2014, **2**, 20729-20738.

77. C.-L. Tang, X. Wei, Y.-M. Jiang, X.-Y. Wu, L. N. Han, K.-X. Wang and J.-S. Chen, *J. Phys. Chem. C*, 2015, **119**, 8465-8471.

78. F. Li, G. Li, H. Chen, J. Q. Jia, F. Dong, Y. B. Hu, Z. G. Shang and Y. X. Zhang, *J. Power Sources*, 2015, **296**, 86-91.

79. S. J. Zhu, J. Q. Jia, T. Wang, D. Zhao, J. Yang, F. Dong, Z. G. Shang and Y. X. Zhang, *Chem. Commun.*, 2015. DOI: 10.1039/c5cc03976b.

80. H. Y. Lee and J. B. Goodenough, *J. Solid State Chem.*, 1999, **144**, 220-223.

81. Y. Hu and J. Wang, *J. Power Sources*, 2015, **286**, 394-399.

82. X. Tang, Z.-h. Liu, C. Zhang, Z. Yang and Z. Wang, *J. Power Sources*, 2009, **193**, 939-943.

83. W. Li, K. Xu, B. Li, J. Sun, F. Jiang, Z. Yu, R. Zou, Z. Chen and J. Hu, *ChemElectroChem*, 2014, **1**, 1003-1008.

84. P. Yang, Y. Ding, Z. Lin, Z. Chen, Y. Li, P. Qiang, M. Ebrahimi, W. Mai, C. P. Wong and Z. L. Wang, *Nano Lett.*, 2014, **14**, 731-736.

85. X. Lu, D. Zheng, T. Zhai, Z. Liu, Y. Huang, S. Xie and Y. Tong, *Energy Environ. Sci.*, 2011, **4**, 2915-2921.

86. Y. Qiu, P. Xu, B. Guo, Z. Cheng, H. Fan, M. Yang, X. Yang and J. Li, *RSC Adv.*, 2014, **4**, 64187-64192.

87. M. Huang, Y. Zhang, F. Li, L. Zhang, R. S. Ruoff, Z. Wen and Q. Liu, *Sci. Rep.*, 2014, **4**, 3878.

88. K. Xiao, J.-W. Li, G.-F. Chen, Z.-Q. Liu, N. Li and Y.-Z. Su, *Electrochim. Acta*, 2014, **149**, 341-348.

89. A. Bahloul, B. Nessark, E. Briot, H. Groult, A. Mauger, K. Zaghib and C. M. Julien, *J. Power Sources*, 2013, **240**, 267-272.

90. C. Wang, Y. Zhan, L. Wu, Y. Li and J. Liu, *Nanotechnology*, 2014, **25**, 305401.

91. C. Choi, S. H. Kim, H. J. Sim, J. A. Lee, A. Y. Choi, Y. T. Kim, X. Lepro, G. M. Spinks, R. H. Baughman and S. J. Kim, *Sci. Rep.*, 2015, **5**, 9387.

92. L.-F. Chen, Z.-H. Huang, H.-W. Liang, Q.-F. Guan and S.-H. Yu, *Adv. Mater.*, 2013, **25**, 4746-4752.

93. G. Wang, H. Xu, L. Lu and H. Zhao, *J. Mater. Chem. A*, 2015, **3**, 1127-1132.

94. X. Zhao, L. Zhang, S. Murali, M. D. Stoller, Q. Zhang, Y. Zhu and R. S. Ruoff, *ACS Nano*, 2012, **6**, 5404-5412.

95. M. Toupin, T. Brousse and D. Belanger, *Chem. Mater.*, 2004, **16**, 3184-3190.

96. O. Ghodbane, F. Ataherian, N.-L. Wu and F. Favier, *J. Power Sources*, 2012, **206**, 454-462.

97. C. Xu, F. Kang, B. Li and H. Du, *J. Mater. Res.*, 2010, **25**, 1421-1432.

98. S. C. Pang, M. A. Anderson and T. W. Chapman, *J. Electrochem. Soc.*, 2000, **147**, 444-450.

99. O. Ghodbane, J.-L. Pascal and F. Favier, *ACS Appl. Mater. Interfaces*, 2009, **1**, 1130-1139.

100. C.-C. Hu and T.-W. Tsou, *Electrochem. Commun.*, 2002, **4**, 105-109.

101. V. Subramanian, H. Zhu, R. Vajtai, P. Ajayan and B. Wei, *J. Phys. Chem. B*, 2005, **109**,

20207-20214.

102. Y. Zhang, C. Sun, P. Lu, K. Li, S. Song and D. Xue, *CrystEngComm*, 2012, **14**, 5892-5897.

103. T. Brousse, M. Toupin, R. Dugas, L. Athouël, O. Crosnier and D. Bélanger, *J. Electrochem. Soc.*, 2006, **153**, A2171-A2180.

104. J. W. Kim, V. Augustyn and B. Dunn, *Adv. Energy Mater.*, 2012, **2**, 141-148.

105. F. Ran, H. Fan, L. Wang, L. Zhao, Y. Tan, X. Zhang, L. Kong and L. Kang, *J. Energy Chem.*, 2013, **22**, 928-934.

106. S. Devaraj and N. Munichandraiah, *J. Phys. Chem. C*, 2008, **112**, 4406-4417.

107. S. L. Brock, N. G. Duan, Z. R. Tian, O. Giraldo, H. Zhou and S. L. Suib, *Chem. Mater.*, 1998, **10**, 2619-2628.

108. M. M. Thackeray, *Prog. Solid State Chem.*, 1997, **25**, 1-71.

109. P. M. Dewolff, *Acta Crystallogr.*, 1959, **12**, 341-345.

110. R. H. Ma, Y. Bando, L. Q. Zhang and T. Sasaki, *Adv. Mater.*, 2004, **16**, 918-922.

111. R. Liu and S. B. Lee, *J. Am. Chem. Soc.*, 2008, **130**, 2942-2943.

112. M.-S. Wu, *Appl. Phys. Lett.*, 2005, **87**, 153102.

113. W. Li, K. Xu, L. An, F. Jiang, X. Zhou, J. Yang, Z. Chen, R. Zou and J. Hu, *J. Mater. Chem. A*, 2014, **2**, 1443-1447.

114. M. Xu, L. Kong, W. Zhou and H. Li, *J. Phys. Chem. C*, 2007, **111**, 19141-19147.

115. S. Park, I. Nam, G.-P. Kim, J. W. Han and J. Yi, *ACS Appl. Mater. Interfaces*, 2013, **5**, 9908-9912.

116. Z. Yu, B. Duong, D. Abbitt and J. Thomas, *Adv. Mater.*, 2013, **25**, 3302-3306.

117. X. Xie, C. Zhang, M.-B. Wu, Y. Tao, W. Lv and Q.-H. Yang, *Chem. Commun.*, 2013, **49**, 11092-11094.

118. A. M. Hashem, H. M. Abuzeid, N. Narayanan, H. Ehrenberg and C. Julien, *Mater. Chem. Phys.*, 2011, **130**, 33-38.

119. R. Poonguzhali, N. Shanmugam, R. Gobi, A. Senthilkumar, R. Shanmugam and K. Sathishkumar, *RSC Adv.*, 2015, **5**, 45407-45415.

120. Y.-S. Wang, D.-S. Tsai, W.-H. Chung, Y.-S. Syu and Y.-S. Huang, *Electrochim. Acta*, 2012, **68**, 95-102.

121. G. Wang, L. Liu, L. Zhang and J. Zhang, *Ionics*, 2013, **19**, 689-695.

122. G. Yu, L. Hu, N. Liu, H. Wang, M. Vosgueritchian, Y. Yang, Y. Cui and Z. Bao, *Nano Lett.*, 2011, **11**, 4438-4442.

123. Y. Hou, Y. Cheng, T. Hobson and J. Liu, *Nano Lett.*, 2010, **10**, 2727-2733.

124. J.-G. Wang, Y. Yang, Z.-H. Huang and F. Kang, *Electrochim. Acta*, 2011, **56**, 9240-9247.

125. P. Lv, Y. Y. Feng, Y. Li and W. Feng, *J. Power Sources*, 2012, **220**, 160-168.

126. Y. Liu, K. Shi and I. Zhitomirsky, *Colloids Surf. A*, 2014, **446**, 15-22.

127. Y. Liu, M. S. Ata, K. Shi, G. z. Zhu, G. A. Botton and I. Zhitomirsky, *RSC Adv.*, 2014, **4**, 29652-29659.

128. S. Hassan, M. Suzuki, S. Mori and A. A. El-Moneim, *RSC Adv.*, 2014, **4**, 20479-20488.

129. J. Yan, E. Khoo, A. Sumboja and P. S. Lee, *ACS Nano*, 2010, **4**, 4247-4255.

130. T. Bordjiba and D. Bélanger, *Electrochim. Acta*, 2010, **55**, 3428-3433.

131. S. W. Lee, J. Kim, S. Chen, P. T. Hammond and Y. Shao-Horn, *ACS Nano*, 2010, **4**, 3889-3896.

132. H. Zheng, F. Tang, Y. Jia, L. Wang, Y. Chen, M. Lim, L. Zhang and G. M. Lu, *Carbon*, 2009,

47, 1534-1542.

133. K.-W. Nam, C.-W. Lee, X.-Q. Yang, B. W. Cho, W.-S. Yoon and K.-B. Kim, *J. Power Sources*, 2009, **188**, 323-331.

134. R. Amade, E. Jover, B. Caglar, T. Mutlu and E. Bertran, *J. Power Sources*, 2011, **196**, 5779-5783.

135. J. Qian, H. Jin, B. Chen, M. Lin, W. Lu, W. M. Tang, W. Xiong, L. W. H. Chan, S. P. Lau and J. Yuan, *Angew. Chem. Int. Ed.*, 2015, **54**, 6800-6803.

136. L. Chen, J. Kang, Y. Hou, P. Liu, T. Fujita, A. Hirata and M. Chen, *J. Mater. Chem. A*, 2013, **1**, 9202-9207.

137. P. Simon and A. Burke, *Electrochem. Soc. Interface*, 2008, **17**, 38-43.

138. X. Zhang, D. Zhao, Y. Zhao, P. Tang, Y. Shen, C. Xu, H. Li and Y. Xiao, *J. Mater. Chem. A*, 2013, **1**, 3706-3712.

139. S. Maiti, A. Pramanik and S. Mahanty, *RSC Adv.*, 2015, **5**, 41617-41626.

140. M. Cao, X. He, J. Chen and C. Hu, *Cryst. Growth Des.*, 2007, **7**, 170-174.

141. X. Feng, N. Chen, Y. Zhang, Z. Yan, X. Liu, Y. Ma, Q. Shen, L. Wang and W. Huang, *J. Mater. Chem. A*, 2014, **2**, 9178-9184.

142. Y. Liu, D. He, H. Wu, J. Duan and Y. Zhang, *Electrochim. Acta*, 2015, **164**, 154-162.

143. C. X. Guo, A. A. Chitre and X. Lu, *Phys. Chem. Chem. Phys.*, 2014, **16**, 4672-4678.

144. H. Chen, X. Dong, J. Shi, J. Zhao, Z. Hua, J. Gao, M. Ruan and D. Yan, *J. Mater. Chem.*, 2007, **17**, 855-860.

145. Y. X. Zhang, M. Huang, F. Li, X. L. Wang and Z. Q. Wen, *J. Power Sources*, 2014, **246**, 449-456.

146. C. Xu, Y. Zhao, G. Yang, F. Li and H. Li, *Chem. Commun.*, 2009, 7575-7577.

147. Y. Zhang, M. Dong, S. Zhu, C. Liu and Z. Wen, *Mater. Res. Bull.*, 2014, **49**, 448-453.

148. J. Ma, Q. Cheng, V. Pavlinek, P. Saha and C. Li, *New J. Chem.*, 2013, **37**, 722-728.

149. L. Li, P. Hua, X. Tian, C. Yang and Z. Pi, *Electrochim. Acta*, 2010, **55**, 1682-1686.

150. J. Zhao, H. Chen, J. Shi, J. Gu, X. Dong, J. Gao, M. Ruan and L. Yu, *Microporous Mesoporous Mater.*, 2008, **116**, 432-438.

151. D. Losic, J. G. Mitchell, R. Lal and N. H. Voelcker, *Adv. Funct. Mater.*, 2007, **17**, 2439-2446.

152. Y. X. Zhang, F. Li, M. Huang, Y. Xing, X. Gao, B. Li, Z. Y. Guo and Y. M. Guan, *Mater. Lett.*, 2014, **120**, 263-266.

153. F. Li, Y. Xing, M. Huang, K. L. Li, T. T. Yu, Y. X. Zhang and D. Losic, *J. Mater. Chem. A*, 2015, **3**, 7855-7861.

154. N. W. Liu, A. Datta, C. Y. Liu, C. Y. Peng, H. H. Wang and Y. L. Wang, *Adv. Mater.*, 2005, **17**, 222-225.

155. F. Grote, R.-S. Kühnel, A. Balducci and Y. Lei, *Appl. Phys. Lett.*, 2014, **104**, 053904.

156. H. Liu, B. Lu, S. Wei, M. Bao, Y. Wen and F. Wang, *Solid State Sci.*, 2012, **14**, 789-793.

157. X. Wang, X. Wang, W. Huang, P. Sebastian and S. Gamboa, *J. Power Sources*, 2005, **140**, 211-215.

158. H. Xia, J. Feng, H. Wang, M. O. Lai and L. Lu, *J. Power Sources*, 2010, **195**, 4410-4413.

159. J. Duay, S. A. Sherrill, Z. Gui, E. Gillette and S. B. Lee, *ACS Nano*, 2013, **7**, 1200-1214.

160. F. Li, Y. X. Zhang, M. Huang, Y. Xing and L. L. Zhang, *Electrochim. Acta*, 2015, **154**, 329-337.

161. S.-W. Bian, Y.-P. Zhao and C.-Y. Xian, *Mater. Lett.*, 2013, **111**, 75-77.

162. T.-D. Dang, A. N. Banerjee, S. W. Joo and B.-K. Min, *Ind. Eng. Chem. Res.*, 2014, **53**, 9743-9753.

163. J. Zhu, W. Shi, N. Xiao, X. Rui, H. Tan, X. Lu, H. H. Hng, J. Ma and Q. Yan, *ACS Appl. Mater. Interfaces*, 2012, **4**, 2769-2774.

164. T. Liu, Y. Huang, Z. Liang and Y.-E. Miao, *ChemNanoMat*, 2015, 1, 159-166.

165. Y. Zhang, L. Li, H. Su, W. Huang and X. Dong, *J. Mater. Chem. A*, 2015, **3**, 43-59.

166. H. Zhang, J. Gu, Y. Jiang, Y. Wang, J. Zhao, X. Zhang and C. Wang, *Energy Convers. Manag.*, 2014, **86**, 605-613.

167. Y. Dai, J. Li, G. Yan, G. Xu, Q. Xue and F. Kang, *J. Alloys Compd.*, 2015, **621**, 86-92.

168. L. Coustan, A. Le Comte, T. Brousse and F. Favier, *Electrochim. Acta*, 2015, **152**, 520-529.

169. H. Zhang, J. Gu, Y. Jiang, J. Zhao, X. Zhang and C. Wang, *J. Solid State Electrochem.*, 2014, **18**, 235-247.

170. C. J. Jafta, F. Nkosi, L. le Roux, M. K. Mathe, M. Kebede, K. Makgopa, Y. Song, D. Tong, M. Oyama and N. Manyala, *Electrochim. Acta*, 2013, **110**, 228-233.

171. M. Sawangphruk, S. Pinitsoontorn and J. Limtrakul, *J. Solid State Electrochem.*, 2012, **16**, 2623-2629.

172. H. Zhang, Y. Wang, C. Liu and H. Jiang, *J. Alloys Compd.*, 2012, **517**, 1-8.

173. Y. Li, X. Cai and W. Shen, *Electrochim. Acta*, 2014, **149**, 306-315.

174. J. Zhou, L. Yu, M. Sun, F. Ye, B. Lan, G. Diao and J. He, *J. Solid State Chem.*, 2013, **198**, 371-378.

175. Y. Du, X. Zhao, Z. Huang, Y. Li and Q. Zhang, *RSC Adv.*, 2014, **4**, 39087-39094.

176. D. Zheng, S. Sun, W. Fan, H. Yu, C. Fan, G. Cao, Z. Yin and X. Song, *J. Phys. Chem. B*, 2005, **109**, 16439-16443.

177. N. Wang, X. Cao, G. Lin and Y. Shihe, *Nanotechnology*, 2007, **18**, 475605.

178. J. Zhou, L. Yu, M. Sun, S. Yang, F. Ye, J. He and Z. Hao, *Ind. Eng. Chem. Res.*, 2013, **52**, 9586-9593.

179. R. Jiang, T. Huang, J. Liu, J. Zhuang and A. Yu, *Electrochim. Acta*, 2009, **54**, 3047-3052.

180. C. Yuan, L. Hou, L. Yang, D. Li, L. Shen, F. Zhang and X. Zhang, *J. Mater. Chem.*, 2011, **21**, 16035-16041.

181. H. Zhang, J. Gu, J. Tong, C. Ma, J. Zhao, X. Zhang and C. Wang, *Energy Convers. Manag.*, 2015, **91**, 120-131.

182. M. Dong, Y. X. Zhang, H. F. Song, X. Qiu, X. D. Hao, C. P. Liu, Y. Yuan, X. L. Li and J. M. Huang, *Physica E*, 2012, **45**, 103-108.

183. S. Jana, S. Pande, A. K. Sinha and T. Pal, *Inorg. Chem.*, 2008, **47**, 5558-5560.

184. S. R. Ede, S. Anantharaj, U. Nithiyanantham and S. Kundu, *Phys. Chem. Chem. Phys.*, 2015, **17**, 5474-5484.

185. B. G. S. Raj, A. M. Asiri, A. H. Qusti, J. J. Wu and S. Anandan, *Ultrason. Sonochem.*, 2014, **21**, 1933-1938.

186. M. Lashanizadegan and H. Mirzazadeh, *Asian J. Chem.*, 2013, **25**, 1425.

187. B. Lu, S. Chen and K. Kawamoto, *Mater. Res. Bull.*, 2012, **47**, 3619-3624.

188. Z. Liu, K. Xu, H. Sun and S. Yin, *Small*, 2015, **11**, 2182-2191.

189. W. Li, Q. Liu, Y. Sun, J. Sun, R. Zou, G. Li, X. Hu, G. Song, G. Ma and J. Yang, *J. Mater. Chem.*, 2012, **22**, 14864-14867.

190. P. Wang, Y.-J. Zhao, L.-X. Wen, J.-F. Chen and Z.-G. Lei, *Ind. Eng. Chem. Res.*, 2014, **53**,

20116-20123.

191.   W.-Y. Ko, L.-J. Chen, Y.-H. Chen and K.-J. Lin, *J. Mater. Res.*, 2014, **29**, 107-114.

192.   Y. Wang, S. Indrawirawan, X. Duan, H. Sun, H. M. Ang, M. O. Tade and S. Wang, *Chem. Eng. J.*, 2015, **266**, 12-20.

193.   S. Zhu, H. Zhang, P. Chen, L.-H. Nie, C.-H. Li and S.-K. Li, *J. Mater. Chem. A*, 2015, **3**, 1540-1548.

194.   W. Li, R. Zeng, Z. Sun, D. Tian and S. Dou, *Sci. Rep.*, 2014, **4**, 6641.

195.   A. M. Toufiq, F. Wang, Q. Li and Y. Li, *Appl. Phys. A*, 2014, **116**, 1127-1132.

196.   Y.-F. Li, S.-S. Li, D.-L. Zhou, A.-J. Wang, P.-P. Zhang, C.-G. Li and J.-J. Feng, *J. Solid State Electrochem.*, 2014, **18**, 2521-2527.

197.   B. Lan, M. Sun, T. Lin, G. Cheng, L. Yu, S. Peng and J. Xu, *Mater. Lett.*, 2014, **121**, 234-237.

198.   A. K. Sinha, M. Pradhan and T. Pal, *J. Phys. Chem. C*, 2013, **117**, 23976-23986.

199.   Z. Song, W. Liu, M. Zhao, Y. Zhang, G. Liu, C. Yu and J. Qiu, *J. Alloys Compd.*, 2013, **560**, 151-155.

200.   D. Su, H.-J. Ahn and G. Wang, *J. Mater. Chem. A*, 2013, **1**, 4845-4850.

201.   X. Su, L. Yu, G. Cheng, H. Zhang, M. Sun, L. Zhang and J. Zhang, *Appl. Energy*, 2014, **134**, 439-445.

202.   X. Zhang, P. Yu, H. Zhang, D. Zhang, X. Sun and Y. Ma, *Electrochim. Acta*, 2013, **89**, 523-529.

203.   G. Zhang, Y. Yan, L. Song, Q. Yue, F. Qu and X. Zhang, *Sci. Adv. Mater.*, 2012, **4**, 1179-1184.

204.   F. Wang, H. Dai, J. Deng, G. Bai, K. Ji and Y. Liu, *Environ. Sci. Technol.*, 2012, **46**, 4034-4041.

205.   D. Li, J. Yang, W. Tang, X. Wu, L. Wei and Y. Chen, *RSC Adv.*, 2014, **4**, 26796-26803.

206.   R. Chen, J. Yu and W. Xiao, *J. Mater. Chem. A*, 2013, **1**, 11682-11690.

207.   D. Li, X. Wu and Y. Chen, *J. Phys. Chem. C*, 2013, **117**, 11040-11046.

208.   Y. Munaiah, B. G. S. Raj, T. P. Kumar and P. Ragupathy, *J. Mater. Chem. A*, 2013, **1**, 4300-4306.

209.   L. Jin, L. Xu, C. Morein, C. h. Chen, M. Lai, S. Dharmarathna, A. Dobley and S. L. Suib, *Adv. Funct. Mater.*, 2010, **20**, 3373-3382.

210.   J. Wu, Q. Wang, A. Umar, S. Sun, L. Huang, J. Wang and Y. Gao, *New J. Chem.*, 2014, **38**, 4420-4426.

211.   H. Zhao, Y. Dong, P. Jiang, G. Wang, J. Zhang, K. Li and C. Feng, *New J. Chem.*, 2014, **38**, 1743-1750.

212.   W. Xiao, H. Xia, J. Y. Fuh and L. Lu, *J. Power Sources*, 2009, **193**, 935-938.

213.   M. Pang, G. Long, S. Jiang, Y. Ji, W. Han, B. Wang, X. Liu and Y. Xi, *Electrochim. Acta*, 2015, **161**, 297-304.

214.   Y. Li, D. Cao, Y. Wang, S. Yang, D. Zhang, K. Ye, K. Cheng, J. Yin, G. Wang and Y. Xu, *J. Power Sources*, 2015, **279**, 138-145.

215.   S. Park, H.-W. Shim, C. W. Lee, H. J. Song, I. J. Park, J.-C. Kim, K. S. Hong and D.-W. Kim, *Nano Res.*, 2015, 8, 990-1004.

216.   K. Selvakumar, S. M. S. Kumar, R. Thangamuthu, K. Ganesan, P. Murugan, P. Rajput, S. N. Jha and D. Bhattacharyya, *J. Phys. Chem. C*, 2015, **119**, 6604-6618.

217.   S. Ghasemi, R. Hosseinzadeh and M. Jafari, *Int. J. Hydrogen Energy*, 2015, **40**, 1037-1046.

218.   J.-H. Moon, H. Munakata, K. Kajihara and K. Kanamura, *Electrochem.*, 2013, **81**, 2-6.

54

219.   C. Wei, H. Pang, B. Zhang, Q. Lu, S. Liang and F. Gao, *Sci. Rep.*, 2013, **3**, 2193.

220.   S.-C. Pang and M. A. Anderson, *J. Mater. Res.*, 2000, **15**, 2096-2106.

221.   R. N. Reddy and R. G. Reddy, *J. Power Sources*, 2003, **124**, 330-337.

222.   C.-Y. Chen, S.-C. Wang, Y.-H. Tien, W.-T. Tsai and C.-K. Lin, *Thin Solid Films*, 2009, **518**, 1557-1560.

223.   C. C. Chen, C.-Y. Tsay, H.-S. Lin, W. D. Jheng and C.-K. Lin, *Mater. Chem. Phys.*, 2012, **137**, 503-510.

224.   L. L. Yu, J. J. Zhu and J. T. Zhao, *Eur. J. Inorg. Chem.*, 2013, **2013**, 3719-3725.

225.   A. S. Poyraz, W. Song, D. Kriz, C.-H. Kuo, M. S. Seraji and S. L. Suib, *ACS Appl. Mater. Interfaces*, 2014, **6**, 10986-10991.

226.   A. Sarkar, A. K. Satpati, V. Kumar and S. Kumar, *Electrochim. Acta*, 2015, **167**, 126-131.

227.   I. Bilecka and M. Niederberger, *Nanoscale*, 2010, **2**, 1358-1374.

228.   T. T. Truong, Y. Liu, Y. Ren, L. Trahey and Y. Sun, *ACS Nano*, 2012, **6**, 8067-8077.

229.   L. R. Pahalagedara, S. Dharmarathna, C. K. King'ondu, M. N. Pahalagedara, Y. Meng, C.-H. Kuo and S. L. Suib, *J. Phys. Chem. C*, 2014, **118**, 20363-20373.

230.   E. K. Nyutu, C.-H. Chen, S. Sithambaram, V. M. B. Crisostomo and S. L. Suib, *J. Phys. Chem. C*, 2008, **112**, 6786-6793.

231.   P. Yu, X. Zhang, Y. Chen, Y. Ma and Z. Qi, *Mater. Chem. Phys.*, 2009, **118**, 303-307.

232.   Y. Li, J. Wang, Y. Zhang, M. N. Banis, J. Liu, D. Geng, R. Li and X. Sun, *J. Colloid Interface Sci.*, 2012, **369**, 123-128.

233.   X. Zhang, X. Sun, H. Zhang, D. Zhang and Y. Ma, *Electrochim. Acta*, 2013, **87**, 637-644.

234.   S. K. Meher and G. R. Rao, *J. Power Sources*, 2012, **215**, 317-328.

235.   A. Bello, O. Fashedemi, M. Fabiane, J. Lekitima, K. Ozoemena and N. Manyala, *Electrochim. Acta*, 2013, **114**, 48-53.

236.   B. Ming, J. Li, F. Kang, G. Pang, Y. Zhang, L. Chen, J. Xu and X. Wang, *J. Power Sources*, 2012, **198**, 428-431.

237.   K. Chen, Y. Dong Noh, K. Li, S. Komarneni and D. Xue, *J. Phys. Chem. C*, 2013, **117**, 10770-10779.

238.   M. Nakayama, T. Kanaya and R. Inoue, *Electrochem. Commun.*, 2007, **9**, 1154-1158.

239.   M.-S. Wu, Z.-S. Guo and J.-J. Jow, *J. Phys. Chem. C*, 2010, **114**, 21861-21867.

240.   W. Yan, T. Ayvazian, J. Kim, Y. Liu, K. C. Donavan, W. Xing, Y. Yang, J. C. Hemminger and R. M. Penner, *ACS Nano*, 2011, **5**, 8275-8287.

241.   C.-L. Ho and M.-S. Wu, *J. Phys. Chem. C*, 2011, **115**, 22068-22074.

242.   J. Xiao, S. Yang, L. Wan, F. Xiao and S. Wang, *J. Power Sources*, 2014, **245**, 1027-1034.

243.   P. Yang, Y. Li, Z. Lin, Y. Ding, S. Yue, C. P. Wong, X. Cai, S. Tan and W. Mai, *J. Mater. Chem. A*, 2014, **2**, 595-599.

244.   B. Babakhani and D. G. Ivey, *J. Power Sources*, 2011, **196**, 10762-10774.

245.   X. Hu, X. Lin, Z. Ling, Y. Li and X. Fu, *Electrochim. Acta*, 2014, **138**, 132-138.

246.   S. Hassan, M. Suzuki, S. Mori and A. A. El-Moneim, *J. Power Sources*, 2014, **249**, 21-27.

247.   S.-L. Chou, J.-Z. Wang, S.-Y. Chew, H.-K. Liu and S.-X. Dou, *Electrochem. Commun.*, 2008, **10**, 1724-1727.

248.   S. H. Lee, H. Lee, M. S. Cho, J.-D. Nam and Y. Lee, *J. Mater. Chem. A*, 2013, **1**, 14606-14611.

249.   M. F. Dupont and S. W. Donne, *Electrochim. Acta*, 2014, **120**, 219-225.

250. Z. Sun, S. Firdoz, E. Y.-X. Yap, L. Li and X. Lu, *Nanoscale*, 2013, **5**, 4379-4387.

251. J. Yang, L. Lian, H. Ruan, F. Xie and M. Wei, *Electrochim. Acta*, 2014, **136**, 189-194.

252. A. Greiner and J. H. Wendorff, *Angew. Chem. Int. Ed.*, 2007, **46**, 5670-5703.

253. M.-R. Gao, Y.-F. Xu, J. Jiang and S.-H. Yu, *Chem. Soc. Rev.*, 2013, **42**, 2986-3017.

254. H.-q. Liu, X.-l. Yu, B. Cai, S.-j. You, Z.-b. He, Q.-q. Huang, L. Rao, S.-s. Li, C. Liu and W.-w. Sun, *Appl. Phys. Lett.*, 2015, **106**, 093703.

255. X. Li, G. Wang, X. Wang, X. Li and J. Ji, *J. Mater. Chem. A*, 2013, **1**, 10103-10106.

256. H. Huang, W. Zhang, Y. Fu and X. Wang, *Electrochim. Acta*, 2015, **152**, 480-488.

257. H.-W. Chang, Y.-R. Lu, J.-L. Chen, C.-L. Chen, J.-F. Lee, J.-M. Chen, Y.-C. Tsai, C.-M. Chang, P.-H. Yeh and W.-C. Chou, *Nanoscale*, 2015, **7**, 1725-1735.

258. X. Li and B. Wei, *Nano Energy*, 2012, **1**, 479-487.

259. L. Hu, W. Chen, X. Xie, N. Liu, Y. Yang, H. Wu, Y. Yao, M. Pasta, H. N. Alshareef and Y. Cui, *ACS Nano*, 2011, **5**, 8904-8913.

260. G. Mo, Y. Zhang, W. Zhang and J. Ye, *Electrochim. Acta*, 2013, **113**, 373-381.

261. H. Zhang, G. Cao, Z. Wang, Y. Yang, Z. Shi and Z. Gu, *Nano Lett.*, 2008, **8**, 2664-2668.

262. L. Li, Z. A. Hu, N. An, Y. Y. Yang, Z. M. Li and H. Y. Wu, *J. Phys. Chem. C*, 2014, **118**, 22865-22872.

263. L. Du, P. Yang, X. Yu, P. Liu, J. Song and W. Mai, *J. Mater. Chem. A*, 2014, **2**, 17561-17567.

264. M. Huang, R. Mi, H. Liu, F. Li, X. L. Zhao, W. Zhang, S. X. He and Y. X. Zhang, *J. Power Sources*, 2014, **269**, 760-767.

265. K. Shi, M. Ren and I. Zhitomirsky, *ACS Sustainable Chem. Eng.*, 2014, **2**, 1289-1298.

266. K. Shi and I. Zhitomirsky, *ChemElectroChem*, 2015, **2**, 396-403.

267. M. D. Stoller, S. Park, Y. Zhu, J. An and R. S. Ruoff, *Nano Lett.*, 2008, **8**, 3498-3502.

268. Z.-S. Wu, W. Ren, D.-W. Wang, F. Li, B. Liu and H.-M. Cheng, *ACS Nano*, 2010, **4**, 5835-5842.

269. H. Huang and X. Wang, *Nanoscale*, 2011, **3**, 3185-3191.

270. X. Feng, Z. Yan, N. Chen, Y. Zhang, Y. Ma, X. Liu, Q. Fan, L. Wang and W. Huang, *J. Mater. Chem. A*, 2013, **1**, 12818-12825.

271. S. Yang, X. Song, P. Zhang and L. Gao, *ACS Appl. Mater. Interfaces*, 2013, **5**, 3317-3322.

272. L. Peng, X. Peng, B. Liu, C. Wu, Y. Xie and G. Yu, *Nano Lett.*, 2013, **13**, 2151-2157.

273. K. Dai, L. Lu, C. Liang, J. Dai, Q. Liu, Y. Zhang, G. Zhu and Z. Liu, *Electrochim. Acta*, 2014, **116**, 111-117.

274. Y. Zhao, W. Ran, J. He, Y. Huang, Z. Liu, W. Liu, Y. Tang, L. Zhang, D. Gao and F. Gao, *Small*, 2015, **11**, 1310-1319.

275. M.-S. Wu and Y.-H. Fu, *Carbon*, 2013, **60**, 236-245.

276. L. Li, A. R. O. Raji and J. M. Tour, *Adv. Mater.*, 2013, **25**, 6298-6302.

277. M. Liu, W. W. Tjiu, J. Pan, C. Zhang, W. Gao and T. Liu, *Nanoscale*, 2014, **6**, 4233-4242.

278. H. R. Naderi, H. R. Mortaheb and A. Zolfaghari, *J. Electroanal. Chem.*, 2014, **719**, 98-105.

279. Y. Song, D.-Y. Feng, T.-Y. Liu, Y. Li and X.-X. Liu, *Nanoscale*, 2015, **7**, 3581-3587.

280. H. Gao, F. Xiao, C. B. Ching and H. Duan, *ACS Appl. Mater. Interfaces*, 2012, **4**, 2801-2810.

281. Y. Sun, Y. Cheng, K. He, A. Zhou and H. Duan, *RSC Adv.*, 2015, **5**, 10178-10186.

282. Y. He, W. Chen, X. Li, Z. Zhang, J. Fu, C. Zhao and E. Xie, *ACS Nano*, 2012, **7**, 174-182.

283. T. Zhai, F. Wang, M. Yu, S. Xie, C. Liang, C. Li, F. Xiao, R. Tang, Q. Wu and X. Lu, *Nanoscale*, 2013, **5**, 6790-6796.

284. X. Sun, H. Wang, Z. Lei, Z. Liu and L. Wei, *RSC Adv.*, 2014, **4**, 30233-30240.

285. Z. Chen, W. Ren, L. Gao, B. Liu, S. Pei and H.-M. Cheng, *Nat. Mater.*, 2011, **10**, 424-428.

286. C. Yang, M. Zhou and Q. Xu, *Phys. Chem. Chem. Phys.*, 2013, **15**, 19730-19740.

287. M. Liu, L. Gan, W. Xiong, Z. Xu, D. Zhu and L. Chen, *J. Mater. Chem. A*, 2014, **2**, 2555-2562.

288. H. Li, L. Jiang, Q. Cheng, Y. He, V. Pavlinek, P. Saha and C. Li, *Electrochim. Acta*, 2015, **164**, 252-259.

289. L. Wang, Y. Zheng, S. Chen, Y. Ye, F. Xu, H. Tan, Z. Li, H. Hou and Y. Song, *Electrochim. Acta*, 2014, **135**, 380-387.

290. J.-G. Wang, Y. Yang, Z.-H. Huang and F. Kang, *J. Power Sources*, 2013, **224**, 86-92.

291. J.-G. Wang, Y. Yang, Z.-H. Huang and F. Kang, *Carbon*, 2013, **61**, 190-199.

292. M. Zhi, A. Manivannan, F. Meng and N. Wu, *J. Power Sources*, 2012, **208**, 345-353.

293. X. Zhang, J. Ma, W. Yang, Z. Gao, J. Wang, Q. Liu, J. Liu and X. Jing, *CrystEngComm*, 2014, **16**, 4016-4022.

294. Z. Lei, J. Zhang and X. Zhao, *J. Mater. Chem.*, 2012, **22**, 153-160.

295. Y. Zhao, Y. Meng and P. Jiang, *J. Power Sources*, 2014, **259**, 219-226.

296. L. Li, R. Li, S. Gai, S. Ding, F. He, M. Zhang and P. Yang, *Chem.- Eur. J.*, 2015, **21**, 7119-7126.

297. A. E. Fischer, K. A. Pettigrew, D. R. Rolison, R. M. Stroud and J. W. Long, *Nano Lett.*, 2007, **7**, 281-286.

298. W. Wei, X. Cui, W. Chen and D. G. Ivey, *Chem. Soc. Rev.*, 2011, **40**, 1697-1721.

299. G. Lv, D. Wu and R. Fu, *J. Non-Cryst. Solids*, 2009, **355**, 2461-2465.

300. G.-R. Li, Z.-P. Feng, Y.-N. Ou, D. Wu, R. Fu and Y.-X. Tong, *Langmuir*, 2010, **26**, 2209-2213.

301. Y. Ren, Q. Xu, J. Zhang, H. Yang, B. Wang, D. Yang, J. Hu and Z. Liu, *ACS Appl. Mater. Interfaces*, 2014, **6**, 9689-9697.

302. J. Jiang, Y. Li, J. Liu, X. Huang, C. Yuan and X. W. D. Lou, *Adv. Mater.*, 2012, **24**, 5166-5180.

303. Z. Su, C. Yang, C. Xu, H. Wu, Z. Zhang, T. Liu, C. Zhang, Q. Yang, B. Li and F. Kang, *J. Mater. Chem. A*, 2013, **1**, 12432-12440.

304. P. Sen, A. De, A. D. Chowdhury, S. Bandyopadhyay, N. Agnihotri and M. Mukherjee, *Electrochim. Acta*, 2013, **108**, 265-273.

305. G. Pandey and A. Rastogi, *ECS Trans.*, 2013, **50**, 71-78.

306. F. Meng, X. Yan, Y. Zhu and P. Si, *Nanoscale Res. Lett.*, 2013, **8**, 1-8.

307. J.-G. Wang, Y. Yang, Z.-H. Huang and F. Kang, *J. Power Sources*, 2012, **204**, 236-243.

308. R. I. Jafri, A. K. Mishra and S. Ramaprabhu, *J. Mater. Chem.*, 2011, **21**, 17601-17605.

309. J. Han, L. Li, P. Fang and R. Guo, *J. Phys. Chem. C*, 2012, **116**, 15900-15907.

310. H. Jiang, J. Ma and C. Li, *J. Mater. Chem.*, 2012, **22**, 16939-16942.

311. R. Liu, J. Duay and S. B. Lee, *ACS Nano*, 2011, **5**, 5608-5619.

312. P. Tang, Y. Zhao and C. Xu, *Electrochim. Acta*, 2013, **89**, 300-309.

313. P. Tang, L. Han, L. Zhang, S. Wang, W. Feng, G. Xu and L. Zhang, *ChemElectroChem*, 2015, **2**, 949-957.

314. R. Sharma, A. Rastogi and S. Desu, *Electrochim. Acta*, 2008, **53**, 7690-7695.

315. Y. Huang, Y. Huang, W. Meng, M. Zhu, H. Xue, C.-S. Lee and C. Zhi, *ACS Appl. Mater. Interfaces*, 2015, **7**, 2569-2574.

316. A. Q. Zhang, Y. H. Xiao, L. Z. Lu, L. Z. Wang and F. Li, *J. Appl. Polym. Sci.*, 2013, **128**,

1327-1331.

317. J. Kim, H. Ju, A. I. Inamdar, Y. Jo, J. Han, H. Kim and H. Im, *Energy*, 2014, **70**, 473-477.

318. X. Lang, A. Hirata, T. Fujita and M. Chen, *Nat. Nanotechnol.*, 2011, **6**, 232-236.

319. W. Yan, J. Y. Kim, W. Xing, K. C. Donavan, T. Ayvazian and R. M. Penner, *Chem. Mater.*, 2012, **24**, 2382-2390.

320. Y. Gao, H. Jin, Q. Lin, X. Li, M. M. Tavakoli, S.-F. Leung, W. M. Tang, L. Zhou, H. L. W. Chan and Z. Fan, *J. Mater. Chem. A*, 2015, **3**, 10199-10204.

321. T. Qiu, B. Luo, M. Giersig, E. M. Akinoglu, L. Hao, X. Wang, L. Shi, M. Jin and L. Zhi, *Small*, 2014, **10**, 4136-4141.

322. Y. Li, H. Fu, Y. Zhang, Z. Wang and X. Li, *J. Phys. Chem. C*, 2014, **118**, 6604-6611.

323. S. Hassan, M. Suzuki and A. A. El-Moneim, *American Journal of Materials Science*, 2012, **2**, 11-14.

324. D. Liu, Q. Wang, L. Qiao, F. Li, D. Wang, Z. Yang and D. He, *J. Mater. Chem.*, 2012, **22**, 483-487.

325. H. Pang, S. Wang, G. Li, Y. Ma, J. Li, X. Li, L. Zhang, J. Zhang and H. Zheng, *J. Mater. Chem. A*, 2013, **1**, 5053-5060.

326. Q. Li, Z.-L. Wang, G.-R. Li, R. Guo, L.-X. Ding and Y.-X. Tong, *Nano Lett.*, 2012, **12**, 3803-3807.

327. Z. Su, C. Yang, B. Xie, Z. Lin, Z. Zhang, J. Liu, B. Li, F. Kang and C. P. Wong, *Energy Environ. Sci.*, 2014, **7**, 2652-2659.

328. D. P. Dubal, J. G. Kim, Y. Kim, R. Holze and W. B. Kim, *Energy Technology*, 2013, **1**, 125-130.

329. M.-J. Deng, P.-J. Ho, C.-Z. Song, S.-A. Chen, J.-F. Lee, J.-M. Chen and K.-T. Lu, *Energy Environ. Sci.*, 2013, **6**, 2178-2185.

330. D. Yan, Z. Guo, G. Zhu, H. Yang, R. Wei, H. Xu and A. Yu, *Mater. Lett.*, 2012, **82**, 156-158.

331. T. Zhu, S. Zheng, Y. Chen, J. Luo, H. Guo and Y. Chen, *J. Mater. Sci.*, 2014, **49**, 6118-6126.

332. M.-J. Deng, J.-K. Chang, C.-C. Wang, K.-W. Chen, C.-M. Lin, M.-T. Tang, J.-M. Chen and K.-T. Lu, *Energy Environ. Sci.*, 2011, **4**, 3942-3946.

333. D. Yan, Z. Guo, G. Zhu, Z. Yu, H. Xu and A. Yu, *J. Power Sources*, 2012, **199**, 409-412.

334. M. Kundu and L. Liu, *J. Power Sources*, 2013, **243**, 676-681.

335. M. Huang, X. L. Zhao, F. Li, L. L. Zhang and Y. X. Zhang, *J. Power Sources*, 2015, **277**, 36-43.

336. J. Liu, J. Jiang, C. Cheng, H. Li, J. Zhang, H. Gong and H. J. Fan, *Adv. Mater.*, 2011, **23**, 2076-2081.

337. D. Kong, J. Luo, Y. Wang, W. Ren, T. Yu, Y. Luo, Y. Yang and C. Cheng, *Adv. Funct. Mater.*, 2014, **24**, 3815-3826.

338. M. Huang, Y. Zhang, F. Li, L. Zhang, Z. Wen and Q. Liu, *J. Power Sources*, 2014, **252**, 98-106.

339. C. Yuan, H. Lin, H. Lu, E. Xing, Y. Zhang and B. Xie, *RSC Adv.*, 2014, **4**, 64675-64682.

340. W. Song, G. Shao, G. Wang, Z. Ma, S. Liu, J. Song and C. Wang, *J. Solid State Electrochem.*, 2014, **18**, 3173-3180.

341. E.-H. Liu, W. Li, J. Li, X.-Y. Meng, R. Ding and S.-T. Tan, *Mater. Res. Bull.*, 2009, **44**, 1122-1126.

342. H. Chen, S. Zhou and L. Wu, *ACS Appl. Mater. Interfaces*, 2014, **6**, 8621-8630.

343.   J. Liu, J. Jiang, M. Bosman and H. J. Fan, *J. Mater. Chem.*, 2012, **22**, 2419-2426.

344.   H. Jiang, C. Li, T. Sun and J. Ma, *Chem. Commun.*, 2012, **48**, 2606-2608.

345.   H. Chen, L. Hu, Y. Yan, R. Che, M. Chen and L. Wu, *Adv. Energy Mater.*, 2013, **3**, 1636-1646.

346.   T. Leshuk, R. Parviz, P. Everett, H. Krishnakumar, R. A. Varin and F. Gu, *ACS Appl. Mater. Interfaces*, 2013, **5**, 1892-1895.

347.   G. Wang, H. Wang, Y. Ling, Y. Tang, X. Yang, R. C. Fitzmorris, C. Wang, J. Z. Zhang and Y. Li, *Nano Lett.*, 2011, **11**, 3026-3033.

348.   H. Zhou and Y. Zhang, *J. Power Sources*, 2014, **272**, 866-879.

349.   A. Ramadoss and S. J. Kim, *Int. J. Hydrogen Energy*, 2014, **39**, 12201-12212.

350.   Y. X. Zhang, M. Kuang, X. D. Hao, Y. Liu, M. Huang, X. L. Guo, J. Yan, G. Q. Han and J. Li, *J. Power Sources*, 2014, **270**, 675-683.

351.   Y. Luo, D. Kong, J. Luo, S. Chen, D. Zhang, K. Qiu, X. Qi, H. Zhang, C. M. Li and T. Yu, *RSC Adv.*, 2013, **3**, 14413-14422.

352.   X. Lu, M. Yu, G. Wang, T. Zhai, S. Xie, Y. Ling, Y. Tong and Y. Li, *Adv. Mater.*, 2013, **25**, 267-272.

353.   X. Cao, X. Xing, N. Zhang, H. Gao, M. Zhang, Y. Shang and X. Zhang, *J. Mater. Chem. A*, 2015, **3**, 3785-3793.

354.   M. Yu, H. Sun, X. Sun, F. Lu, G. Wang, T. Hu, H. Qiu and J. Lian, *Int. J. Electrochem. Sci.*, 2013, **8**, 2313-2329.

355.   P. Yang, X. Xiao, Y. Li, Y. Ding, P. Qiang, X. Tan, W. Mai, Z. Lin, W. Wu and T. Li, *ACS Nano*, 2013, **7**, 2617-2626.

356.   W. Zilong, Z. Zhu, J. Qiu and S. Yang, *J. Mater. Chem. C*, 2014, **2**, 1331-1336.

357.   Y. Zhao and P. Jiang, *Colloids Surf. A*, 2014, **444**, 232-239.

358.   Y.-B. He, G.-R. Li, Z.-L. Wang, C.-Y. Su and Y.-X. Tong, *Energy Environ. Sci.*, 2011, **4**, 1288-1292.

359.   Q. Yang, X. Zhang, M. Zhang, Y. Gao, H. Gao, X. Liu, H. Liu, K. Wong and W. Lau, *J. Power Sources*, 2014, **272**, 654-660.

360.   M. Huang, F. Li, X. L. Zhao, D. Luo, X. Q. You, Y. X. Zhang and G. Li, *Electrochim. Acta*, 2015, **152**, 172-177.

361.   Y. X. Zhang, F. Li and M. Huang, *Mater. Lett.*, 2013, **112**, 203-206.

362.   M. Huang, Y. Zhang, F. Li, Z. Wang, N. Hu, Z. Wen and Q. Liu, *Sci. Rep.*, 2014, **4**, 4518.

363.   J. Shao, X. Zhou, Q. Liu, R. Zou, W. Li, J. Yang and J. Hu, *J. Mater. Chem. A*, 2015, **3**, 6168-6176.

364.   T. Zhu, S. Zheng, Y. Lu, Y. Chen, Y. Chen and H. Guo, *J. Solid State Electrochem.*, 2014, 1-10.

365.   J. Zhu, S. Tang, H. Xie, Y. Dai and X. Meng, *ACS Appl. Mater. Interfaces*, 2014, **6**, 17637-17646.

366.   D. Sarkar, G. G. Khan, A. K. Singh and K. Mandal, *J. Phys. Chem. C*, 2013, **117**, 15523-15531.

367.   M. Huang, X. L. Zhao, F. Li, W. Li, B. Zhang and Y. Zhang, *J. Mater. Chem. A*, 2015, 3, 12852-12857.

368.   L. Yu, G. Zhang, C. Yuan and X. W. D. Lou, *Chem. Commun.*, 2013, **49**, 137-139.

369.   K. Xu, W. Li, Q. Liu, B. Li, X. Liu, L. An, Z. Chen, R. Zou and J. Hu, *J. Mater. Chem. A*, 2014, **2**, 4795-4802.

370. G. Li, W. Li, K. Xu, R. Zou, Z. Chen and J. Hu, *J. Mater. Chem. A*, 2014, **2**, 7738-7741.

371. M. Kuang, Z. Q. Wen, X. L. Guo, S. M. Zhang and Y. X. Zhang, *J. Power Sources*, 2014, **270**, 426-433.

372. R. Zou, M. F. Yuen, Z. Zhang, J. Hu and W. Zhang, *J. Mater. Chem. A*, 2015, **3**, 1717-1723.

373. F. Bao, Z. Zhang, W. Guo and X. Liu, *Electrochim. Acta*, 2015, **157**, 31-40.

374. Q. Wang, J. Xu, X. Wang, B. Liu, X. Hou, G. Yu, P. Wang, D. Chen and G. Shen, *ChemElectroChem*, 2014, **1**, 559-564.

375. W. Ma, H. Nan, Z. Gu, B. Geng and X. Zhang, *J. Mater. Chem. A*, 2015, **3**, 5442-5448.

376. K. Qiu, Y. Lu, D. Zhang, J. Cheng, H. Yan, J. Xu, X. Liu, J.-K. Kim and Y. Luo, *Nano Energy*, 2015, **11**, 687-696.

377. L. Bao, J. Zang and X. Li, *Nano Lett.*, 2011, **11**, 1215-1220.

378. D. Guo, W. Ren, Z. Chen, M. Mao, Q. Li and T. Wang, *RSC Adv.*, 2015, **5**, 10681-10687.

379. Y. Wang, Y. Shi, C. X. Zhao, J. I. Wong, X. W. Sun and H. Y. Yang, *Nanotechnology*, 2014, **25**, 094010.

380. W. Gao, N. Singh, L. Song, Z. Liu, A. L. M. Reddy, L. Ci, R. Vajtai, Q. Zhang, B. Wei and P. M. Ajayan, *Nat. Nanotechnol.*, 2011, **6**, 496-500.

381. S. Makino, Y. Yamauchi and W. Sugimoto, *J. Power Sources*, 2013, **227**, 153-160.

382. M. F. El-Kady, V. Strong, S. Dubin and R. B. Kaner, *Science*, 2012, **335**, 1326-1330.

383. C. Meng, J. Maeng, S. W. John and P. P. Irazoqui, *Adv. Energy Mater.*, 2014, **4**, 1301269.

384. M. F. El-Kady and R. B. Kaner, *Nat. Commun.*, 2013, **4**, 1475.

385. S. Y. Hong, J. Yoon, S. W. Jin, Y. Lim, S.-J. Lee, G. Zi and J. S. Ha, *ACS Nano*, 2014, **8**, 8844-8855.

386. M. S. Kim, B. Hsia, C. Carraro and R. Maboudian, *Carbon*, 2014, **74**, 163-169.

387. J. Xu and G. Shen, *Nano Energy*, 2015, **13**, 131-139.

388. P. Xu, B. Wei, Z. Cao, J. Zheng, K. Gong, F. Li, J. Yu, Q. Li, W. Lu and J.-H. Byun, *ACS Nano*, 2015, 9, 6088-6096.

389. Y. S. Moon, D. Kim, G. Lee, S. Y. Hong, K. K. Kim, S. M. Park and J. S. Ha, *Carbon*, 2015, **81**, 29-37.

390. M. Xue, Z. Xie, L. Zhang, X. Ma, X. Wu, Y. Guo, W. Song, Z. Li and T. Cao, *Nanoscale*, 2011, **3**, 2703-2708.

391. C. Shen, X. Wang, S. Li, W. Zhang and F. Kang, *J. Power Sources*, 2013, **234**, 302-309.

392. X. Wang, B. D. Myers, J. Yan, G. Shekhawat, V. Dravid and P. S. Lee, *Nanoscale*, 2013, **5**, 4119-4122.

393. M. F. El-Kady, M. Ihns, M. Li, J. Y. Hwang, M. F. Mousavi, L. Chaney, A. T. Lech and R. B. Kaner, *Proc. Natl. Acad. Sci. USA*, 2015, **112**, 4233-4238.

394. W. Liu, C. Lu, X. Wang, R. Y. Tay and B. K. Tay, *ACS Nano*, 2015, **9**, 1528-1542.

395. D. P. Dubal, D. Aradilla, G. Bidan, P. Gentile, T. J. Schubert, J. Wimberg, S. Sadki and P. Gomez-Romero, *Sci. Rep.*, 2015, **5**, 9771.

Fig. 1. Ragone plot of specific power versus specific energy for various electrochemical energy storage systems. Reproduced with permission from ref. 1. Copyright 2008, Nature Publishing Group.
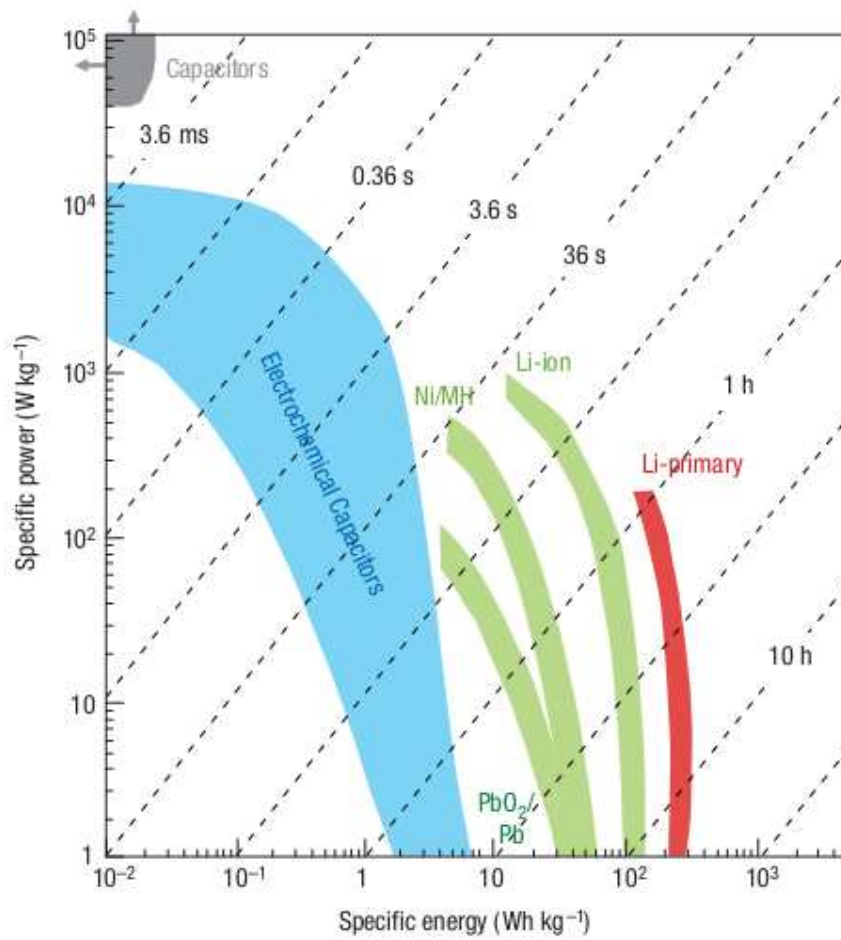
Fig. 2. Schematic of two different charge storage mechanisms via (a) electrochemical double-layer capacitance (EDLC) or (b) redox reactions based pseudocapacitance. Reproduced with permission from ref. 18. Copyright 2011, Materials Research Society.
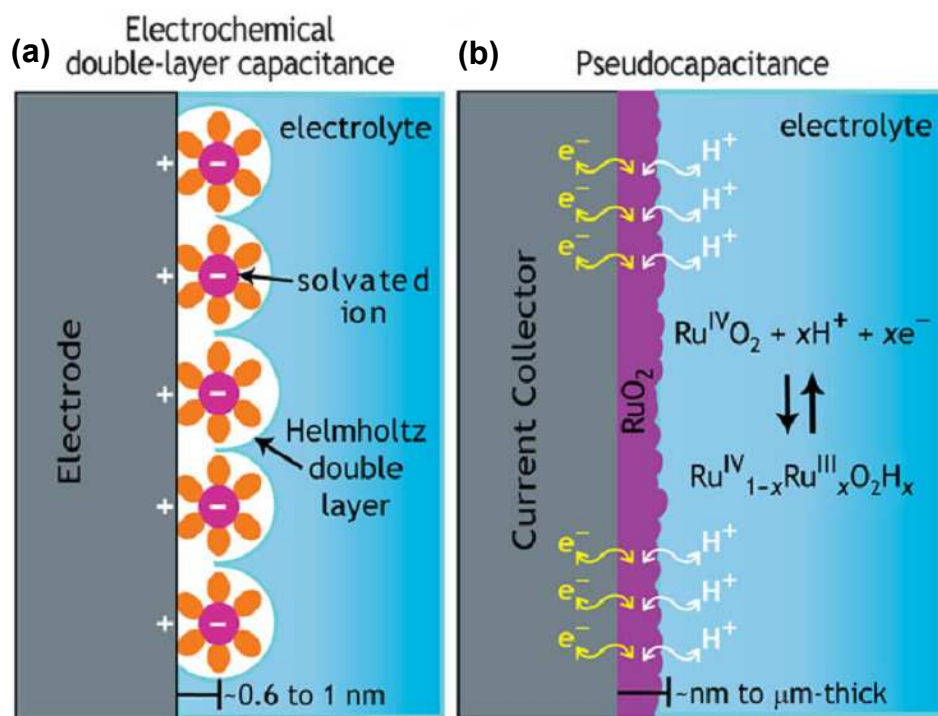
Fig. 3. Crystal structures of α-, β-, γ-, δ-, and λ-MnO₂. Reproduced with permission from ref. 106. Copyright 2008, American Chemical Society.

(α)

(β)

(γ)

(δ)

(λ)
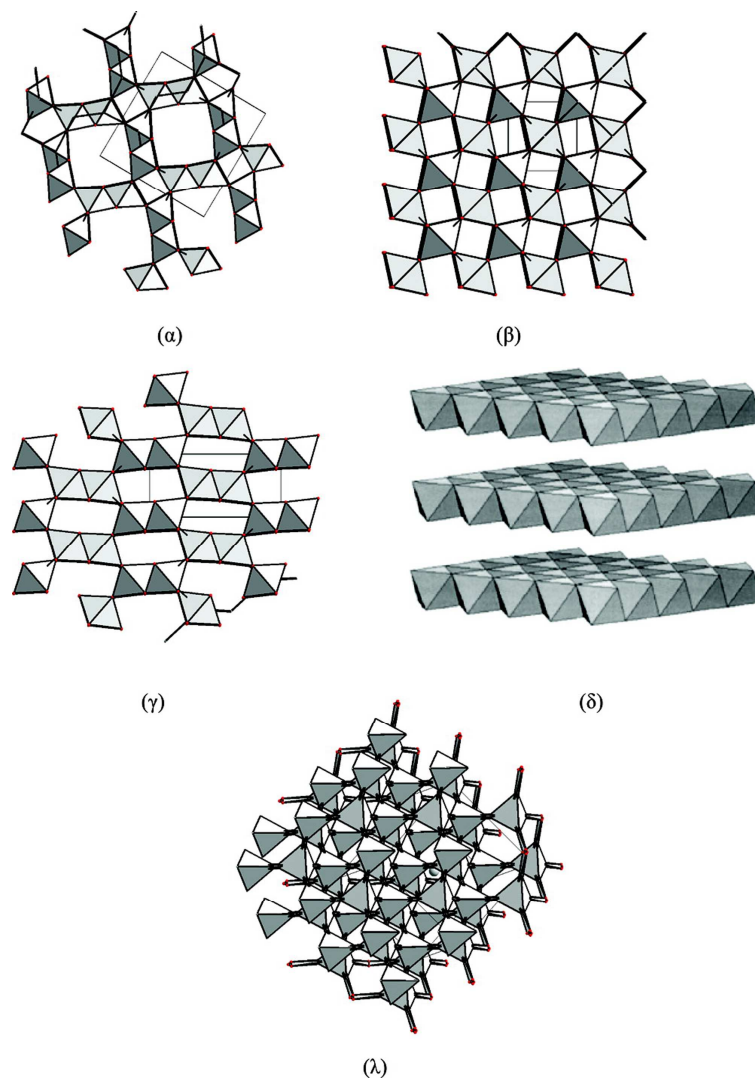
Fig. 4. SEM images of diatomite structures with different morphologies (a, d, and g) and the corresponding hierarchical hollow MnO$_2$ patterns by replica molding from diatomites. Reproduced with permission from ref. 153. Copyright 2015, The Royal Society and Chemistry.
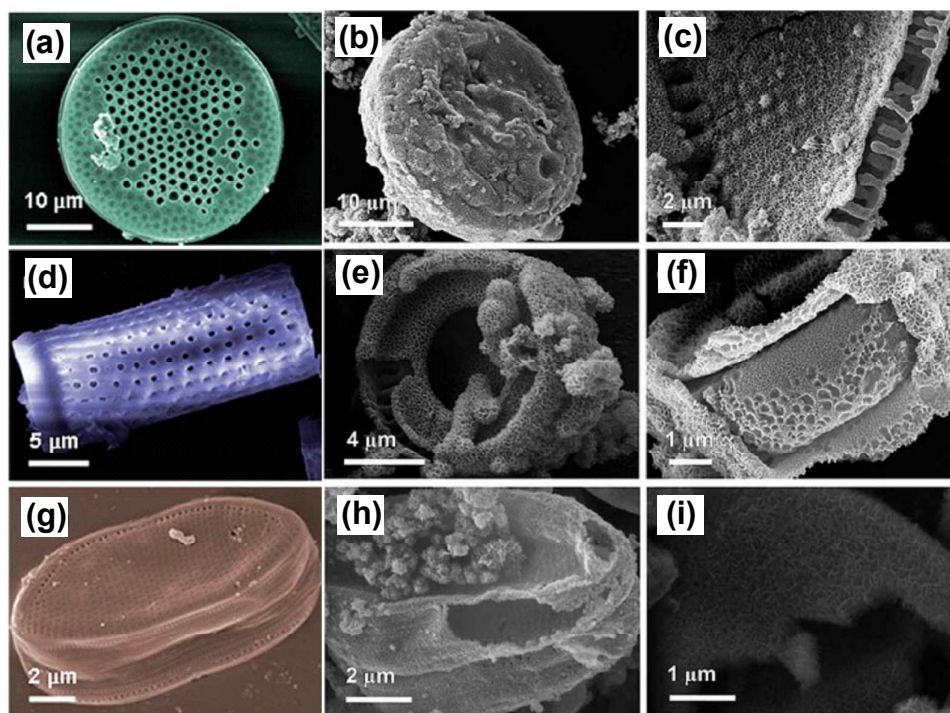
Fig.5. MnO$_2$ nanotubes and nanowires arrays made from AAO templates: (a, b) AAO template and MnO$_2$ nanotubes arrays. Reproduced with permission from ref. 155. Copyright 2014, AIP Publishing LLC. (c, d) MnO$_2$ nanowires arrays. Reproduced with permission from ref. 158 Copyright 2010, Elsevier B.V.
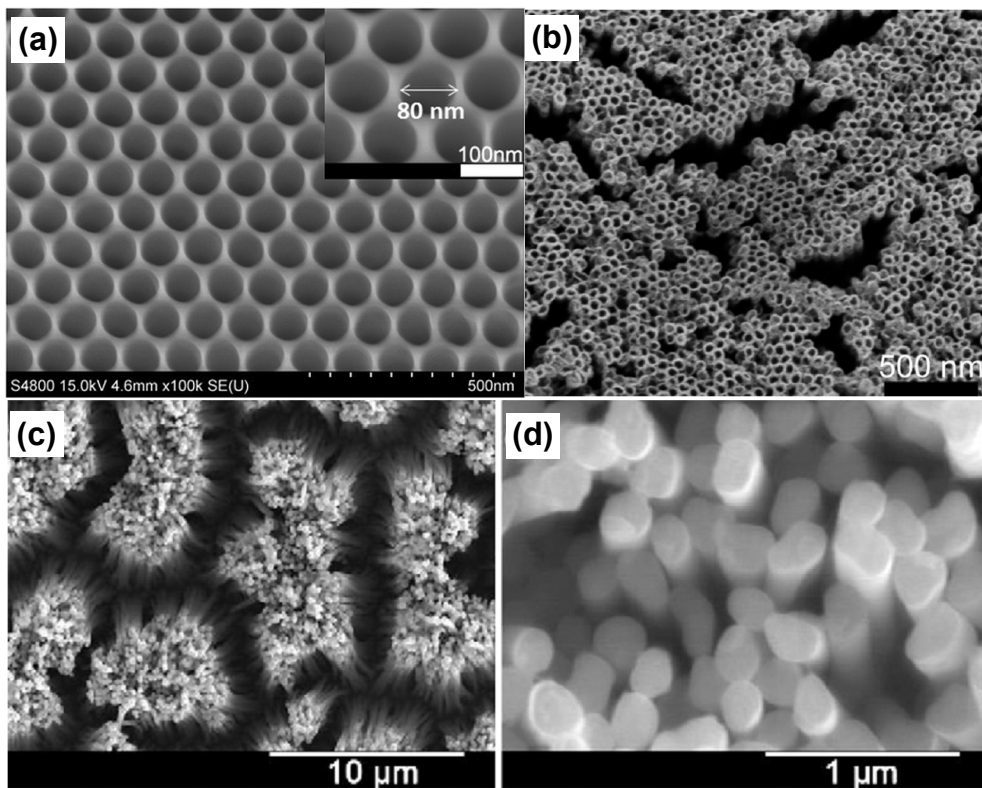
Fig. 6. (a) Schematic illustration of the procedure to synthesize porous MnO_2 nanotubes. SEM images of MnO_2 nanotubes. (b) Detailed images of the MnO_2 nanotubes. (c) Side-view of MnO_2 nanotubes arrays. (d) Enlarged view of the MnO_2 nanotubes arrays. (e) The energy density vs. power density of the MnO_2 nanotubes//AG asymmetric supercapacitor in a Ragone plot for fuel cells, conventional batteries, conventional capacitors, and ultracapacitors. (f) Digital image of a red-light-emitting diode (LED) lighted by the MnO_2 nanotubes//AG device. Reproduced with permission from ref. 87. Copyright 2014, Nature Publishing Group.
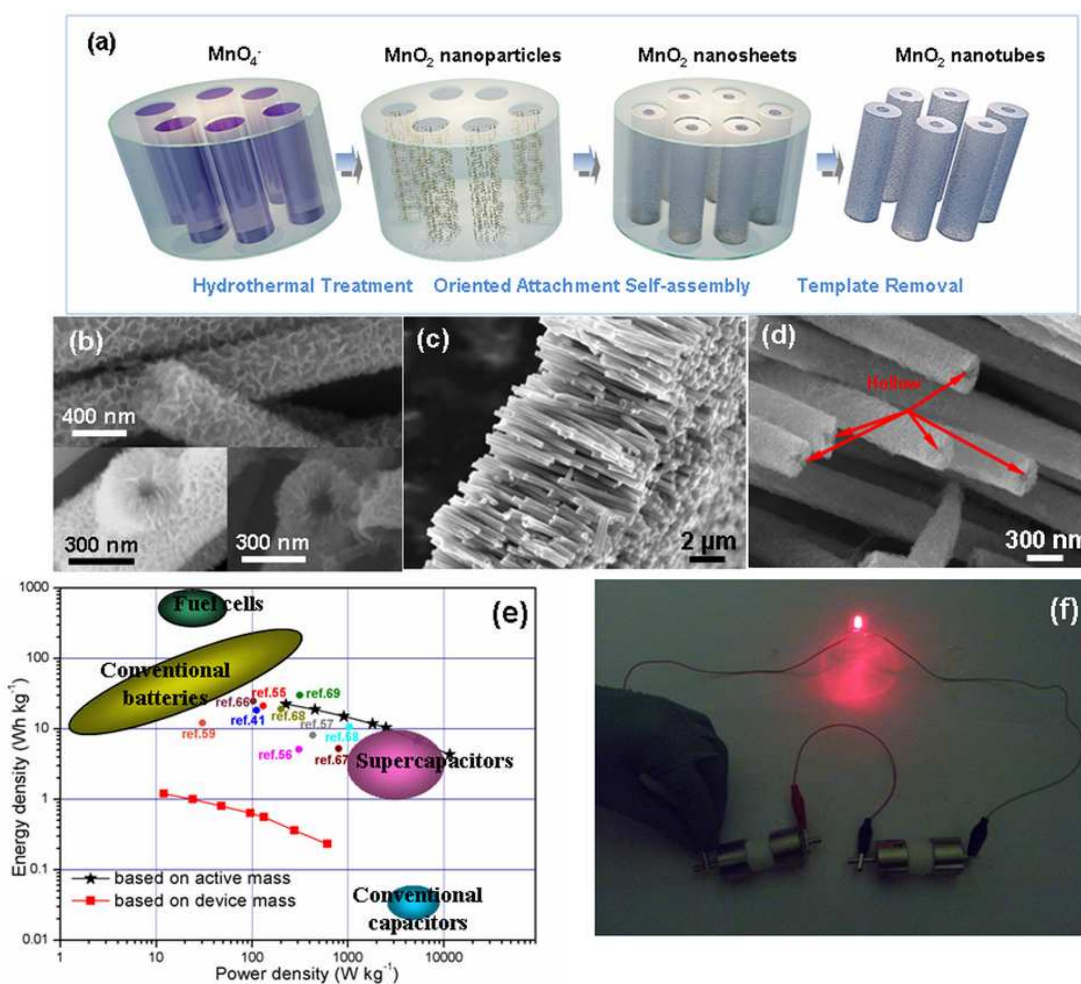
Fig. 7. (a-d) SEM images with different magnifications of the obtained β-MnO$_2$ network. (e, f) HRTEM images of the obtained β-MnO$_2$ network. Reproduced with permission from ref. 219. Copyright 2013, Nature Publishing Group.
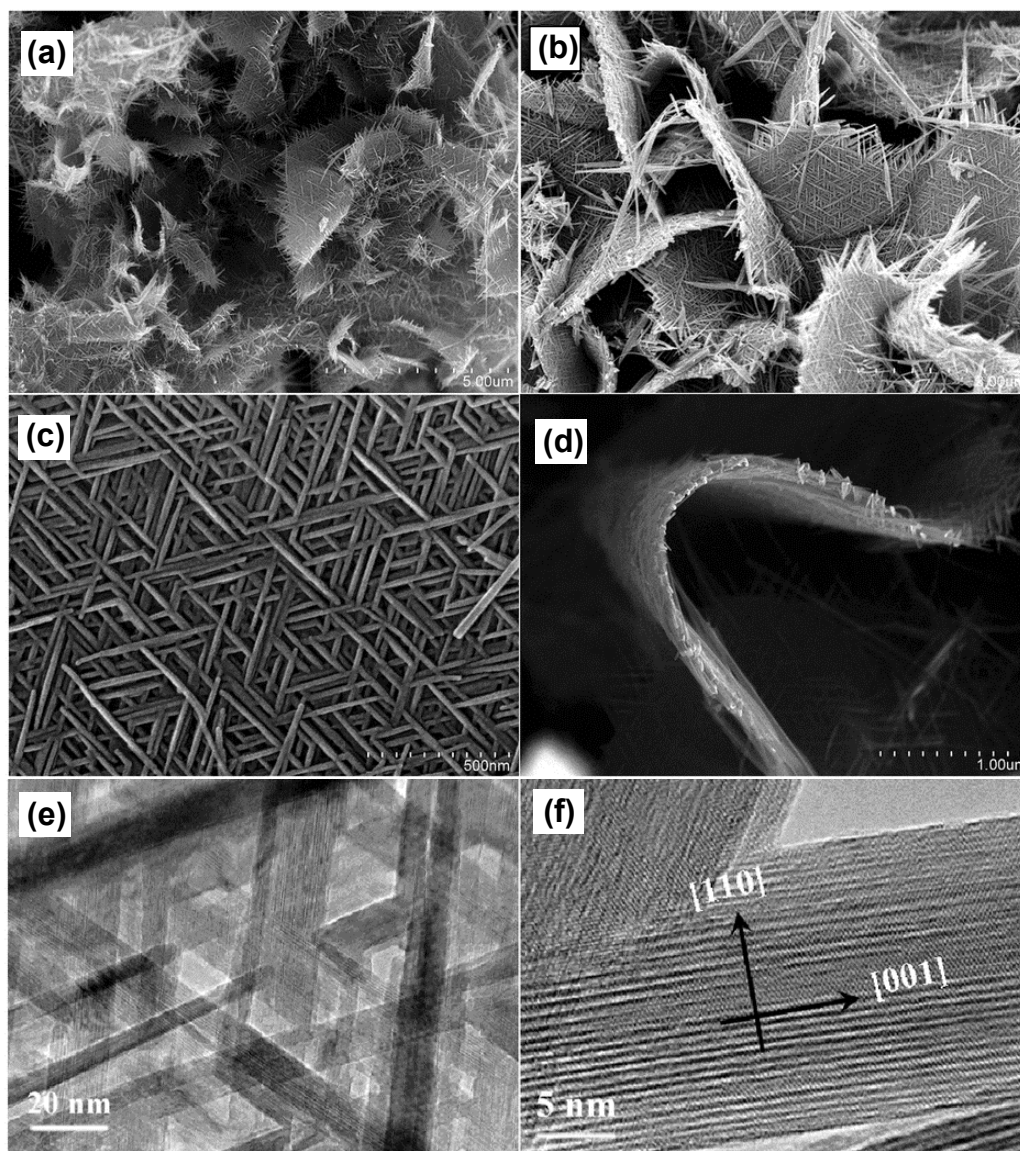
Fig. 8. (a-c) SEM images of hollow Ni dendrites. (d-f) hollow Ni dendrite-supported MnO$_2$ nanowires (Ni@MnO$_2$) grown on Ni foil. The corresponding insets are low-magnification images. (h-i) Elec trochemical measurements of Ni@MnO$_2$ structures prepared on Ni foils. Reproduced with permission from ref. 250. Copyright 2013, The Royal Society and Chemistry.
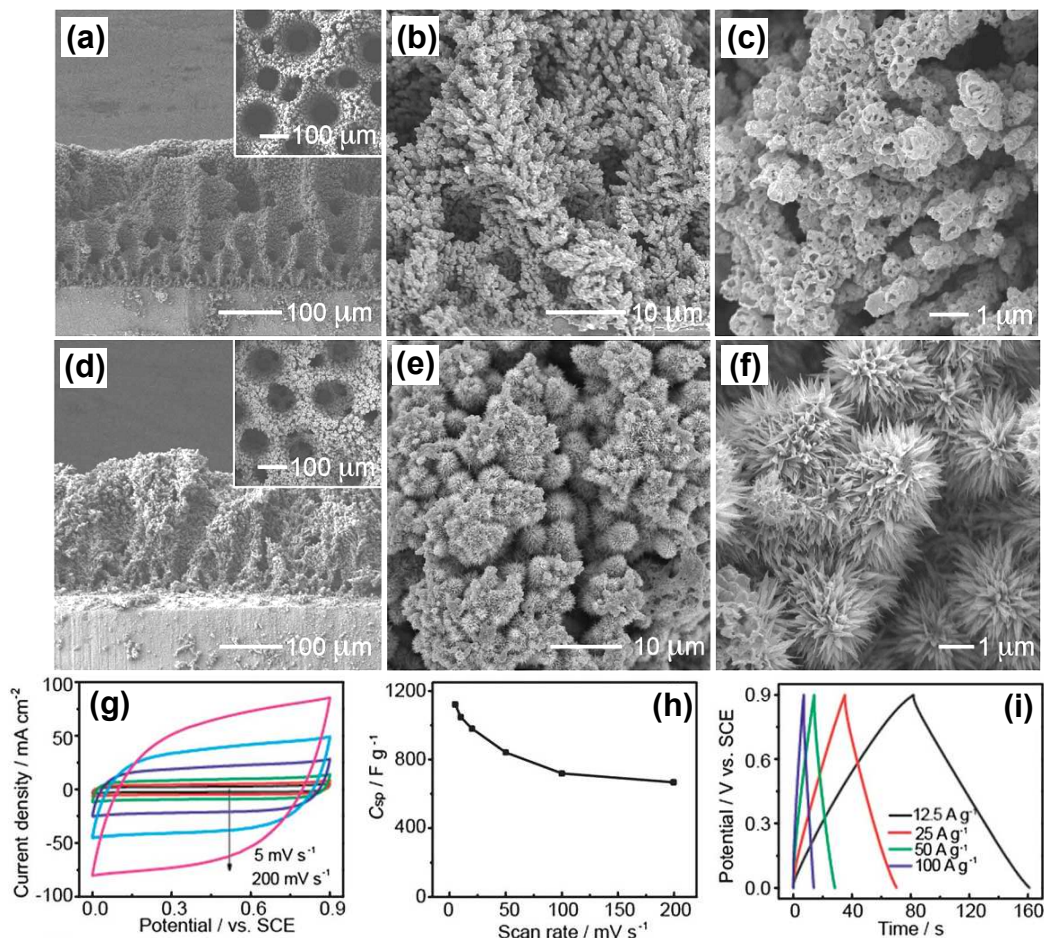
Fig. 9. (a, b) SEM images of CNTs@MnO$_2$ core–shell nanostructures grown on Ni foam. Insets show the corresponding local 3D structures in low magnifications. (c, d) TEM and HRTEM image of a partial coverage of the MnO$_2$ nanosheets on the surface of CNTs. (e, f) Electrochemical properties of the as-prepared CNTs@MnO$_2$ core-shell nanocomposite electrode. Reproduced with permission from ref. 264. Copyright 2014, Elsevier B.V.
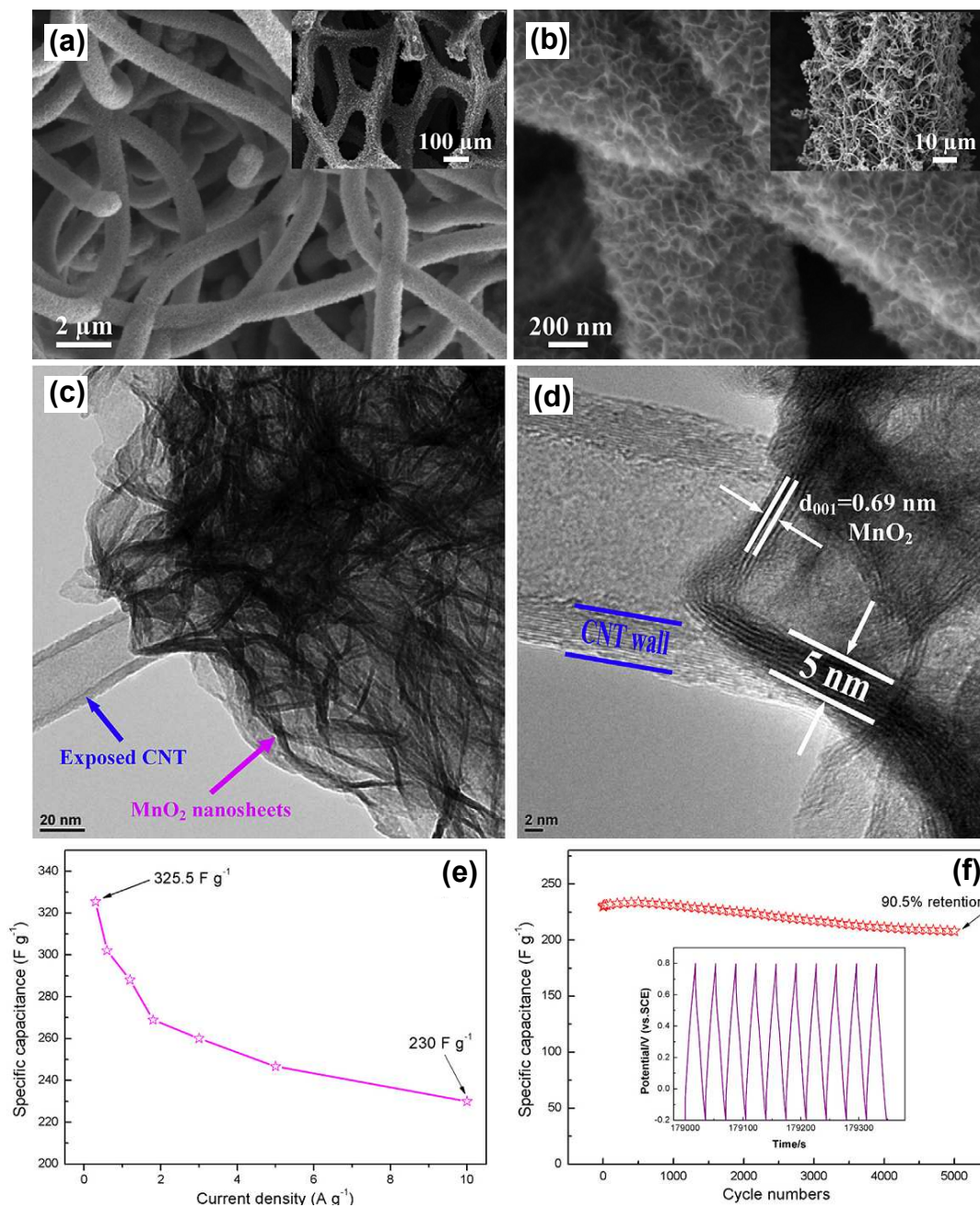
Fig. 10. SEM images of MnO₂-graphene composites with different structures. (a) Graphene nanoshees/MnO₂. Reproduced with permission from ref. 268. Copyright 2010, American Chemical Society. (b) Graphene nanoribbons/MnO₂. Reproduced with permission from ref. 277. Copyright 2014, The Royal Society and Chemistry. (c) Partial-exfoliated graphite/MnO₂. Reproduced with permission from ref. 279. Copyright 2015, The Royal Society and Chemistry. (d) 3D graphene hydrogel/MnO₂. Reproduced with permission from ref. 193. Copyright 2015, The Royal Society and Chemistry.
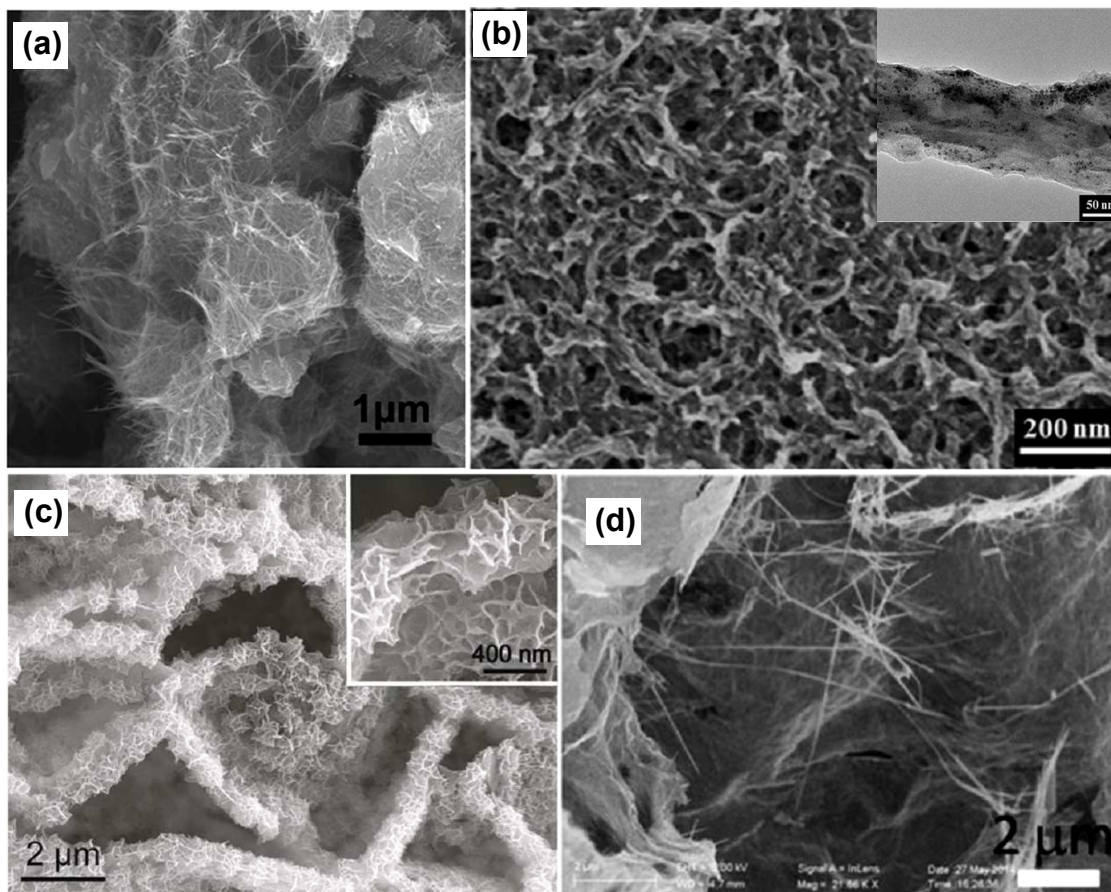
Fig. 11. (a, b) SEM image of 3D graphene networks and 3D graphene/MnO$_2$ composite networks Inset shows high-magnification SEM image. (c) Schematic of the flexible supercapacitors. The two digital photographs show the flexible supercapacitors when bended. (d) Ragone plots of the flexible supercapacitor, compared with the values of similar symmetrical systems from other references. Reproduced with permission from ref. 282. Copyright 2012, American Chemical Society.
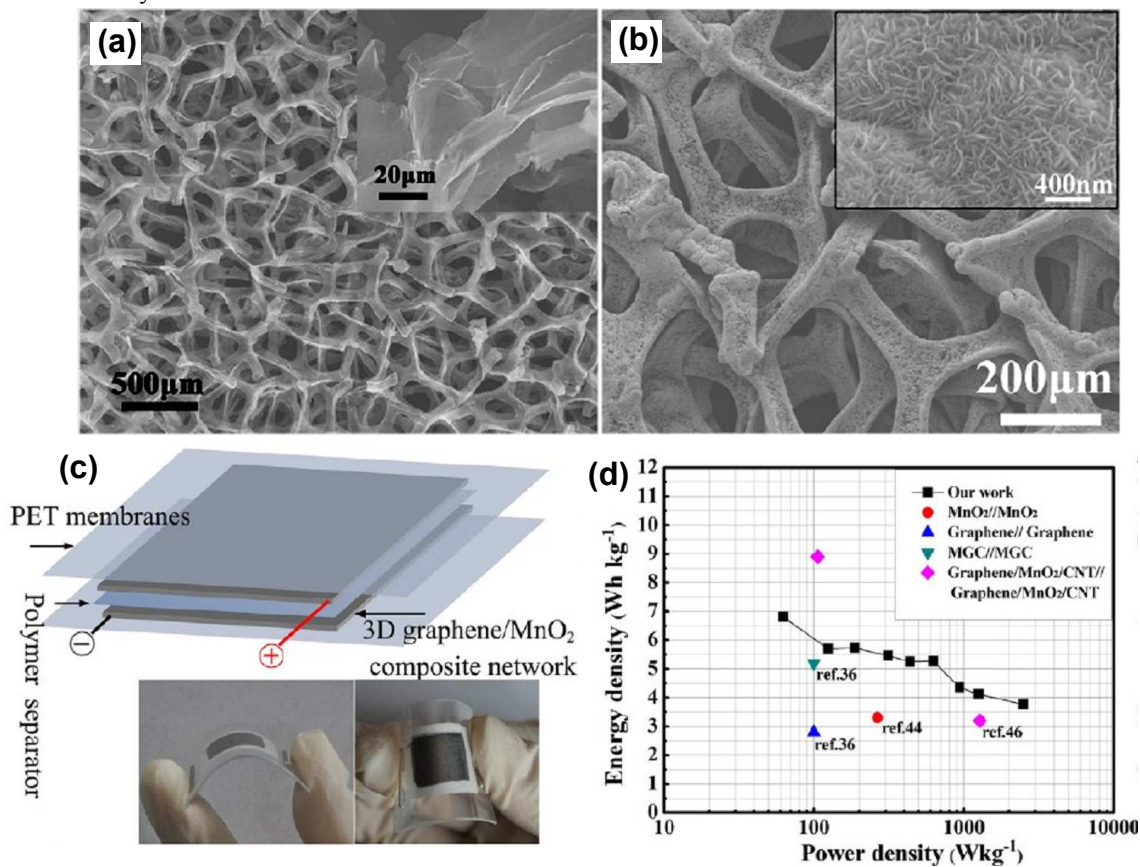
Fig. 12. (a) SEM image of 3D porous carbon. (b-d) SEM images of MnO$_2$/3D porous carbon hybrid structure after MnO$_2$ deposition. (f) Specific capacitance vs scan rate for samples with different areal mass densities for MnO$_2$. (b) Areal capacitance of MnO$_2$/3D porous carbon hrbrid electrode vs MnO$_2$ mass loading. Reproduced with permission from ref. 289. Copyright 2014, Elsevier B.V.
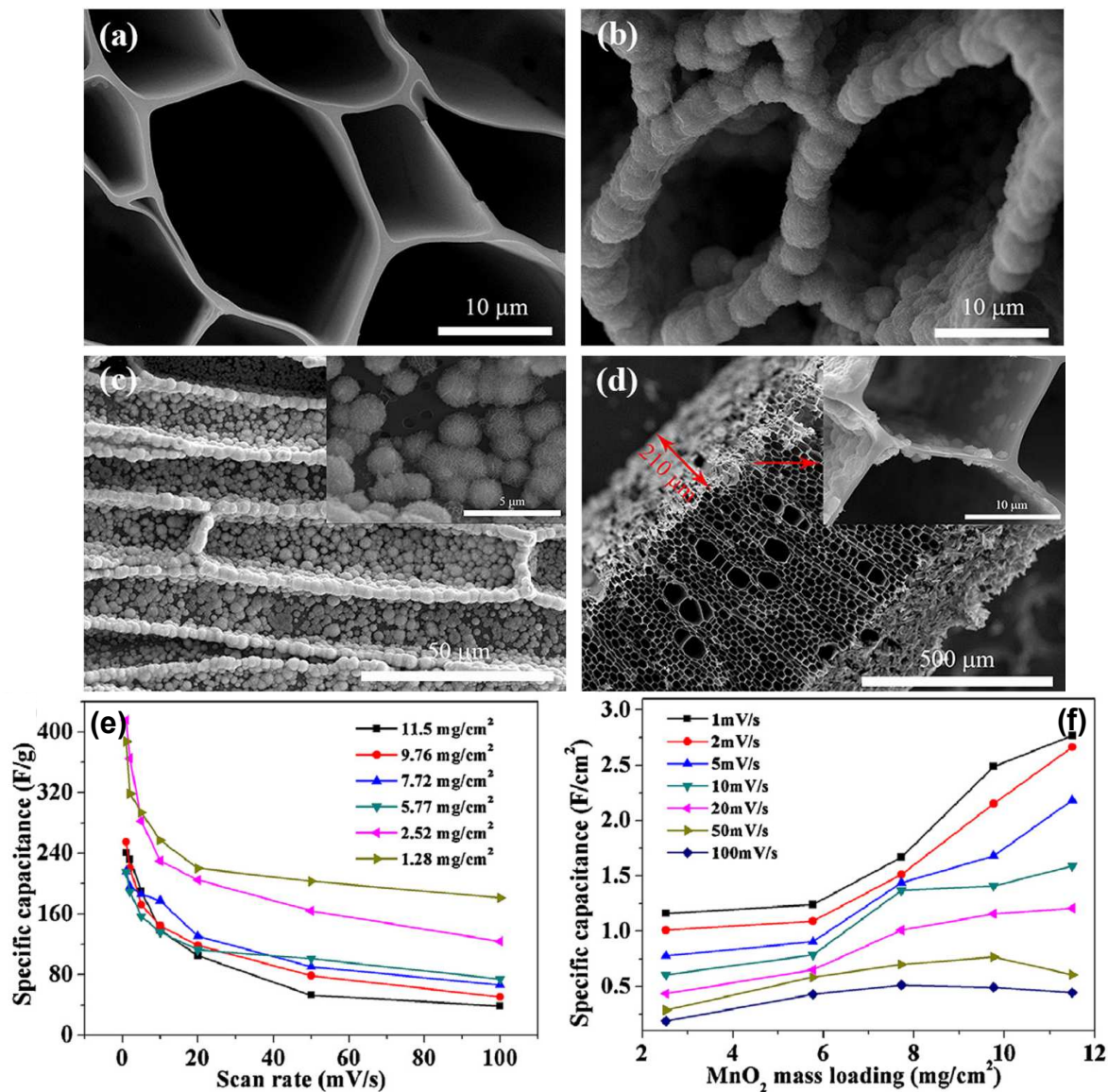
Fig. 13. (a, b) SEM images of the carbon nanofibers and carbon nanofiber@MnO$_2$ composite. (c, d) TEM images of a single carbon nanofiber@MnO$_2$ nanostructure. Reproduced with permission from ref. 292. Copyright 2012, Elsevier B.V.
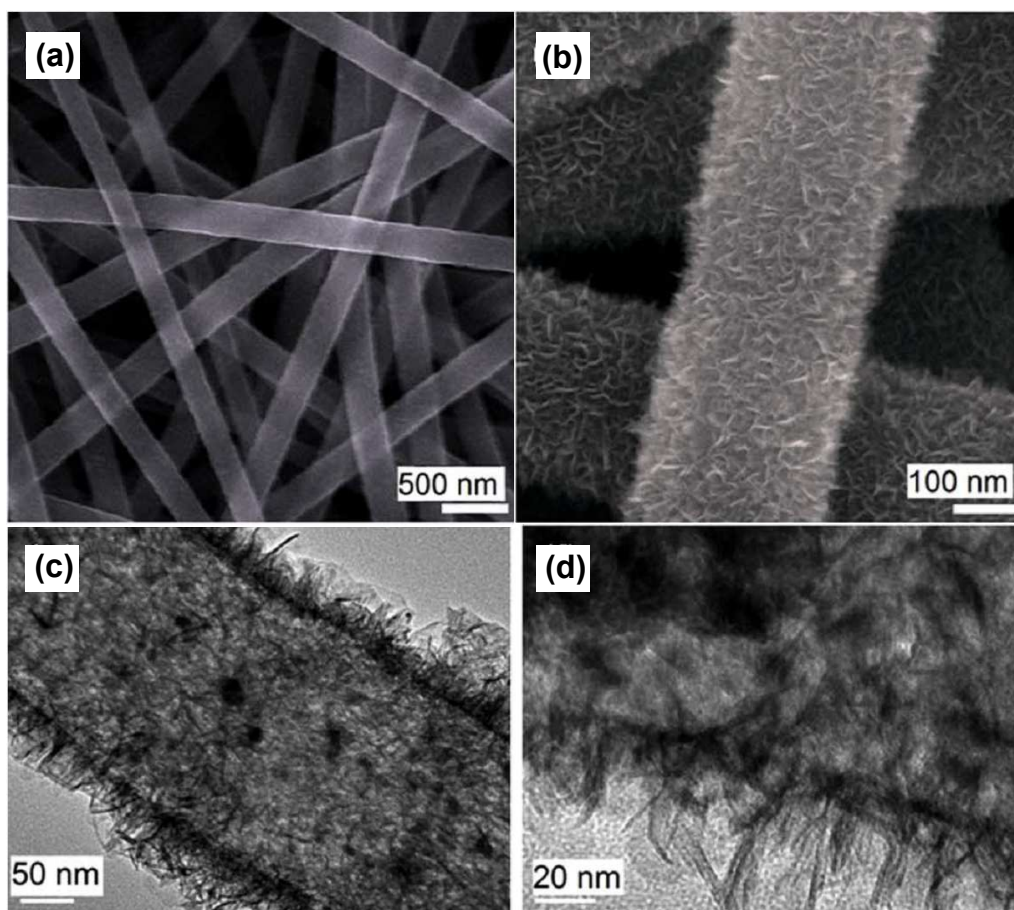
Fig. 14. (a, b) SEM images of carbon spheres and carbon sphere@MnO$_2$ core-shell composite. (c-g) TEM and corresponding EDS of the carbon sphere@MnO$_2$ core-shell composite. Reproduced with permission from ref. 295. Copyright 2014, Elsevier B.V.
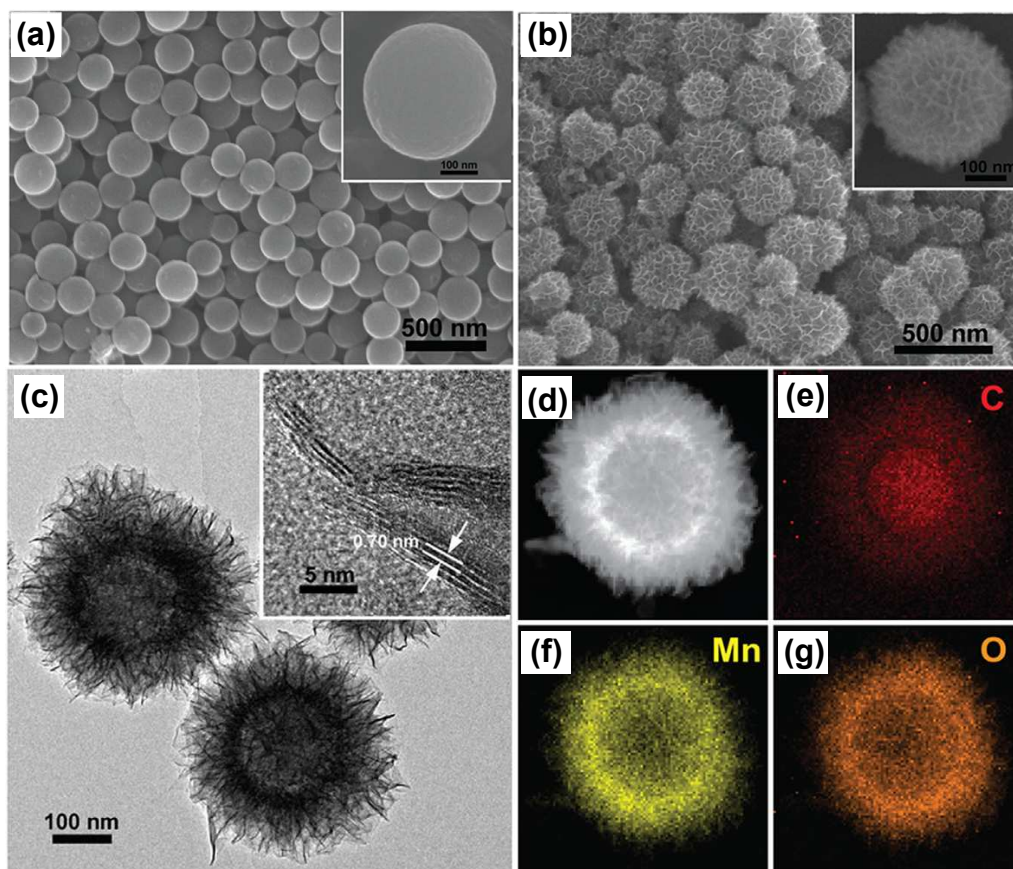
Fig. 15. (a) Schematic illustration for the formation of 1D conducting polymer−MnO_2 composites. TEM images of (b) PANI and (c, d) PANI−MnO_2 composites. (e) SAED pattern, and EDS maps of (f) Mn and (g) O from a single composite nanofiber. Scale bars: (b, c) 100 nm; (d, f, g) 20 nm. (h, i) Electrochemical properties of the PANI-MnO_2 composite electrode. Reproduced with permission from ref. 309. Copyright 2012, American Chemical Society.
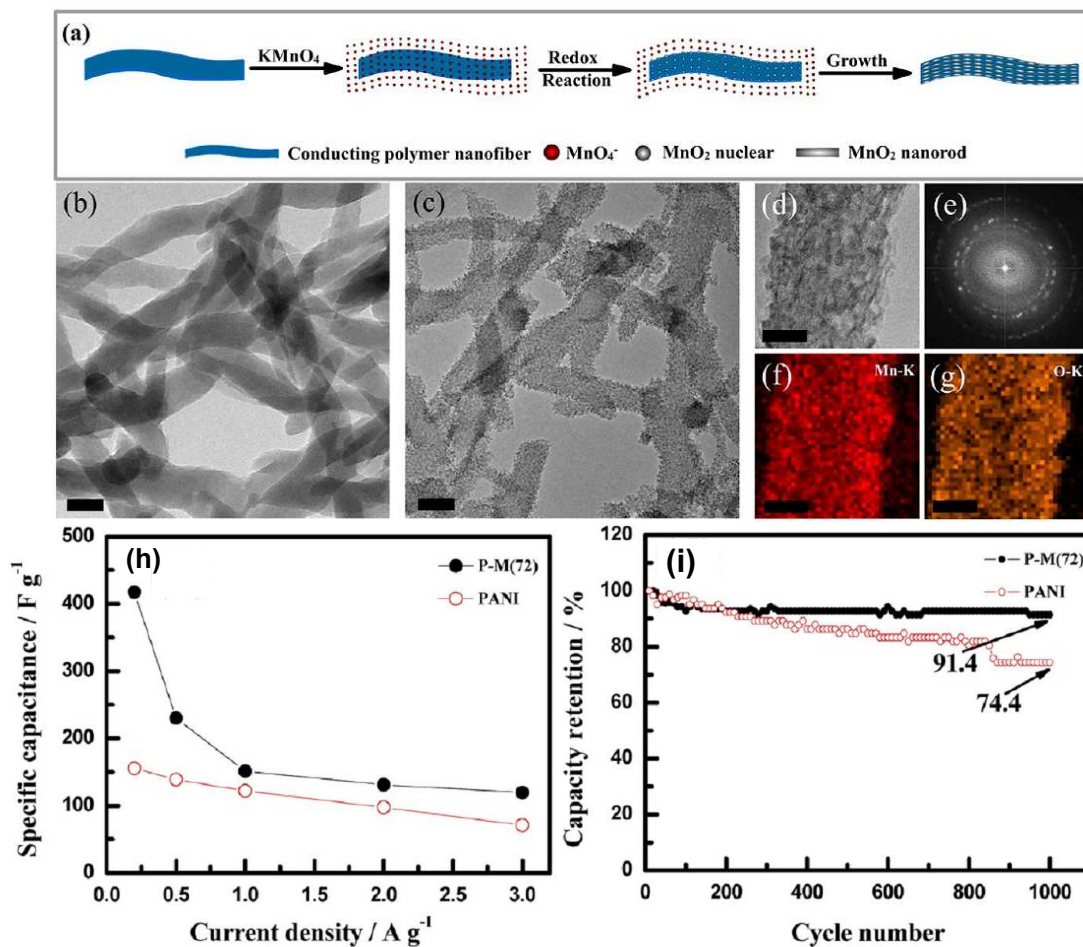
Fig. 16. (a) Schematic showing the fabrication process for nanoporous gold/MnO$_2$ hybrid materials by directly growing MnO$_2$ (orange) onto nanoporous gold. (b) Photograph of a nanoporous gold/MnO$_2$-based supercapacitor. (c) SEM image of as de-alloyed nanoporous gold films. (d) SEM image of a nanoporous gold/MnO$_2$ film with a MnO$_2$ plating time of 10 min. (e) Bright-field TEM image of the nanoporous gold/MnO$_2$ hybrid with a MnO$_2$ plating time of 20 min. (f, g) Electrochemical properties of the Au/MnO$_2$ composite electrode. Reproduced with permission from ref. 318. Copyright 2011, Nature Publishing Group.
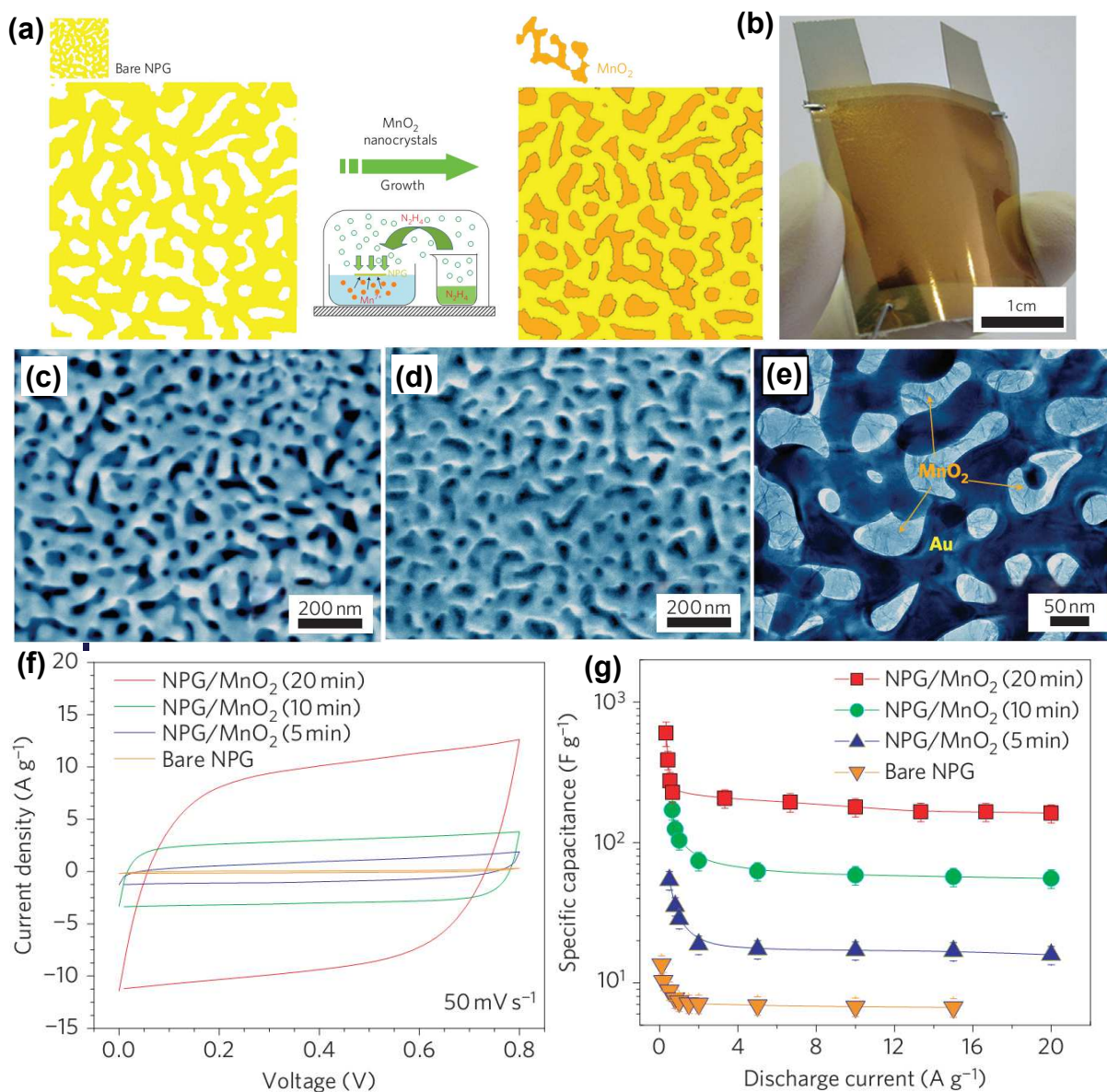
Fig. 17. (a) Photographs of the free-standing Au nanospikes film transferred onto a regular Xerox printing paper and the SEM image (insert) shows the microstructure upon bending. (b) Top-view SEM image of the as-prepared $MnO_2/Au/MnO_2$ nanospike electrode. (c) CV measurements when the device is folded and released. Reproduced with permission from ref. 320. Copyright 2015, The Royal Society and Chemistry. (d, e) SEM image of the Au nanomesh and Au@δ-MnO_2 core–shell nanomesh peeled from PET substrate. Inset shows the optical image of a transparent flexible supercapacitor. (f) Cycling stability and coulombic efficiency of the device at flat and bending state. Reproduced with permission from ref. 321. Copyright 2014, WILEY-VCH Verlag GmbH & Co. KGaA, Weinheim.
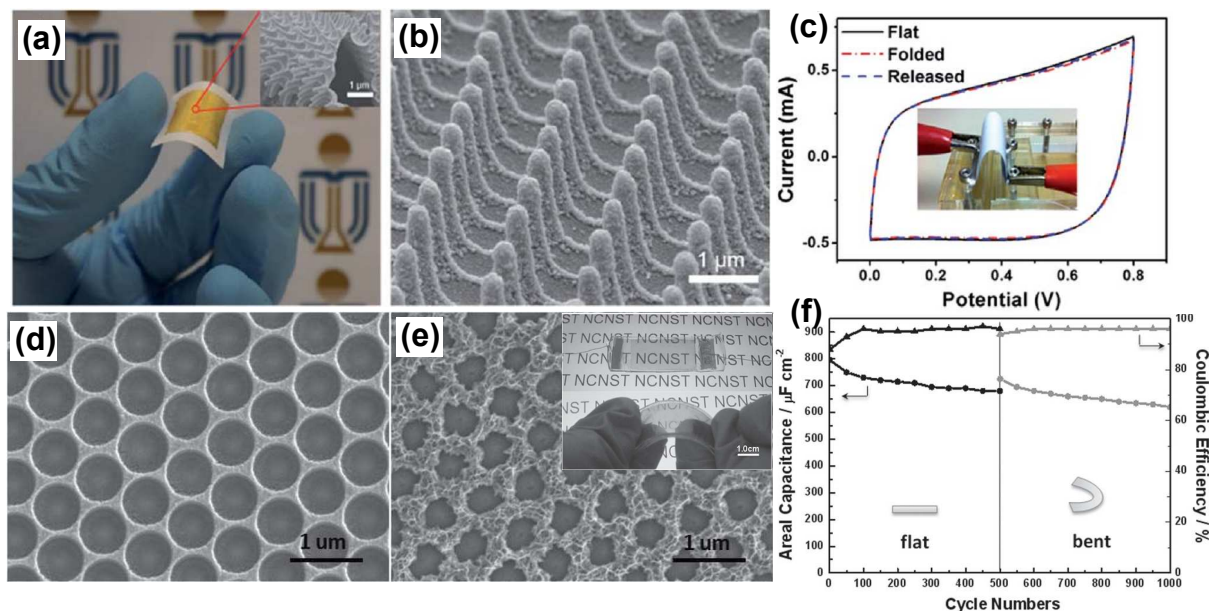
Fig. 18. (a-c) SEM images of Ni nanocones and the MnO$_2$ nanostructure deposited on Ni nanocones (MNN). (d-f) TEM images of the MnO$_2$ nanostructure deposited on Ni nanocones. Inset is the selected area electron diffraction (SAED) pattern of MnO$_2$. (g) A photographic image of the as-prepared MNN/AC ionogel supercapacitor electrode (1.3 m). (h) Photographic image of a fully packed supercapacitor device. (i) Photograph showing a MNN/AC ionogel supercapacitor driving a red LED under a bending state. (j) Energy and power densities of the MNN-based asymmetric supercapacitors compared to some available energy storage systems. Reproduced with permission from ref. 327. Copyright 2014, The Royal Society and Chemistry.
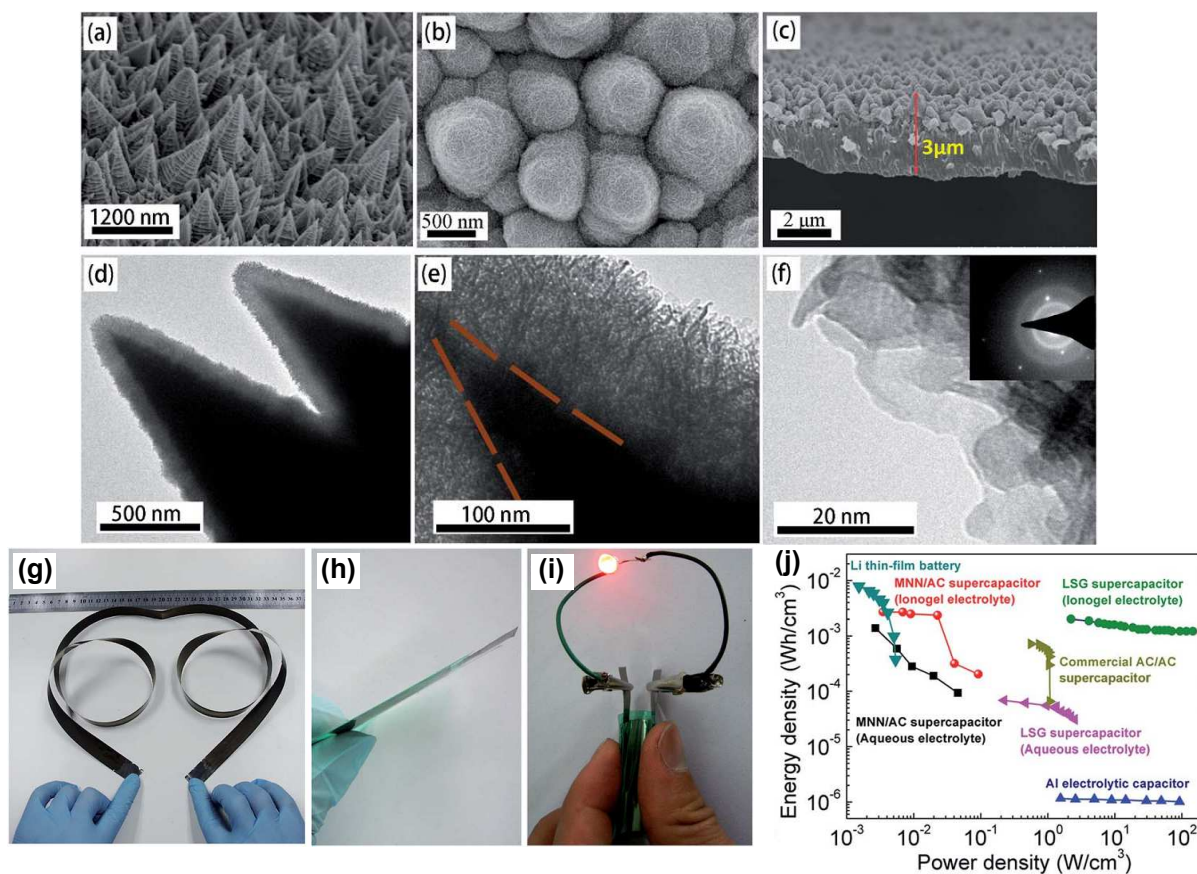
Fig. 19. (a) Scheme of preparing a high-porosity 3D ordered macroporous Mn/MnO$_2$ electrode. SEM images of (b) polystyrene opals covering the Au/ITO substrate, (c) 3D ordered macroporous Mn inverse opals structure (inset: large magnification), (c) 3D ordered macroporous Mn/MnO$_2$ electrode structure. Reproduced with permission from ref. 329. Copyright 2013, The Royal Society and Chemistry.
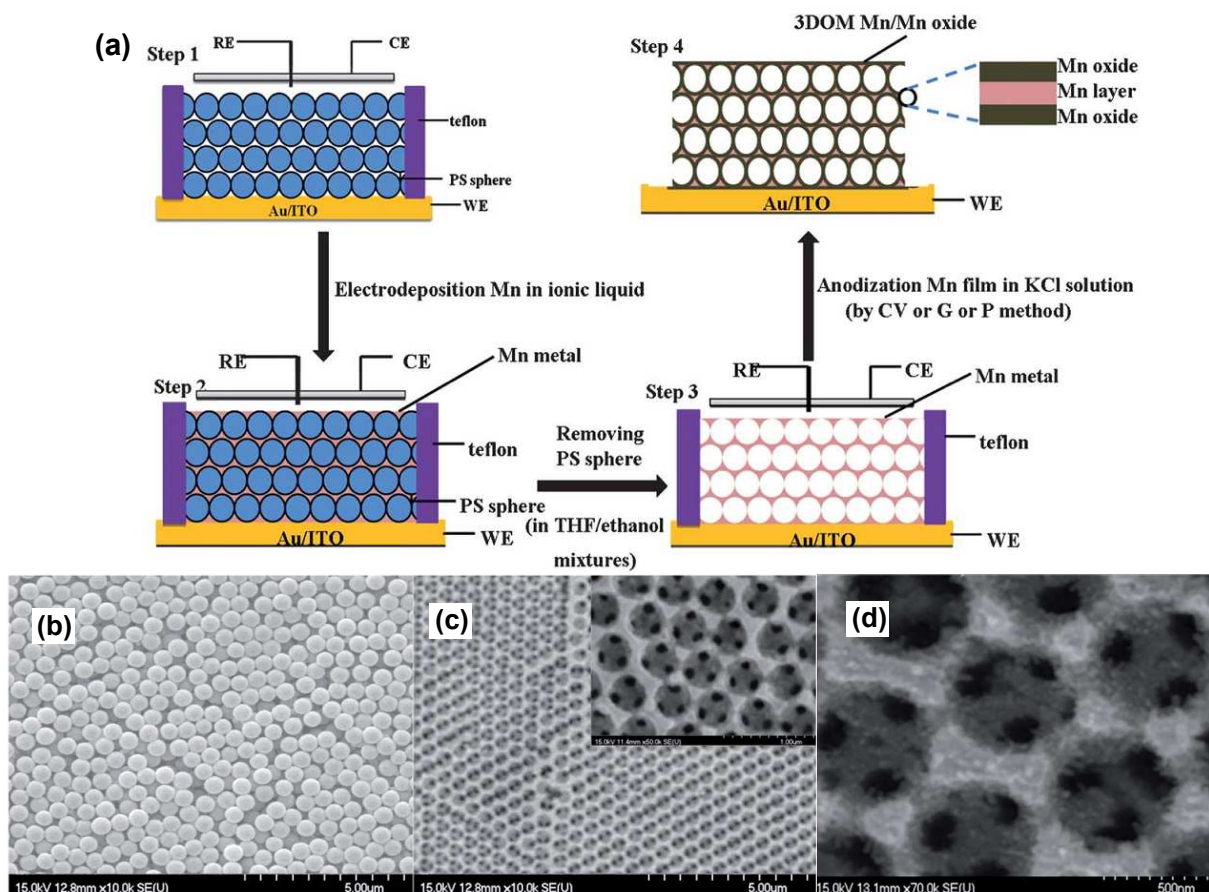
Fig. 20. SEM images of the Ni foam (a), MnO$_2$ nanosheets arrays on Ni foam (b–d) with different magnifications. The insets show the corresponding optical images of the pristine Ni foam, and MnO$_2$ nanosheets on Ni foam. (e, f) Electrochemical performance of the MnO$_2$ nanosheets arrays on Ni foam electrode. Reproduced with permission from ref. 335. Copyright 2015, Elsevier B.V.
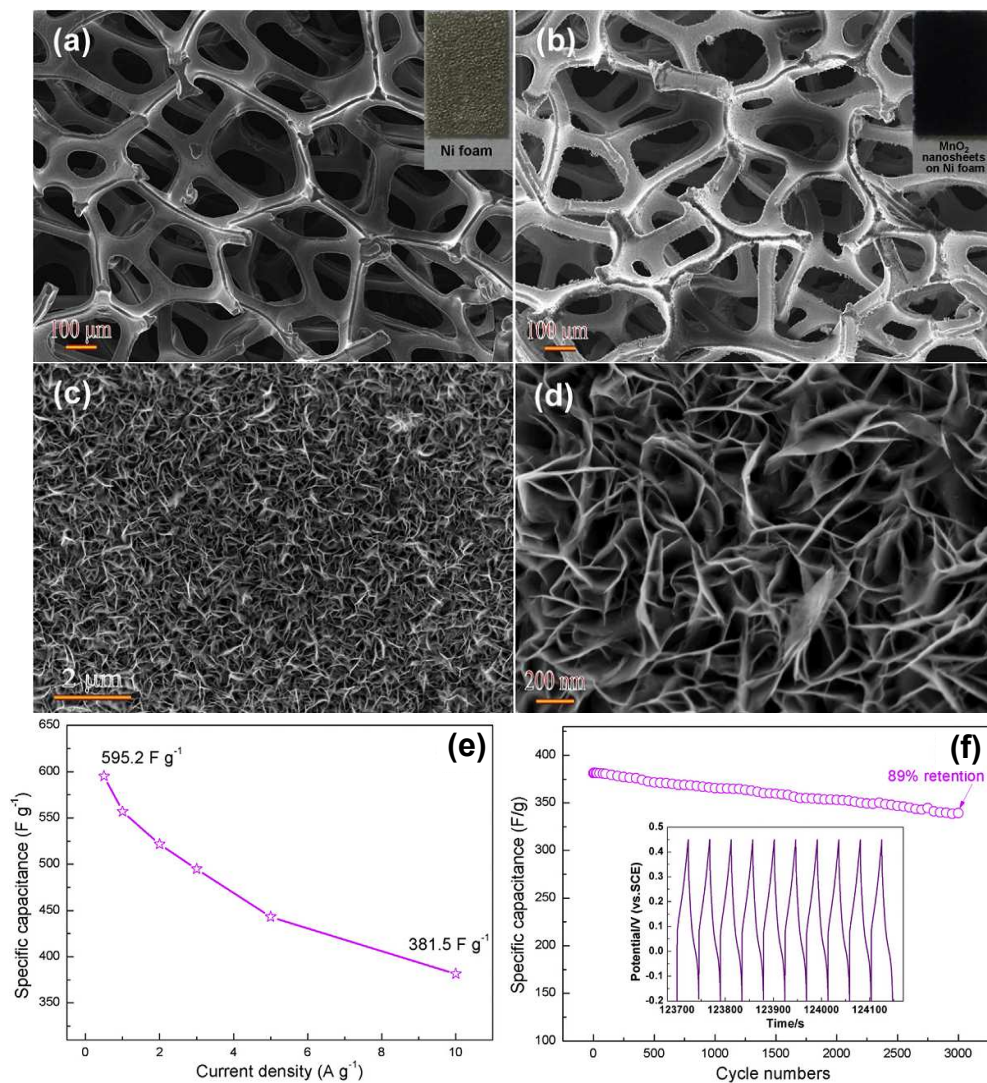
Fig. 21. (a) Schematic illustration of the two-step synthesis of hierarchical $Co_3O_4@MnO_2$ core–shell arrays directly on Ni foam. (b, c) Low-magnification and enlarged SEM images of the Co_3O_4 nanowires arrays on Ni foam. (d, e) Low-magnification and enlarged SEM images of the hierarchical $Co_3O_4@MnO_2$ core–shell nanowire arrays on Ni foam. Reproduced with permission from ref. 338. Copyright 2014, Elsevier B.V.
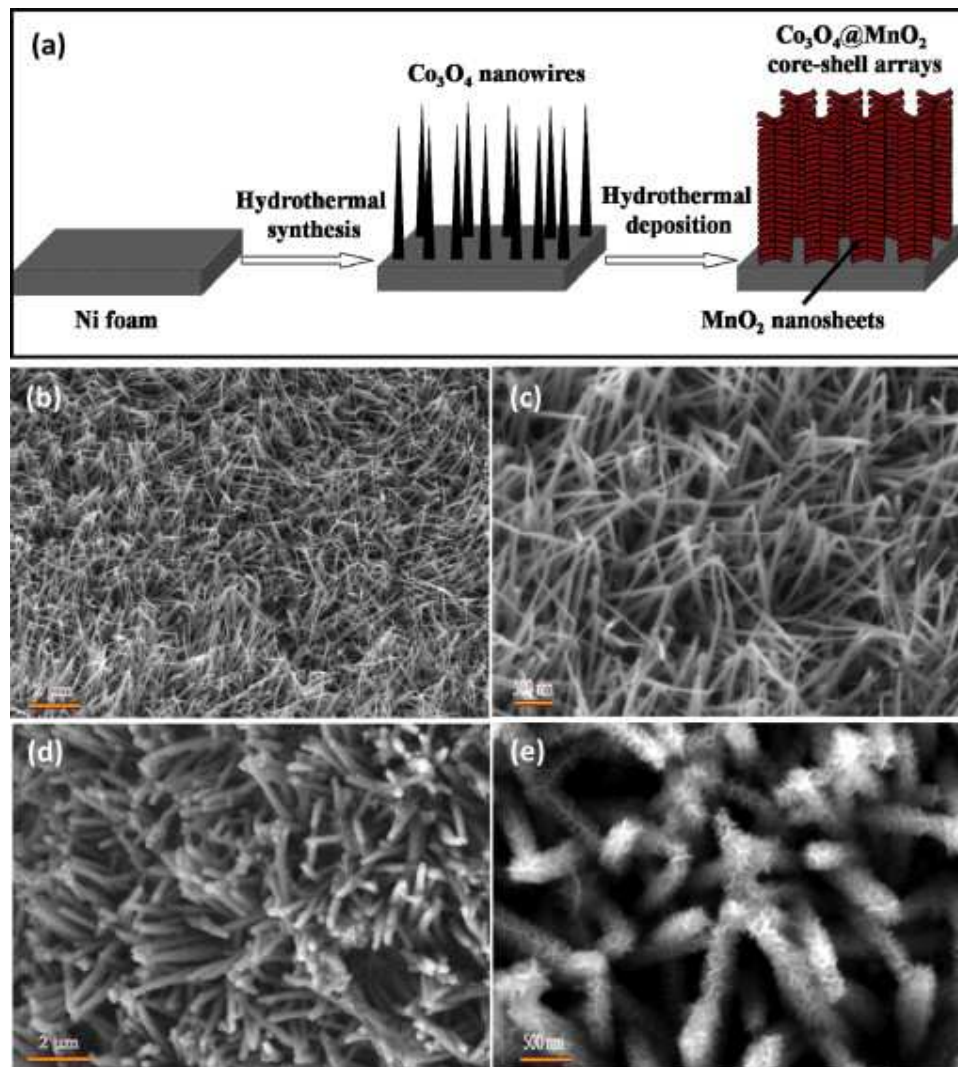
Fig. 22. (a) Possible formation mechanism for Ni(OH)$_2$-MnO$_2$ composite nanosheets on Ni foam and the structural schematic diagram of a single hybrid nanosheet. (b, c) Typical SEM images of the Ni(OH)$_2$-MnO$_2$ hybrid film supported on Ni foam. (e, f) Typical TEM images of the composite nanosheets. Reproduced with permission from ref. 345. Copyright 2013, WILEY-VCH Verlag GmbH & Co. KGaA, Weinheim.
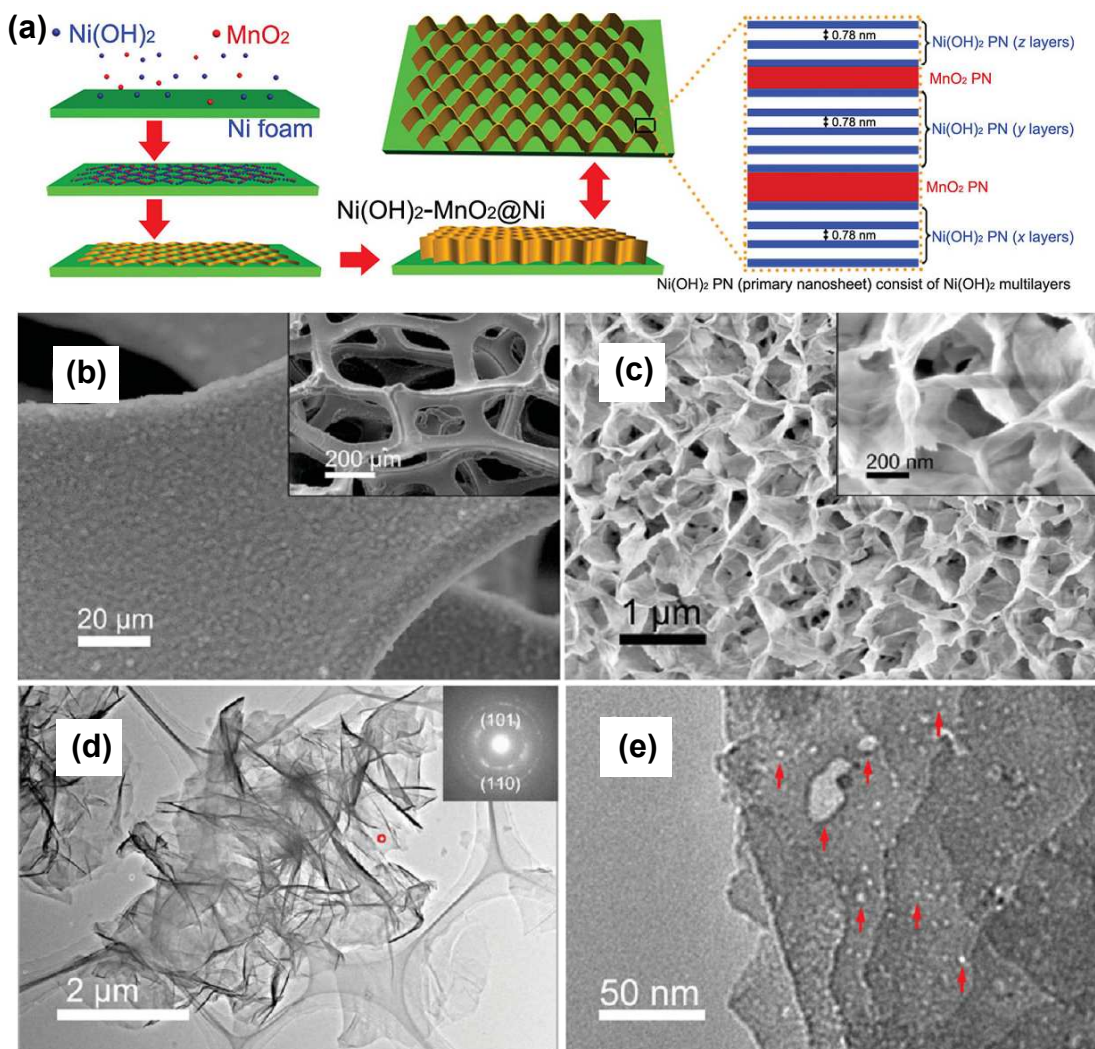
Fig. 23. (a) Schematic diagram illustrating the growth processes for H-TiO$_2$@MnO$_2$ composite nanowires on a carbon cloth substrate. (b, c) SEM and TEM images of H-TiO$_2$@MnO$_2$ composite NWs. Insets are magnified SEM image, TEM image and SAED pattern, respectively. (d) CV curves for the ASC device under flat, bent, and twisted conditions. Insets are the device pictures under test conditions. (e) Ragone plots of the ASC devices measured in the aqueous and gel electrolyte. Inset shows a red LED powered by a solid-state ASC device. Reproduced with permission from ref. 352. Copyright 2013, WILEY-VCH Verlag GmbH & Co. KGaA, Weinheim.
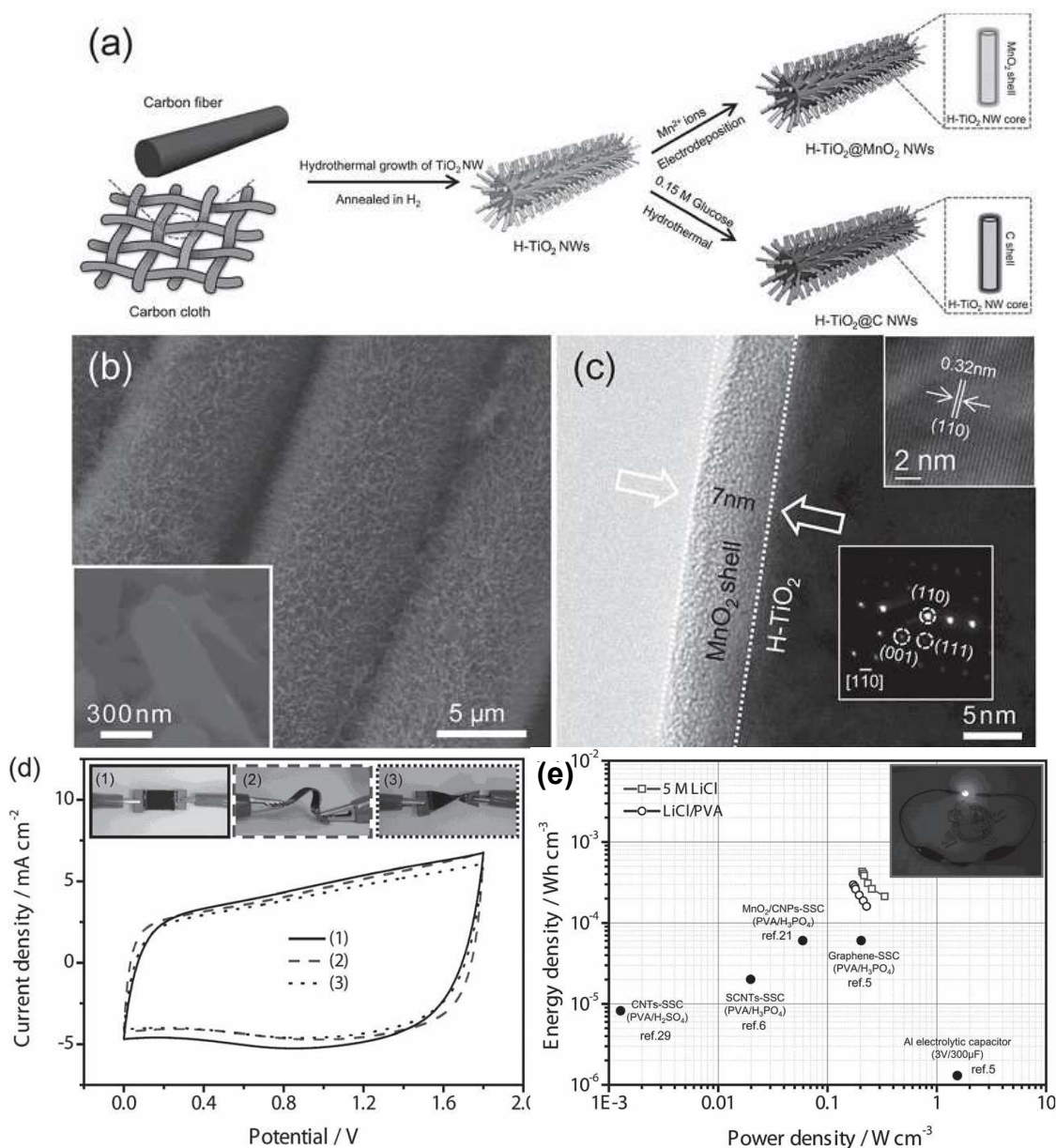
Fig. 24. (a, b) SEM images of the ZnO/MnO$_2$ composite nanowires on the carbon fiber substrates. (c) The TEM image of a single ZnO/MnO$_2$ core–shell NW. (d) The EDS pattern of ZnO/MnO$_2$ NWs. (e) The HRTEM image of a ZnO/MnO$_2$ core–shell NW. Reproduced with permission from ref. 359. Copyright 2014, Elsevier B.V.
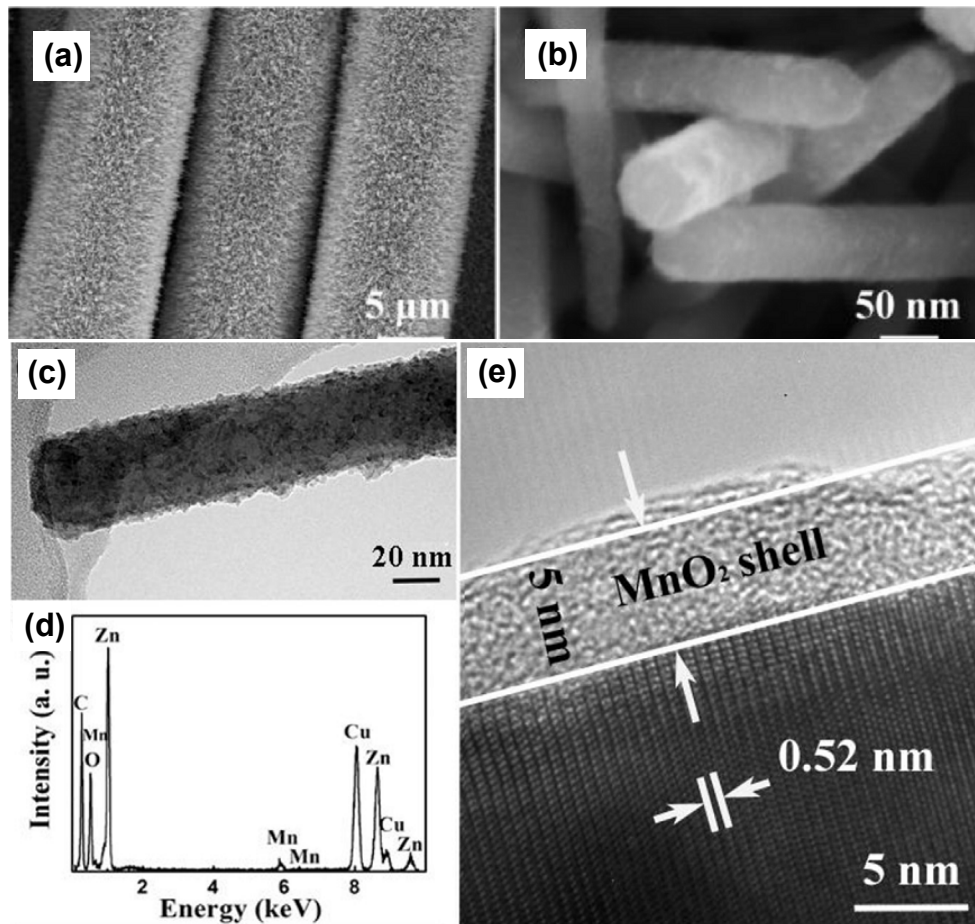
Fig. 25. (a) Schematic illustration of the growth mechanism of the CuO@MnO$_2$ core-shell nanostructures. (b-d) TEM images of the hierarchical CuO nanotube@MnO2 nanosheets nanostructures. The inset shows the corresponding SAED pattern taken from the edge of nanosheet. (e) STEM image and EDS mapping of the hierarchical CuO nanotube@MnO$_2$ nanosheets nanostructures. (f) Ragone plots of the asymmetric supercapacitor. The inset shows the digital image of a red-light-emitting diode (LED) lighted by the CuO@MnO$_2$//MEGO device. Reproduced with permission from ref. 362. Copyright 2014, Nature Publishing Group.
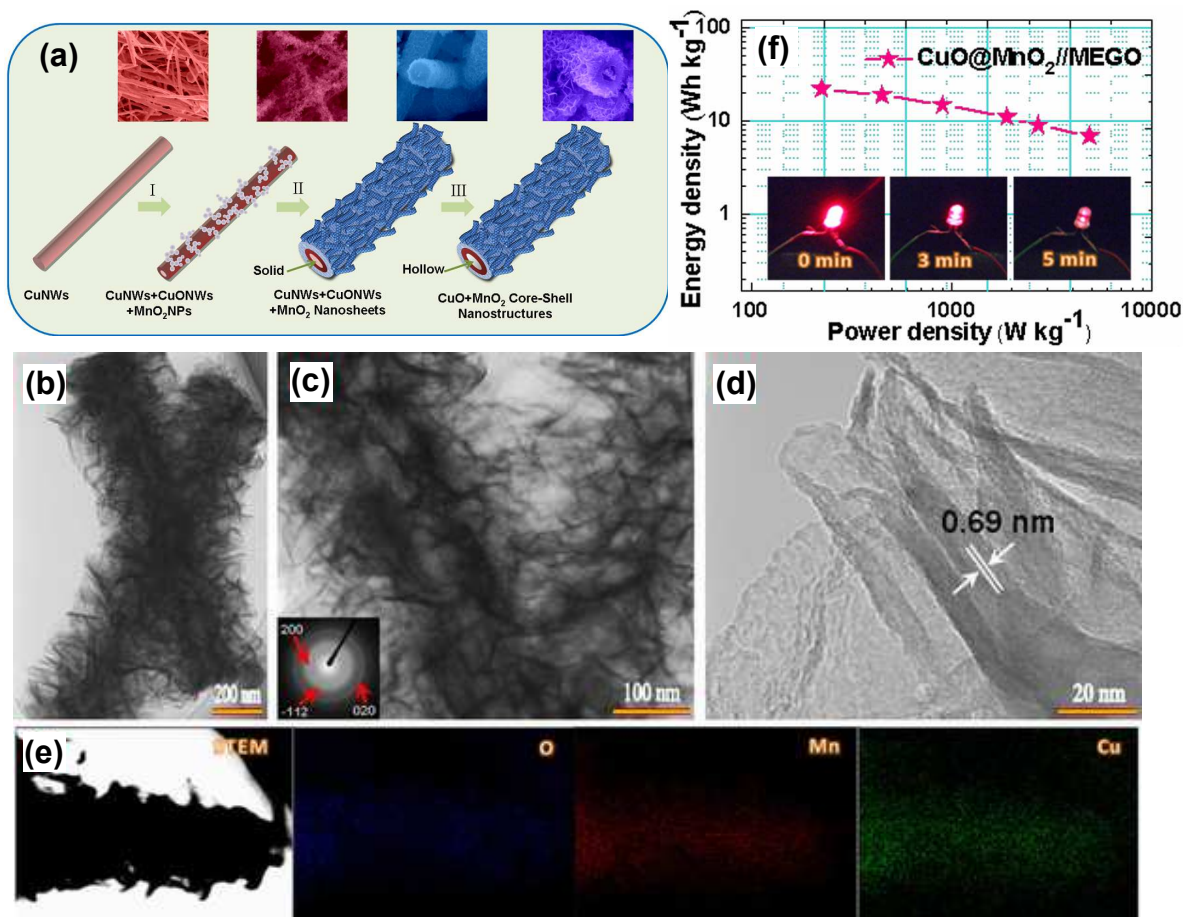
Fig. 26. (a, b) SEM images of Co_3O_4/SnO_2 nanoboxes. (c, d) SEM images of the $Co_3O_4/SnO_2@MnO_2$ core–shell nanostructures. (e-g) TEM images of the nanocomposite. The inset in (f) shows the corresponding SAED pattern taken from the edge of MnO_2 nanosheets. Reproduced with permission from ref. 367. Copyright 2015, The Royal Society and Chemistry.
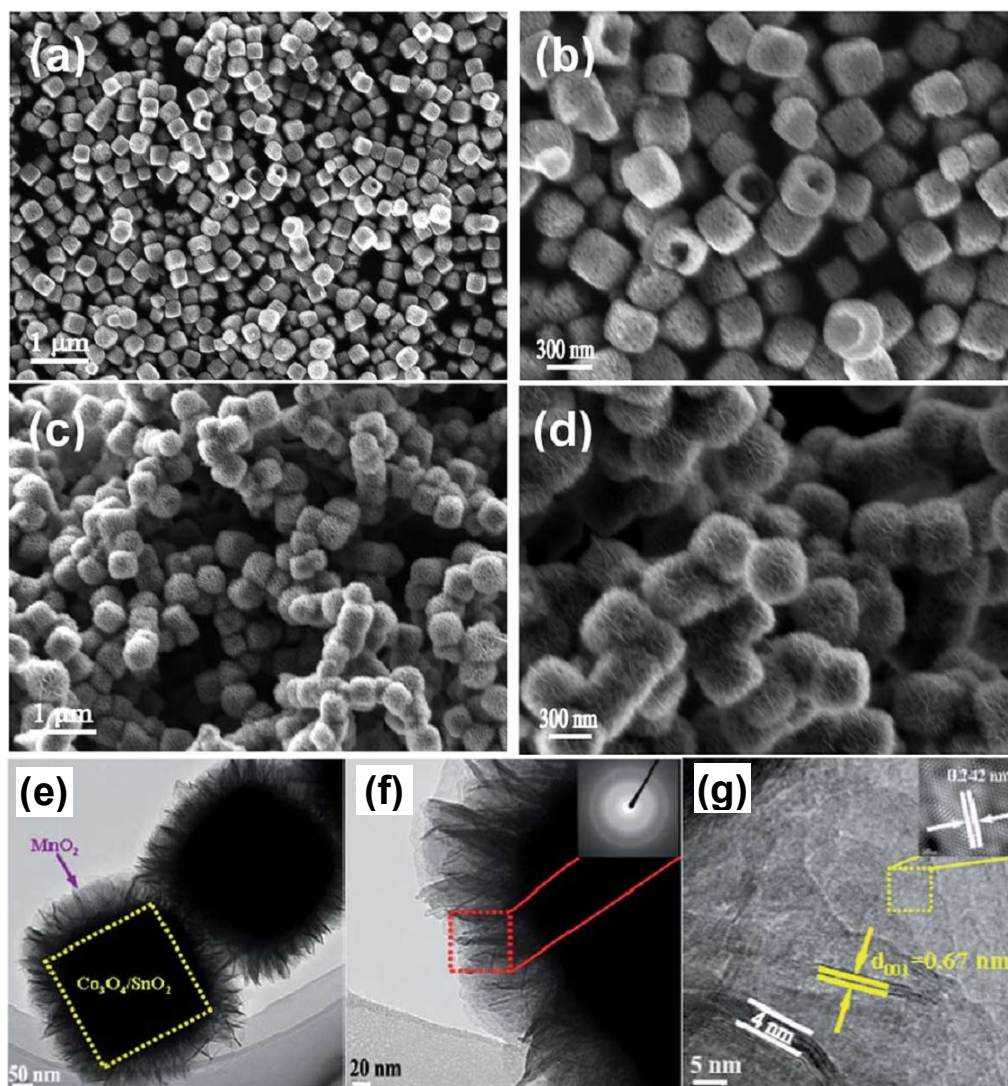
Fig. 27. (a, b) SEM images of NiCo$_2$O$_4$ nanowire arrays and hierarchical NiCo$_2$O$_4$@MnO$_2$ core–shell nanowire arrays. Reproduced with permission from ref. 369. Copyright 2014, The Royal Society and Chemistry. (c, d) SEM images of networked NiCo$_2$O$_4$/MnO$_2$-precursor and NiCo$_2$O$_4$/MnO$_2$ branched nanowire heterostructure arrays on Ni foam. Reproduced with permission from ref. 372. Copyright 2015, The Royal Society and Chemistry. (e, f) SEM images of NiCo$_2$O$_4$ nanosheet arrays and NiCo$_2$O$_4$@MnO$_2$ core–shell nanosheet arrays. Reproduced with permission from ref. 373. Copyright 2015, Elsevier B.V.

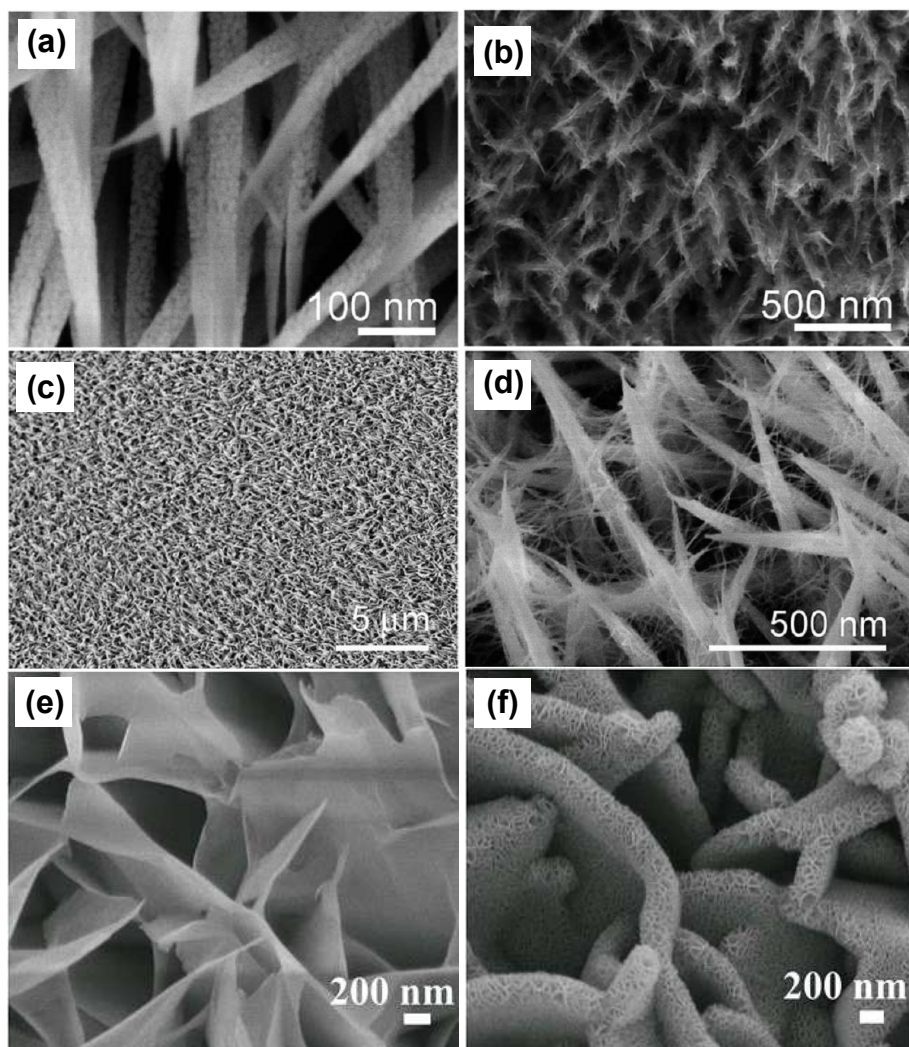Fig. 28 (a-d) SEM and TEM images of $ZnCo_2O_4/MnO_2$ nanocone forests. (e) Cyclic performance of the $ZnCo_2O_4/MnO_2$ electrodes at a current density of 2 A g^{-1}. (f) Rate performance of the electrodes at progressively increased current densities. Reproduced with permission from ref. 376. Copyright 2015, Elsevier B.V.
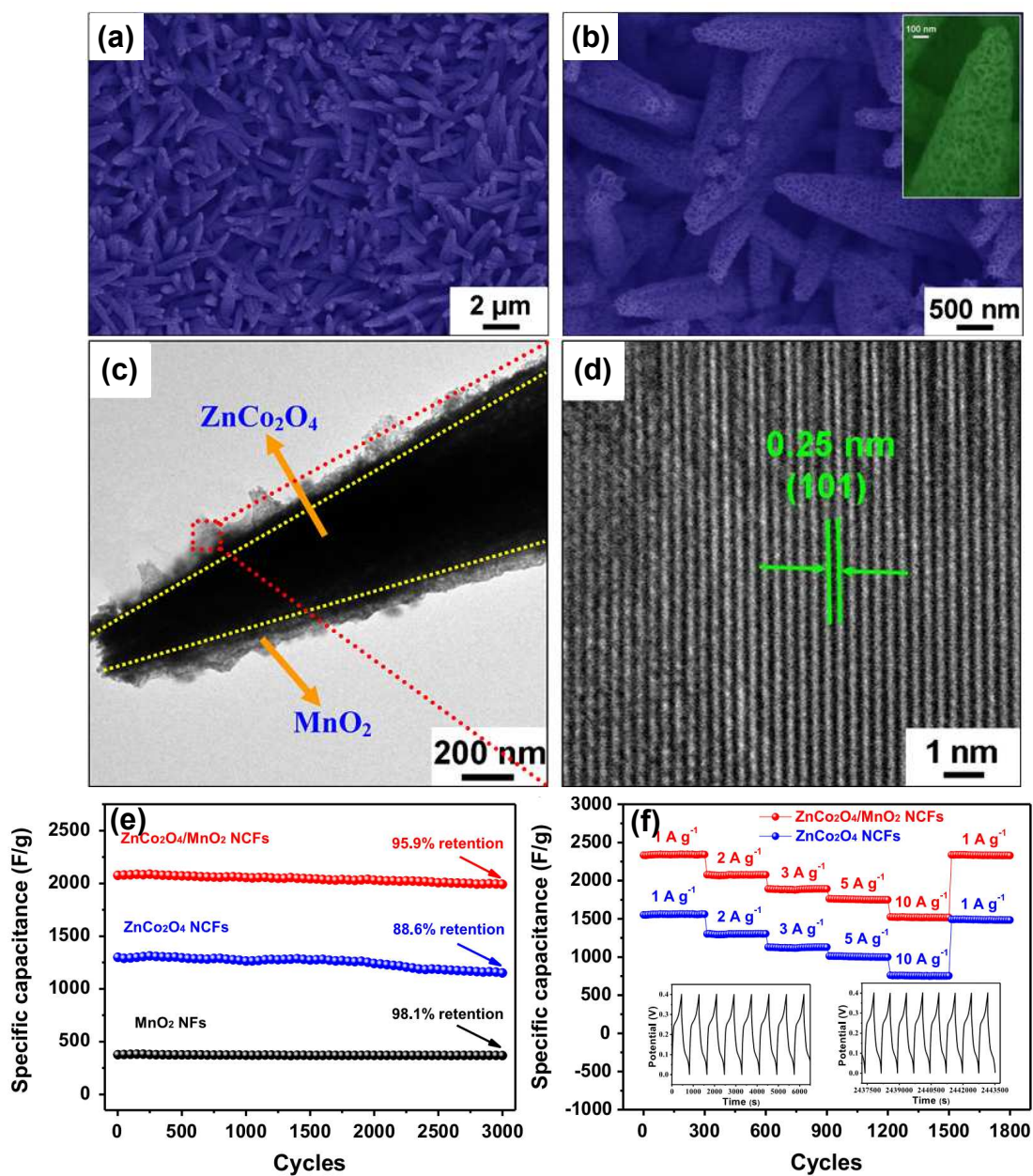
Fig. 29. (a) Illustration of the fabrication process for an asymmetric microsupercapacitor based on LSG–MnO$_2$ as the positive electrode and LSG as the negative electrode. (b) Photograph showing the asymmetric micro-supercapacitor. (c) Optical microscope image showing the LSG–GO–LSG-MnO$_2$ interface. (d) SEM image of the interface between GO and LSG shows the selective electrodeposition of MnO$_2$ on LSG only. (Inset) Magnified view of the GO and LSG area. (e) Integration of a supercapacitor array with solar cells for efficient solar energy harvesting and storage. Reproduced with permission from ref. 393. Copyright 2015, National Academy of Sciences, USA.
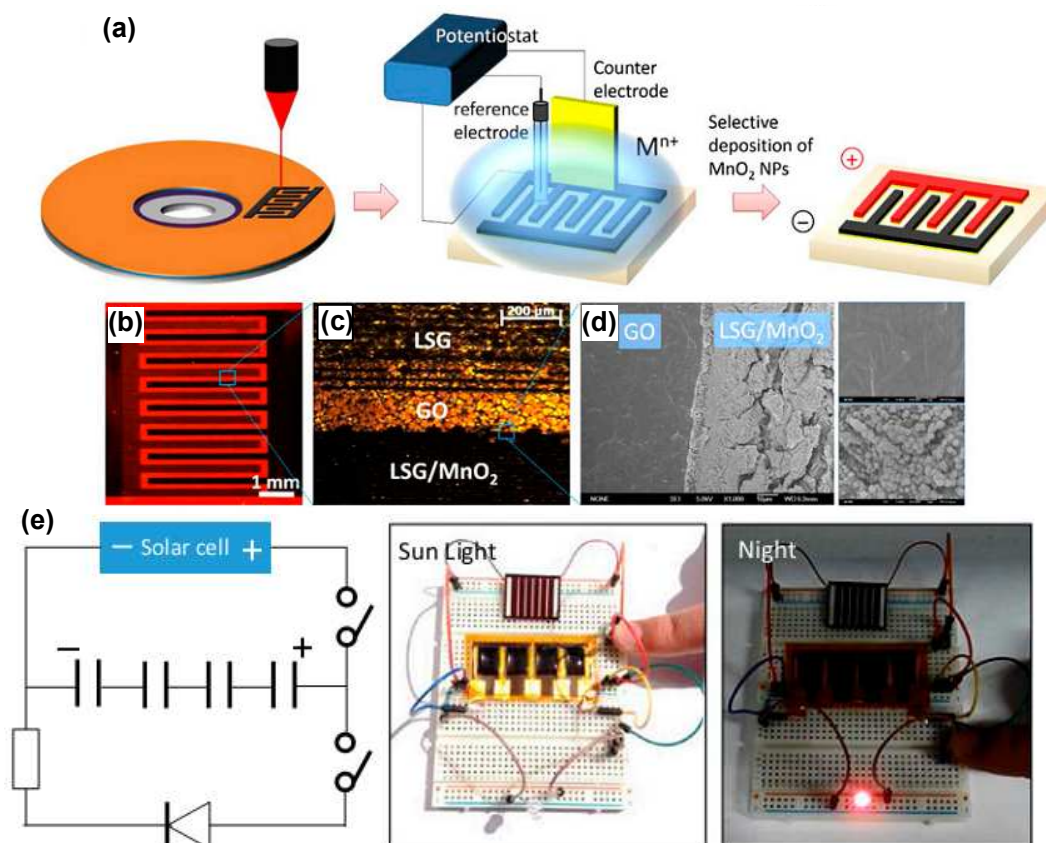
Fig. 30. (a) Fabrication of the GMA ternary hybrid film through vacuum filtration of the mixture of GO, MnO2, and AgNW suspension. (b) Digital photograph of the as-obtained GMA film supported on the cellulose acetate membrane after the vacuum filtration. (c) Schematic illustration of the fabrication procedures for RGMA-MSCs on an alumina substrate. (d-f) SEM images of RGMA ternary hybrid film on silicon wafer. (g, h) Digital photography of RGMA-MSCs microsupercapacitor electrode. Reproduced with permission from ref. 394. Copyright 2015, American Chemical Society.